Title
NanoMaterials for Energy Conversion and Storage : Concentrating Solar Power and Lithium-Ion Battery

Author
Kim, Tae Kyoung

Publication Date
2015

UNIVERSITY OF CALIFORNIA, SAN DIEGO

NanoMaterials for Energy Conversion and Storage: Concentrating Solar Power and Lithium-Ion Battery

A dissertation submitted in partial satisfaction of the
requirements for the degree Doctor of Philosophy

in

Materials Science and Engineering

by

Tae Kyoung Kim

Committee in Charge:

Professor Sungho Jin, Chair
Professor Renkun Chen, Co-Chair
Professor Prabhakar Bandaru
Professor Ratneshwar Lal
Professor Zhaowei Liu
Professor Yu Qiao

2015

The dissertation of Tae Kyoung Kim is approved, and it is acceptable in quality and form for publication on microfilm and electronically:

Co-Chair

Chair

University of California, San Diego

2015

DEDICATION

Dedicated to my loving wife, Shinyoung, rich scholar son, Euhan, gentle hero son, Minjune, and great parents, Pansul Kim, and Jeombun Lee who have shown continuous love and concern.

EPIGRAPH

Genius is one percent inspiration, ninety-nine percent perspiration.

Thomas Edison

TABLE OF CONTENTS

LIST OF FIGURES

LIST OF TABLES

ACKNOWLEDGEMENTS

I wish to acknowledge and deeply thank my advisor, Professor Sungho Jin and co-advisor, Professor Renkun Chen for their strong encouragement, support, and guidance during my Ph.D. work. I also wish to express my gratefulness to my committee members for their time and helpful suggestions: Professor Prabhakar Bandaru, Professor Ratneshwar Lal, Professor Yu Qiao, and Professor Zhaowei Liu.

I appreciate all the help from my collaborators in Department of Energy's SunShot project and ARPA-E project: Bryan VanSaders, Professor Jaeyun Moon, Elizabeth Caldwell, Sunmi Shin, Professor Renkun Chen, Professor Zhaowei Liu, Cyrus Rustomji, Duyoung Choi, Hyung-Man Cho, Dr. Jungmin You, Professor Shirley Meng, and Professor Joseph Wang. We have shared the joy and frustration together solving countless materials, fabrications and device problems in the past several years.

I would also like to recognize and thank the following individuals for their assistance in various aspects of this work: Dr. Chulmin Choi, Kelvin Gardner, Dongwon Chun, Chin-Hung Liu, Taewoo Kim, Cihan Kuru, Alireza Kargar, Dr. Kyungjun Hwang, Youngjin Kim, Jirapon Khamwannah, Ying Zhong, Gunwoo Kim, Serdar Yavuz, Erick Martinez-Loran, Jihye Baek, Dr. Young Oh, Dr. Gang Wang, Dr. Ekaterina Kritsuk, Prof. Olivia Graeve, Prof. Jun Hyun Han.

I wish to thank Nano3 staffs at UC San Diego. They have been always ready to help with the nanofabrication and characterization processes.

I would truly like to thank my wonderful friends who are like family and made this incredible journey possible. We enjoyed Americano coffee and sports every week, while sometimes discussing serious matters of life and research: Dr. Sungsik Hur, Professor Jinwoo Lee, Jae-Young Jung, Shiteng Zhao, Chomgun Cho.

Special thanks go to Charlotte Lauve, Patrick Mallon, Linda McKamey, Gina Torgersen, J.V. Agnew for taking care of the administrative matters and purchasing materials/chemicals for my research activities.

Lastly, I wish to express my deepest gratitude to my wife, my lucky twins, Euhan, Minjune, great Parents and other family members. Thanks again to my wife, Shinyoung, for her devoted support for our sons as well as for my march toward the PhD degree.

I also wish to thank my many friends and other colleagues who are too numerous to mention all by names.

Chapter 2, in full, is composed of two reprints and a prepared manuscript for submission and deals with three research topics. The first is a reprint of the material as it appears in Nano Energy 9 (2014) 32-40, “Si boride-coated Si nanoparticles with improved thermal oxidation resistance”, Tae Kyoung Kim, Jaeyun Moon, Bryan VanSaders, Dongwon Chun, Calvin Gardner, Jae-Young Jung, Gang Wang, Renkun Chen, Zhaowei Liu, Yu Qiao, and Sungho Jin. The second is a reprint of the material as it appears in Nano Energy 11 (2015) 247-259, “Tandem structured spectrally selective coating layer of copper oxide nanowires combined with cobalt oxide nanoparticles”, Tae Kyoung Kim, Bryan VanSaders, Jaeyun Moon, Taewoo Kim, Chin-Hung Liu, Jirapon Khamwannah, Dongwon Chun, Duyoung Choi, Alireza Kargar, Renkun Chen, Zhaowei Liu, and Sungho Jin. The third is currently being prepared for submission to a SCI journal, “Two-layered tandem structures with copper-contained spinel metal oxide nanoparticles”, Tae Kyoung Kim, Bryan VanSaders, Elizabeth Caldwell, Sunmi Shin, Youngjin Kim, Zhaowei Liu, Renkun Chen, and Sungho Jin. The dissertation author was the primary investigator and author of these aforementioned three papers.

Chapter 3, in full, is currently being prepared for submission to a SCI journal. “Carbon nanotube-embedded lithium cobalt phosphate nanocomposites for high voltage cathode of lithium ion batteries”, Tae Kyoung Kim, Cyrus S. Rustomji, Hyung-Man Cho, Duyoung Choi, Dongwon Chun, Elizabeth Caldwell, Jun Hyun Han, Renkun Chen, and Sungho Jin. The dissertation author was the primary investigator and author of this paper.

VITA

1998	Bachelor of Science in Metallurgical Engineering, Yonsei University, Seoul, South Korea
2000	Master of Science in Metallurgical Engineering, Yonsei University, Seoul, South Korea
2011	Senior Research Engineer in Electronic Materials R&D Center, Samsung Cheil Industries, South Korea
2015	Doctor of Philosophy in Materials Science and Engineering, University of California, San Diego

LIST OF PUBLICATIONS

<u>Journals Articles:</u>

[1] Carbon nanotube-embedded lithium cobalt phosphate nanocomposites for high voltage cathode of lithium ion batteries, **Tae Kyoung Kim**, Cyrus S. Rustomji, Hyung-Man Cho, Duyoung Choi, Dongwon Chun, Elizabeth Caldwell, Jun Hyun Han, Renkun Chen, and Sungho Jin, (Manuscript in Preparation).

[2] Two-layered tandem structures with copper-contained spinel metal oxide nanoparticles, **Tae Kyoung Kim**, Bryan VanSaders, Elizabeth Caldwell, Sunmi Shin, Youngjin Kim, Zhaowei Liu, Renkun Chen, and Sungho Jin, (Manuscript in Preparation).

[3] Thin-film electrochemical sensor electrode for electrolytic conductivity, cyclic voltammetry and temperature measurements, Cyrus S. Rustomji, Jimmy Mac, Chulmin Choi, **Tae Kyoung Kim**, Duyoung Choi, and Sungho Jin, J. Appl. Electrochemistry (Manuscript No.: JACH-D-15-00059).

[4] Tandem structured spectrally selective coating layer of copper oxide nanowires combined with cobalt oxide nanoparticles, **Tae Kyoung Kim**, Bryan VanSaders, Jaeyun Moon, Taewoo Kim, Chin-Hung Liu, Jirapon Khamwannah, Dongwon Chun, Duyoung Choi, Alireza Kargar, Renkun Chen, Zhaowei Liu, and Sungho Jin, Nano Energy, **11** (2015) 247-259.

[5] Solution-processed $CoFe_2O_4$ nanoparticles on carbon fiber papers for efficient and durable oxygen evolution reaction, Alireza Kargar, Serdar Yavuz, **Tae Kyoung Kim**, Chin-Hung Liu, Cihan Kuru, Cyrus Rustomji, Sungho Jin, and Prabhakar R. Bandaru, Nano Energy (Manuscript No. NANOEN-D-15-00398).

[6] Black oxide nanoparticles as durable solar absorbing material for high-temperature concentrating solar power system, Jaeyun Moon*, **Tae Kyoung Kim***, Bryan VanSader*, Chulmin Choi, Zhaowei Liu, Sungho Jin, and Renkun Chen, (*: equal contributor), Solar Energy Materials and Solar Cells, **134** (2015) 417-424.

[7] NiOx-Fe_2O_3-coated p-Si photocathodes for enhanced solar water splitting in neutral pH water, Alireza Kargar, Justin S. Cheung, Chin-Hung Liu, **Tae Kyoung Kim**, Conor T. Riley, Shaohua Shen, Zhaowei Liu, Donald J. Sirbuly, Deli Wang, and Sungho Jin, Nanoscale, **7** (2015) 4900-4905.

[8] Low temperature sintering Cu_6Sn_5 nanoparticles for superplastic and super-uniform high temperature circuit interconnections, Ying Zhong, Rong An, Chunqing Wang, ZhiQuan Liu , ChinHung Liu, CaiFu Li, **Tae Kyoung Kim**, and Sungho Jin, Accepted to Small in 2015.

[9] Si-Si boride nanoparticles with high thermal oxidation resistance for solar thermal applications, **Tae Kyoung Kim**, Jaeyun Moon, Bryan VanSaders, Dongwon Chun, Calvin J. Gardner, Jae-Young Jung, Gang Wang, Renkun Chen, Zhaowei Liu, Yu Qiao, and Sungho Jin, Nano Energy, **9** (2014) 32-40.

[10] Controlled metallic nanopillars for low impedance biomedical electrode, Calvin J Gardner, Jonathan Trisnadi, **Tae Kyoung Kim**, Karla Brammer, Lina Reiss, Li-han Chen, and Sungho Jin, Acta Biomaterialia, **10** (2014) 2296-2303.

[11] High performance multi-scaled nanostructured spectrally selective coating for concentrating solar power, Jaeyun Moon, Dylan Lu, Bryan VanSaders, **Tae Kyoung Kim**, Seong Deok Kong, Sungho Jin, Renkun Chen, and Zhaowei Liu, Nano Energy, **8** (2014) 238-246.

[12] Control of nanogeometry for advanced energy applications, Jirapon Khamwannah, Hyunsu Kim, YanYan Zhang, **Tae Kyoung Kim**, and Sungho Jin, J. Nanosci. and Nanotechnol., **13** (2013) 8199.

[13] Uniformly nano-patterned grapheme field effect transistors with enhanced properties, Duyoung Choi, Cihan Kuru, Gunwoo Kim, **Taekyoung Kim**, Renkun Chen, and Sungho Jin, Nanoscale Research Letters (Manuscript No.: 2507103451656385).

Patents:

[1] Electrochemical devices comprising compressed gas solvent electrolytes, Cyrus Rustomji, Sungho Jin, **Taekyoung Kim**, Duyoung Choi, Jungmin You, Joseph Wang, (USA) International Application No. PCT/US14/66015.

[2] Semiconductor processing by magnetic field guided etching, Sungho Jin, Young Oh, Chulmin Choi, Dae-Hoon Hong, **Tae Kyoung Kim**, (USA) Publication No. US2014/0256078A1, International Application No. PCT/US2012/060143.

[3] Solar energy absorbing coating and methods of fabrication, Sungho Jin, Renkun Chen, Zhaowei Liu, Jaeyun Moon, **Tae Kyoung Kim**, and Bryan Van Saders, (USA)Internation Application No. PCT/US15/20589.

[4] Sunlight reflecting materials and methods of fabrication, Sungho Jin, Chulmin Choi, Jaeyun Moon, **Tae Kyoung Kim**, and Ratneshwar Lal, (USA) Provisional Application Serial No. 61/832,118.

News Release:

[1] New solar power material converts 90 percent of captured light into heat, UC San Diego Jacobs School of Engineering News, http://www.jacobsschool.ucsd.edu/news/news_releases/release.sfe?id=1589.

ABSTRACT OF THE DISSERTATION

NanoMaterials for Energy Conversion and Storage: Concentrating Solar Power and Lithium-Ion Battery

by

Tae Kyoung Kim

Doctor of Philosophy in Materials Science and Engineering

University of California, San Diego, 2015

Professor Sungho Jin, Chair
Professor Renkun Chen, Co-Chair

Renewable power plants and battery energy storage systems are expanding worldwide in many countries for eventual smart grid systems. However, the high cost of electricity generation and storage is still a barrier to the utilization of abundant renewable energy such as sunlight and wind. For instance, the levelized cost of electricity (LCOE) of concentrating solar power (CSP) plants entering service in 2019 is projected to be 24.3 ¢/kWh, compared to nuclear power plants' LCOE of 9.6 ¢/kWh (US EIA).

For the CSP system to obtain the competitiveness, new technologies have to be developed to reduce electricity price. If new solar receivers can be operated stably at 750 ^{o}C in air, Carnot efficiency can increase by 1.5 times from the conventional CSP opertated at 500 ^{o}C. To develop solar receivers operated at 750 ^{o}C under air, 3 types of approach are carried out including 'Si boride-coated Si core-shell nanoparticles', 'tandem-structured spectrally selective coating (SSC) layers with CuO nanowires and Co_3O_4 nanoparticles' and 'tandem-structured SSC layers with $CuFeMnO_4$ and $CuCr_2O_4$ nanoparticles'. Finally 2-layered SSC with porous $CuFeMnO_4$ top and dense $CuCr_2O_4$ bottom layer can achieve 0.90 in figure of merit (efficiency of solar-to-thermal energy), assuming an operation at 750 ^{o}C and 1000 in sunlight concentrating factor.

Lithium-ion batteries (LIB) with high energy density can be used for energy storage system for many applications including renewable power plants and electric vehicles capable of longer distance driving. One method to make LIB with high energy density is to use high voltage cathodes such as $LiCoPO_4$ (LCP, 4.6-4.8V, 800 Wh/kg). However, LCP material has one drawback of low electrical conductivity (~10^{-15} S/cm) which needs to be solved for LIB applications. In this research, multi-wall carbon nanotubes-embedded LCP nanocomposites (LCP-CNT) are devised in order to enhance the electrical conductance of LCP-CNT particles which can improve cell capacity by 2 times from 24.4 mAh/g for bare LCP to 52.5 mAh/g. And main important factors affecting the capacity increment are a reduced impedance of charge transfer (intercalation/de-intercalation of Li^+) in addition to uniform distribution of MWCNTs which can be fabricated during gelation step of $LiCoPO_4$ in synthesis procedure.

CHAPTER 1: Introduction

1.1 Motivation and Background

Electricity generation is accomplished by many different approaches including conventional coal power plant, natural gas-fired power plant, nuclear power plant, geothermal power plant, biomass power plant, wind power plant, solar PV (photovoltaic) cell power plant, solar thermal (concentrating solar power) plant, and hydroelectric plant. Fig. 1-1(a) shows that the ratio of electricity generated by renewable sources is ~ 13% among all electricity generations in year 2012 and is anticipated to grow up to 18% in 2040 according to the projection of US Energy Information Administration (EIA) [1]. The amount of electricity generated by solar, wind, and other renewable sources became comparable to that by hydropower in 2012 and is expectred to substantially surpass it in 2040, as shown in Fig. 1-1(b) [1].

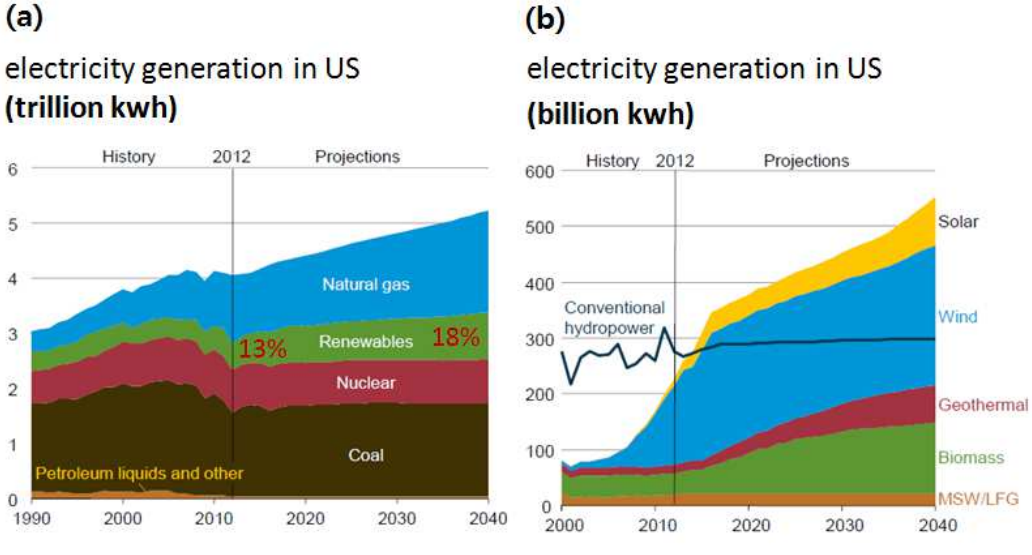

Figure 1-1. History and projection of (a) overall electricity generations in US including the generation with renewable sources, and (b) the renewable electricity generations [1].

When considering levelized cost of electricity (LCOE) for year 2019, solar thermal electricity generation such as concentrating solar power (CSP) system has higher LCOE value (~22.4¢/kWh) than nuclear power plant (8.6¢/kWh) and renewable wind power plant (8¢/kWh), as summarized in Table 1-1 [1]. Although the solar energy coming from the sun is abundant enough to be stable for the next 4 billion years [2], the electricity generation power plants using the sunlight cannot grow if the economical barrier of high cost remains the same, as compared to other power plants. It is therefore necessary to develop technologies to reduce the cost of electricity generation in CSP system in order to expand the utilization of this type of solar power plant.

Table 1-1. US average LCOE (Y2012 $/MWh) for plants entering service in 2019 [1]

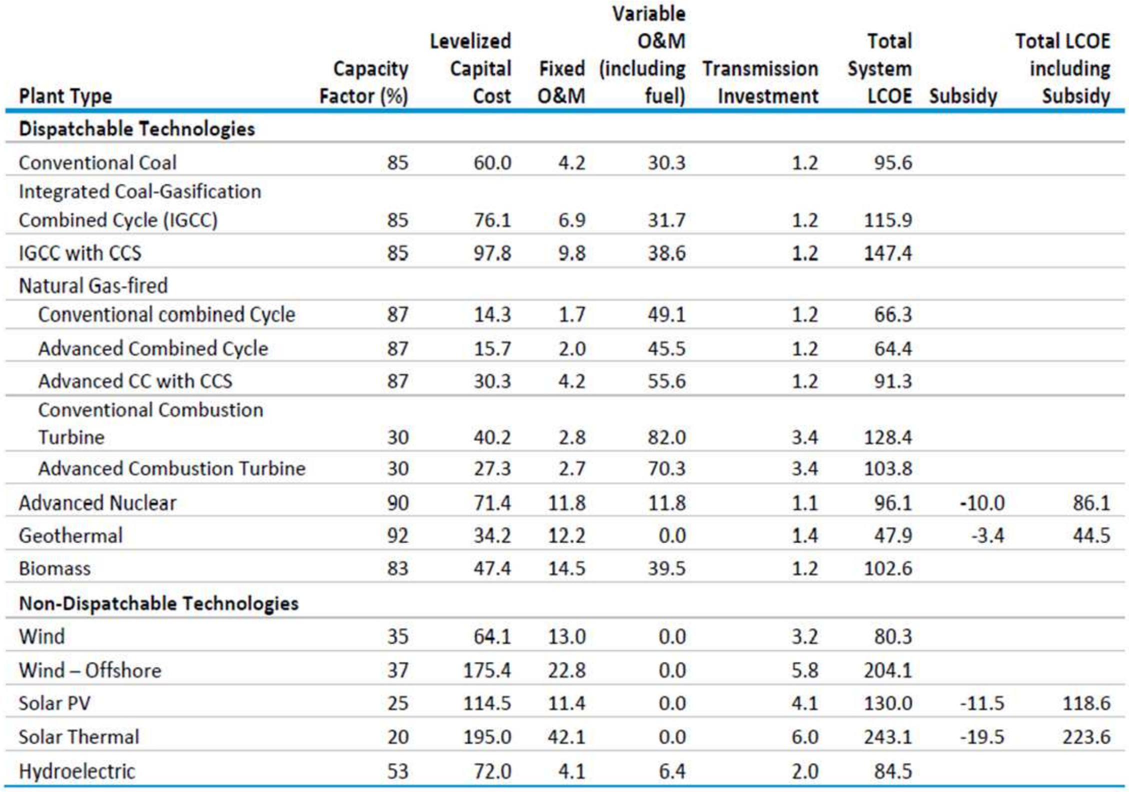

Plant Type	Capacity Factor (%)	Levelized Capital Cost	Fixed O&M	Variable O&M (including fuel)	Transmission Investment	Total System LCOE	Subsidy	Total LCOE including Subsidy
Dispatchable Technologies								
Conventional Coal	85	60.0	4.2	30.3	1.2	95.6		
Integrated Coal-Gasification Combined Cycle (IGCC)	85	76.1	6.9	31.7	1.2	115.9		
IGCC with CCS	85	97.8	9.8	38.6	1.2	147.4		
Natural Gas-fired								
Conventional combined Cycle	87	14.3	1.7	49.1	1.2	66.3		
Advanced Combined Cycle	87	15.7	2.0	45.5	1.2	64.4		
Advanced CC with CCS	87	30.3	4.2	55.6	1.2	91.3		
Conventional Combustion Turbine	30	40.2	2.8	82.0	3.4	128.4		
Advanced Combustion Turbine	30	27.3	2.7	70.3	3.4	103.8		
Advanced Nuclear	90	71.4	11.8	11.8	1.1	96.1	-10.0	86.1
Geothermal	92	34.2	12.2	0.0	1.4	47.9	-3.4	44.5
Biomass	83	47.4	14.5	39.5	1.2	102.6		
Non-Dispatchable Technologies								
Wind	35	64.1	13.0	0.0	3.2	80.3		
Wind – Offshore	37	175.4	22.8	0.0	5.8	204.1		
Solar PV	25	114.5	11.4	0.0	4.1	130.0	-11.5	118.6
Solar Thermal	20	195.0	42.1	0.0	6.0	243.1	-19.5	223.6
Hydroelectric	53	72.0	4.1	6.4	2.0	84.5		

1.1.1 Concentrating solar power (CSP) system

Recently three concentrating solar power (CSP) plants have been constructed in Mojave desert located at Ivanpah of California and entered into service in 2014 [3], as shown in Fig. 1-2. This Ivanpah CSP plant can generate electricity of 392 MW and supply power for 94,400 average American homes [4].

Figure 1-2. A photo image of Ivanpah concentrating solar power plants located near Mojave desert in California [3].

Fig. 1-3 exhibits the concept of CSP plant generating electricity using sunlight reflected by many heliostats mirrors and concentrated onto solar receiver located on top of CSP tower [5]. The solar receiver is made of spectrally selective coating layer on the surface of metallic alloy tube inside which a heat transfer fluid (HTF) flows and is heated up to 500 ^{o}C by the absorbed solar energy. With such high temperature HTF, heat exchangers make high pressure steam which turns turbine generators to make electricity.

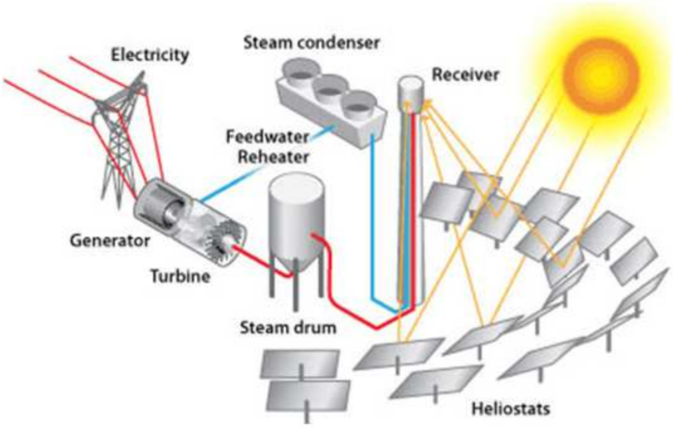

Figure 1-3. A concept of electricity generation in concentrating solar power plant [5].

US Department of Energy (DOE) planned to reduce the levelized cost of electricity (LCOE) in CSP plant from 21¢/kWh in 2010 to 6¢/kWh by 2020 [6], as shown in Fig. 1-4(a). To reach this target of cost reduction, some important requirements need to be satisfied by development of new technologies as displayed in Fig. 1-4(b). Especially in solar receiver part, the following conditions have to be achieved; HTF's exit temperature $\geq 650^{o}C$, solar to thermal efficiency $\geq 90\%$, and lifetime $\geq 10{,}000$ cycles [6]. The solar receiver temperature of conventional CSP plant is around $500^{o}C$ but it needs to be increased up to $750^{o}C$ for next generation CSP plant to make HTF exit temperature to be at least $650^{o}C$.

In this research, the coating materials and structures for low cost solar receivers with high efficiency and thermal stability have been developed by collaboration of UC San Diego's 3 teams through DOE's SunShot project. 3 types of solar receiver layer materials have been researched including Si-boride coated Si core-shell nanoparticles, tandem-structured SSC layers with CuO nanowires and Co_3O_4 nanoparticles, and 2-layered tandem structure with Cu-contained black oxide nanoparticles.

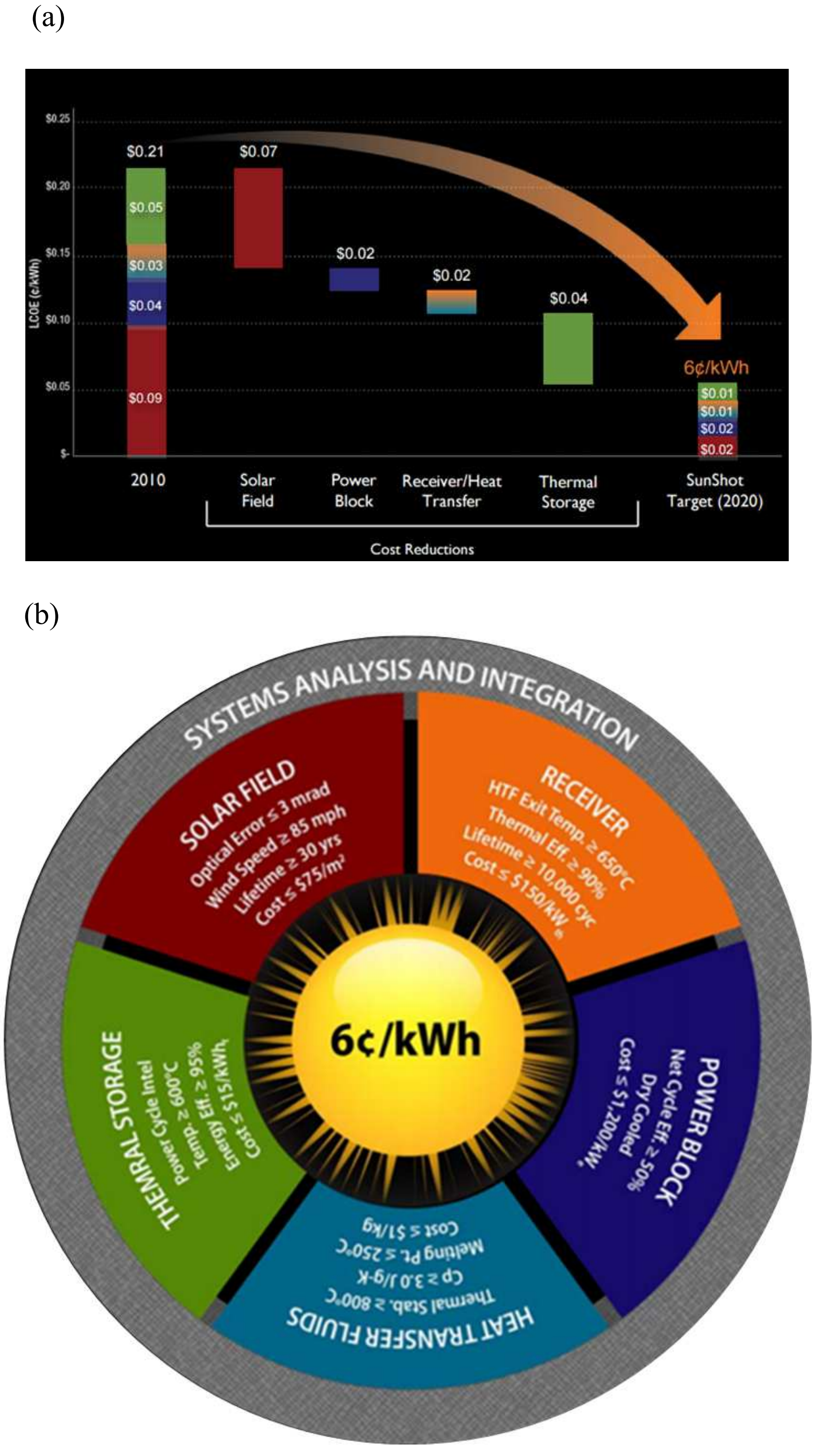

Figure 1-4. DOE’s strategies showing (a) the goal of electricity generation cost and (b) the requirements to achieve 6¢/kWh in 2020 [6].

1.1.2 Battery energy storage system (BESS) and smart grids

The generated electricity by renewable sources such as concentrating solar power, solar PV cell, and wind power, can flow directly to homes, commercial buildings, and other facilities. But the renewable electricity generation power plants can supply more stable electricity via battery energy storage systems (BESS) which stores electricity and distributes it again to various usages by smart grid system as shown in Fig. 1-5.

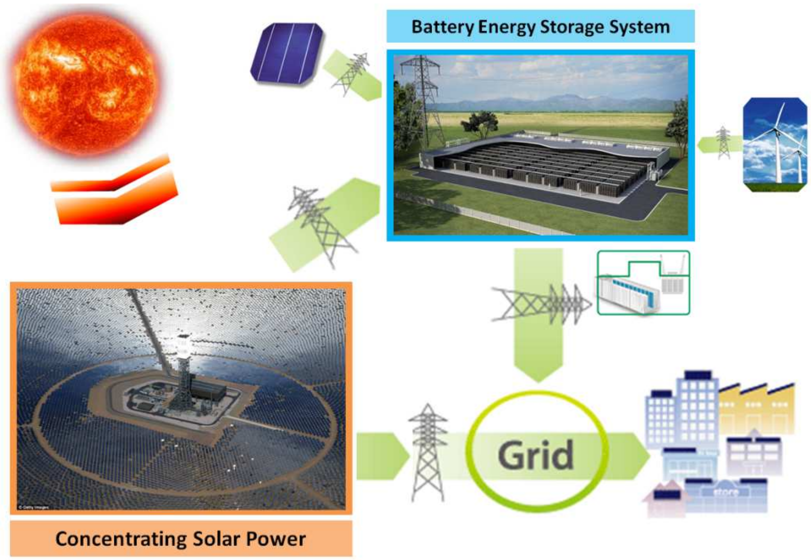

Figure 1-5. A smart grid system connecting renewable power plants (concentrating solar power plant, solar PV cell, and wind power) and battery energy storage system with residential homes, buildings, and factories.

Lithium-ion batteries have a higher energy density because of light weight as shown in Table 1-2 relatively to nickel-metal hydride (Ni-MH) rechargeable batteries and do not have a memory effect which is a critical drawback of Ni-MH batteries. Fig. 1-6 shows the operation mechanism of lithium-ion batteries where Li^+ ion is de-intercalated from a cathode during charging and is intercalated into the cathode during discharging of the lithium-ion battery [7]. Reversely, an anode such as graphite electrode is intercalated with Li$^+$ ion during charging and de-intercalated during discharging procedure of the battery.

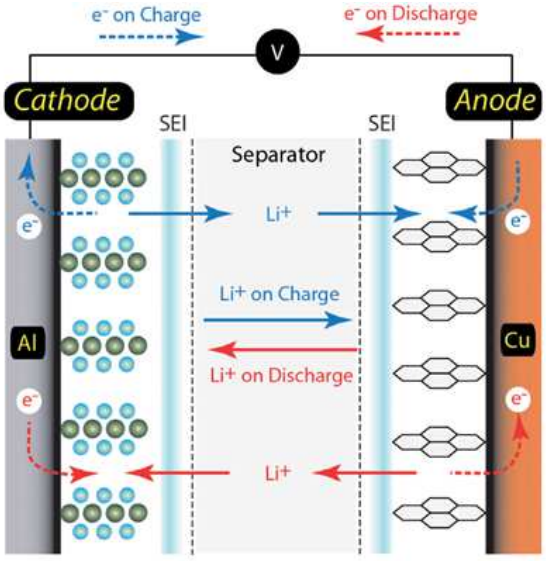

Figure 1-6. Reaction mechanism of charging and discharging in a lithium-ion battery [7].

There are a few types of high voltage cathode materials including $LiNi_{0.5}Mn_{1.5}O_4$, $LiCoPO_4$, and $LiNiPO_4$ as shown in Fig. 1-7 and Table 1-2. Among these materials $LiCoPO_4$ (LCP) has high discharging voltage (4.6-4.8V vs. Li) and large capacity (167 mAh/g) enough to increase energy density (800 mAh/g) by 1.5 times compared to a conventional lithium-ion battery with $LiCoO_2$ electrode (534 mAh/g) [7-9].

Lithium-ion batteries with $LiCoPO_4$ cathode of high energy density can cost down the battery energy storage system (BESS) to support the growth and stabilization of renewable power plants and also will enable electric vehicles to voyage to more distant place. In this research, carbon nanotube-embedded LCP electrode was developed because carbon nanotubes have higher electrical conductivity than bare LCP particles so that the embedding structure can help LCP electrode improve conductance.

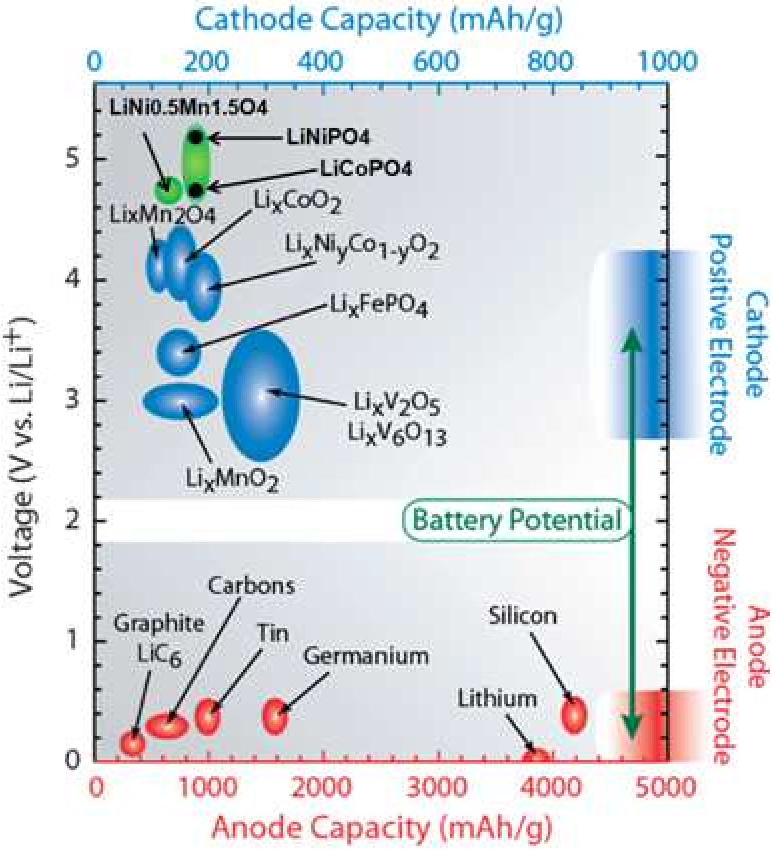

Figure 1-7. Diagram showing the operation voltage and capacity of anode and cathode materials [7]-[9].

Table 1-2. Capacity, discharging voltage, and energy density of cathode materials [7]-[9].

Cathodes	Capacity (mAh/g)	Discharging V vs. Li	Energy Density (Wh/kg)
LiNiPO4	167	5.0-5.1	850
LiCoPO4	**167**	**4.6-4.8**	**800**
LiNi0.5Mn1.5O4	147	4.6-4.7	690
LiCoO2 (Conventional)	137 (x=0.5)	3.9	534

1.2 Thesis Outline

The central focus of this thesis is to develop nanoparticles and new layer structures which is desirable for energy conversion systems including concentrating solar power plants and lithium-ion batteries.

In Chapter 2, three types of spectrally selective coating (SSC) layers have been mainly developed with lab-made Si-boride core-shell nanoparticles, CuO nanowires, Co_3O_4 nanoparticles, and Cu-contained spinel black oxide nanoparticles. In the long run, the tandem-structured SSC layer fabricated with a porous $CuFeMnO_4$ top layer and a dense $CuCr_2O_4$ layer shows highest conversion efficiency (90.3%) of solar to thermal energy, good thermal stability at 750^oC in air and strong adhesion property of coating layer.

In chapter 3, carbon nanotube-embedded $LiCoPO_4$ (LCP) nanocomposites have been developed for high voltage cathode of lithium-ion batteries which can be used for energy storage system storing electricity generated by renewable power plants such as the concentrating solar power plants. Multi-wall carbon nanotubes (MWCNTs) can be dispersed with LCP precursors with a dry mixing procedure and distributed more uniformly in the process of gelation of $LiCoPO_4$. Cathodes fabricated with this type of LCP-CNT nanocomposite particles finally have larger capacity compared to bare LCP cathode.

1.3 References

[1] US Energy Information Administration (EIA), Levelized cost and levelized avoided cost of new generation resources, Annual Energy Outlook , 2014.

[2] T.K. Kim, B. VanSaders, J. Moon, T. Kim, C.-H. Liu, J. Khamwannah, D. Chun, D. Choi, A. Kargar, R. Chen, Z. Liu, and S. Jin, Nano Energy **11**, 247 (2015).

[3] http://www.brightsourceenergy.com

[4] http://energy.gov/articles/celebrating-completion-worlds-largest-concentrating-solar-power-plant

[5] http://energy.gov/eere/energybasics/articles/concentrating-solar-power-tower-system-basics

[6] http://energy.gov/eere/sunshot/concentrating-solar-power

[7] B.J. Landi, M.J. Ganter, C.D. Cress, R.A. DiLeo, and R.P. Raffaelle, Energy Environ. Sci. **2**, 638 (2009).

[8] V. Aravindan, J. Gnanaraj, Y.-S. Lee, and S. Madhav, J. Mater. Chem. **A 1**, 3518 (2013).

[9] G. Hautier, A. Jain, S.P. Ong, B. Kang, C. Moore, R. Doe, and G. Ceder, Chem. Mater. **23**, 3495 (2011).

CHAPTER 2: NanoMaterials and Tandem Structures for Solar Receiver of Concentrating Solar Power System

This chapter is composed of two reprints and a prepared manuscript for submission and contains 3 research topics. The first is a reprint of the material as it appears in Nano Energy 9 (2014) 32-40, "Si boride-coated Si nanoparticles with improved thermal oxidation resistance", Tae Kyoung Kim, Jaeyun Moon, Bryan VanSaders, Dongwon Chun, Calvin Gardner, Jae-Young Jung, Gang Wang, Renkun Chen, Zhaowei Liu, Yu Qiao, and Sungho Jin. The second is a reprint of the material as it appears in Nano Energy 11 (2015) 247-259, "Tandem structured spectrally selective coating layer of copper oxide nanowires combined with cobalt oxide nanoparticles", Tae Kyoung Kim, Bryan VanSaders, Jaeyun Moon, Taewoo Kim, Chin-Hung Liu, Jirapon Khamwannah, Dongwon Chun, Duyoung Choi, Alireza Kargar, Renkun Chen, Zhaowei Liu, and Sungho Jin. The third is currently being prepared for submission to a SCI journal, "Two-layered tandem structures with copper-contained spinel metal oxide nanoparticles", Tae Kyoung Kim, Bryan VanSaders, Elizabeth Caldwell, Sunmi Shin, Youngjin Kim, Zhaowei Liu, Renkun Chen, and Sungho Jin. The dissertation author was the primary investigator and author of these aforementioned three papers.

2.1 Introduction

Solar receivers in concentrating solar power (CSP) plants is composed of spectrally selective coating (SSC) layers coated on metal tube and heat-transfer fluid (HTF) flowing inside tube [1], as shown in Fig. 2-1. By the absorption of concentrated solar energy, HTF and the metal tube with SSC layers are heated up to so high temperature of ~750ºC in the case of next generation CSP plants that they can emit infrared (IR) spectrum in the range longer than λ= ~2.5μm, as simulated in Fig. 2-1(b). And natural sunlight reaching our earth shows the irradiation spectrum like the green graph in Fig. 2-1(b) and the part of solar irradiation spectrum with high energy density is close to zero also near λ=2.5μm. Therefore it is desirable that ideal SSC layers can absorb solar spectrum as much as possible from ultraviolet (UV) to near-IR spectrum of 2.5 μm and can reflect near-IR spectrum longer than λ=2.5μm, which can increase the conversion efficiency of solar to thermal energy called as figure of merit (FOM).

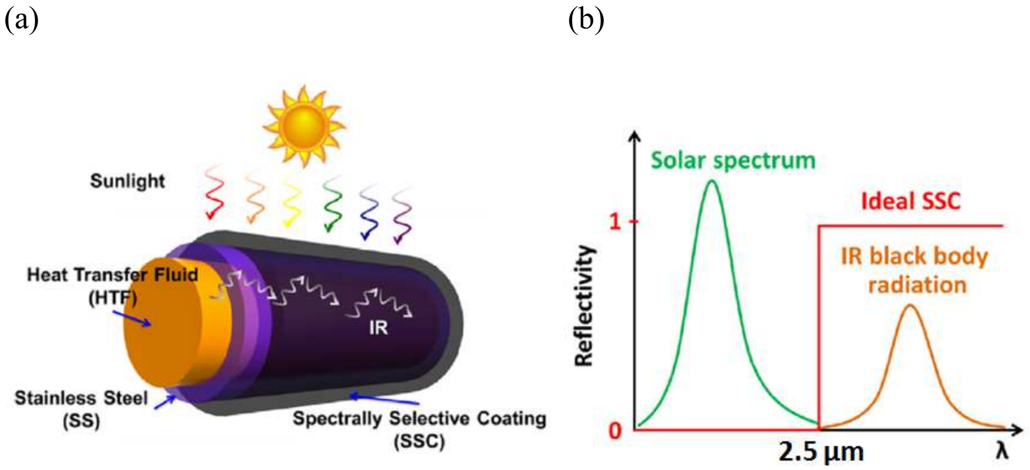

Figure 2-1. (a) The concept image of solar receiver tube, and (b) the optical property of solar spectrum, IR black body radiation, and an ideal SSC layer [1]. (solar spectrum: irradiation to the earth, IR black body radiation: IR emission from a receiver tube, and Ideal SSC: the reflectivity of ideal solar receiver).

Conventional solar receiver in CSP plant is made of Pyromark black paint which can be purchased commercially. Pyromark-coated samples with Inconel 625 substrate begin degrading after 100h isothermal annealing at 750ºC in air [2], as shown in Fig. 2-2 which was plotted by Sandia National Laboratories. When calculating figure of merit (FOM) for Pyromark-coated samples in our lab using reflectance measurement, FOM of Pyromark sample is still below 90%, which will be explained later in this chapter.

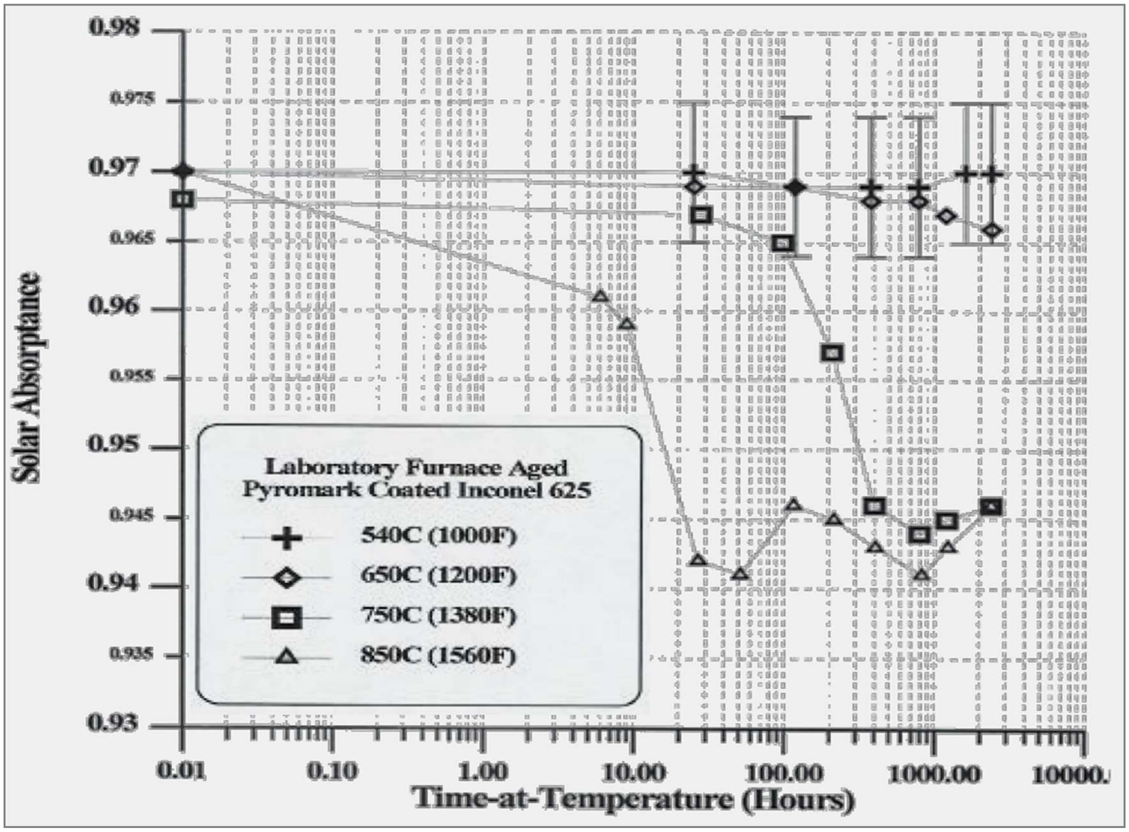

Figure 2-2. Absorptance change with time of Pyromark samples annealed at different temperature under air atmosphere [2].

Therefore, it is necessary to develop new SSC layers with better thermal stability and higher FOM for the next generation CSP plants. The milestones of DOE's SunShot project as followings; solar receiver's temperature = 750°C, FOM ≥ 90%, and FOM endurance (after 500h at 750°C in air) ≥ 98% of the initial FOM. In order to reach these goals, three approaches have been carried out to fabricate solar receivers with high performance, including SSC layer of Si boride-coated Si core-shell nanoparticles [3], tandem-structured SSC layer using CuO nanowires and Co_3O_4 nanoparticles [4], and 2-layered tandem structures composed of a porous $CuFeMnO_4$ layer and a dense $CuCr_2O_4$ layer.

2.2 Materials and Methods

2.2.1 Fabrication of Si boride-coated Si core-shell nanoparticles

Si nanoparticles (~99.9 % purity) with average particle size of 100 nm as a core material and $NaBH_4$ (~98 % purity) powder as a boron source were purchased from Alfa Aesar (Ward Hill, MA). For sample preparations, the Si nanoparticles and $NaBH_4$ powder were thoroughly mixed together by repeated grinding with a mortar and a pestle in a globe box under Ar atmosphere. A quartz tube was sealed with the mixed powders and Ar gas, and heat-treated at 500 ^{o}C for 2 days which enabled $NaBH_4$ in the form of a molten salt to make a diffusional reaction with the surface atoms of Si nanoparticles to form a Si boride shell. After the reaction, the residual unreacted $NaBH_4$ was dissolved away with de-ionized (DI) water, and the core-shell nanoparticles were collected with a centrifuge followed by freeze-drying. To crystallize Si boride nanoshell, an annealing process of 900 ^{o}C / 5h under Ar atmosphere was employed. After annealing, some portion of the shell remained amorphous. An additional shell-passivation process was applied at 550 ^{o}C for 1hr in an oxidizing atmosphere of air in order to convert the amorphous phase in the shell to a passivating borate phase (presumably a glassy borosilicate phase that would not oxidize further) as a part of the shell structure. Without this stabilizing heat treatment step, the oxidation resistance was inferior on high temperature exposure, which was observed with weight gain by thermo-gravimetric analysis (TGA). For the comparative phase analysis, SiB_3 particles, and SiB_6 particles were prepared by ball-milling of arc-melted metal ingots with the same stoichiometric compositions.

2.2.2 Synthesis of CuO nanowires and Co_3O_4 nanoparticles

Thermal growth of copper oxide nanowires (NWs) was made by annealing copper foil in air atmosphere [5, 6]. As a pretreatment procedure, the purchased copper foil (Alfa Aesar, 50 μm thick) was cleaned with hexane, acetone, isopropyl alcohol and distilled water, followed by drying with air blowing. The copper foil was heated with a rate of 20 $^{o}C/min$ up to 500 ^{o}C and held for 5 h under air atmosphere. After cooling down to room temperature, a dense array of copper oxide NWs was obtained on copper foil. The image of the copper oxide NWs was observed by scanning electron microscopy (SEM) and the crystal structure of nanowires was analyzed with X-ray diffraction analysis (XRD), transmission electron microscopy (TEM) and energy-dispersive X-ray spectroscopy (EDX).

A two-step synthesis method was used to produce cobalt oxide (Co_3O_4) nanoparticles (NPs), with the first step of precipitation into cobalt hydroxide and the second step of hydrothermal synthesis to make cobalt oxide NPs. The precursor cobalt chloride ($CoCl_2{\cdot}6H_2O$) was purchased (Alfa Aesar) and dissolved in distilled water in concentration of 1.0 M. To induce a precipitation of $Co(OH)_2$, 10.0 M NaOH aqueous solution was added gradually until the pH of the mixed solution reached 11.5. The mixed solution was placed inside a Teflon liner of high pressure steel container and subjected to a hydrothermal synthesis for 20 h at 150 °C. After the synthesis, the remaining precursor solution and reaction byproducts were removed with repeated washing in distilled water followed by centrifuging, after which freeze-drying for 1 day was employed to dry the cobalt oxide nanoparticles. The dried particles were annealed at 750 °C for 2 h to fully crystallize into Co_3O_4 NPs. The processed Co_3O_4 NPs were composed of mainly particles having 100-200 nm in average size.

2.2.3 Fabrication of tandem structure with CuO NWs and Co_3O_4 NPs

Based on the evaluation of optical reflectance of CuO NWs alone and that of Co_3O_4 NPs alone (see Fig. 2-19(a)), it is seen that copper oxide nanowires (NWs) can absorb a large amount of visible spectrum. By contrast, the coated layer of Co_3O_4 nanoparticles (NPs) exhibits a much higher optical reflectance in the visible range than CuO NWs, but shows an advantage of absorbing more near-IR spectrum than the CuO NWs. Therefore, a combined tandem structure of copper oxide NWs and cobalt oxide NPs was devised to take advantage of both materials unique characteristics and achieve higher absorption of sunlight in both near-IR and visible spectrum. The SEM micrograph of Fig. 2-19(b) shows one example of such a combined tandem structure of CuO NWs and Co_3O_4 NPs. This concept of tandem structure formation for optically improved SSC layer is more clearly illustrated by schematic diagrams of Fig. 2-3.

According to Fig. 2-3, vertically aligned CuO NWs and spherical Co_3O_4 NPs can be combined in two different configurations. One way is to coat the vertical CuO NWs with cobalt oxide NPs by means of spray-coating, or dip-coating method which makes micro-cone type of structure formed with cobalt oxide NPs, as shown in the left side procedure of Fig. 2-3. Another way of tandem structure formation is to have the copper oxide NW layer itself separated from the copper foil substrate by wet-etching removal of Cu, followed by attachment of it on top of micro-layer of cobalt oxide NPs pre-deposited on Inconel substrate surface, as represented by the right side procedure of Fig. 2-3.

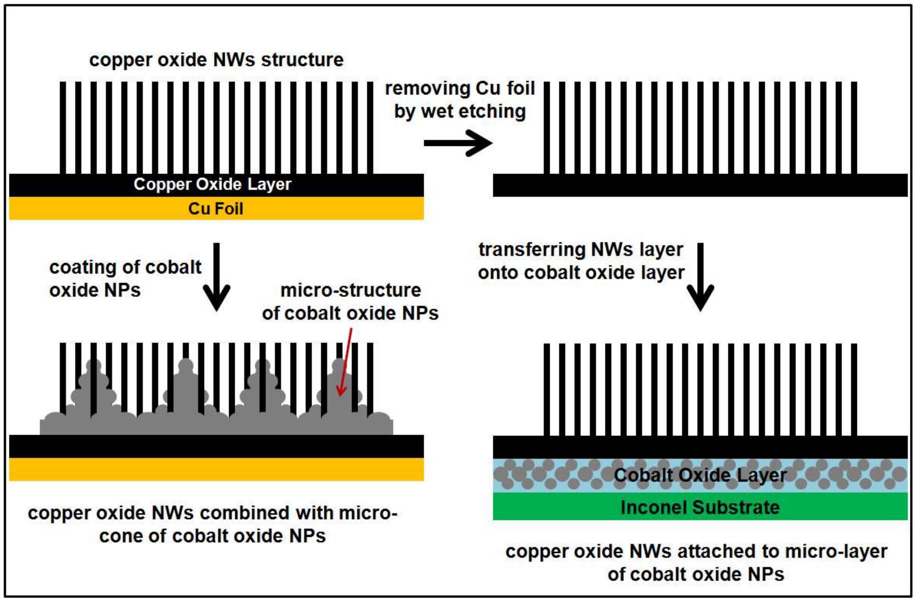

Figure 2-3. Schematic illustration of the tandem-structured spectrally selective coating (SSC) layer concepts including coating cobalt oxide NPs into vertically aligned copper oxide NWs as well as transferring of copper oxide NW layer onto the layer of cobalt oxide NPs.

Spectrally selective coating (SSC) layer of copper oxide nanowires (NWs) combined with cobalt oxide (Co_3O_4) nanoparticles (NPs), was fabricated with three different methods including spray-coating, dip-coating, and transferring.

For the preparation of coating solution for spray-coating of the synthesized cobalt oxide NPs, phenyl-methyl polysiloxane resin (purchased from Evonik (Germany, SILIKOPHEN P 80/X)) was utilized as a binder resin. After diluting to 6 wt% by adding a cosolvent of isobutanol/xylene (1/3 v/v ratio) to the purchased resin solution, cobalt oxide NPs were then added to the diluted binder solution with a composition of 4:1 (w/w) (cobalt oxide: pheny-methyl polysiloxane). In the final coating solution, the concentration of total solid consisting of cobalt oxide and a binder became 18 wt%. The nanoparticle dispersion was further improved by sonication followed by ball-mixing for 1 day. On the surface of copper oxide NWs (which are semi-vertically aligned on Cu foil surface), the final cobalt oxide NPs coating solution was spray-coated (left side schematics in Figure 5) after which the binder resin was cured at 250 ^{o}C for 1 h in air atmosphere.

Cobalt oxide solutions with different concentrations of 18 wt% and 6 wt% were used for the dip-coating of cobalt oxide NPs into the copper oxide NW structure. The cobalt oxide solution of 18 wt% prepared as described above was used for dip-coating into copper oxide NW structure with different dipping methods, including a continuous longer time dipping (10 min) without making the solution container to be vacuum state, and a dipping with 1 cycle of vacuum (20 sec) and venting. For a diluted coating solution with a solid concentration of 6 wt%, the previous 18 wt% solution was diluted by a factor of 3 by adding isobutanol/xylene (1/3 v/v). With this diluted cobalt oxide solution (6 wt%), copper oxide NW structure was dip-coated using 1 cycle of vacuum/venting and 3 cycles of vacuum/venting procedure. For all these dip-coating procedures, the drying and curing procedure was carried out at 250^{o}C for 1 h in air environment.

For an alternative tandem structure by transferring of copper oxide NW layer and placing it on top of cobalt oxide NP layer (right side schematics in Figure 5), the copper oxide NWs grown thermally on copper foil was separated from the copper foil by wet-etching removal of remaining Cu in a mixed aqueous solution of 3.0 M iron chloride solution and 37% hydrochloric acid solution (25/1 w/w). Before transferring, thin binder resin layer of phenyl-methyl polysiloxane was coated on cobalt oxide NP layer (30 μm) formed on Inconel 625 substrate by spray-coating at 40 psi pressure, using the cobalt oxide NP solution with 18 wt% concentration. The separated copper oxide NW layer was transferred onto the binder resin layer, followed by drying and curing at 250 ^{o}C for 1 h in air atmosphere.

2.2.4 Synthesis of spinel Cu-contained metal oxide nanoparticles

Two types of black oxide nanoparticles with spinel structure were synthesized using the below procedure in Fig. 2-4. For the synthesis of copper chromites, copper chloride ($CuCl_2·2H_2O$) aqueous solution of 1 M was mixed uniformly with chromium chloride ($CrCl_3·6H_2O$) aqueous solution of 1 M with vigorous stirring for 5 h, followed by co-precipitation into Cu-Cr hydroxides by dropping 10 M NaOH solution. After mixing the co-precipitated hydroxides for 2 h, hydrothermal synthesis was made in 45 mL autoclave with Teflon liner at 200 ^{o}C for 20 h. As a post-treatment, centrifuged particles were dried with freeze-dryer and finally crystallized at high temperatures (550 ^{o}C, 750 ^{o}C) in air atmosphere. To synthesize spinel Cu-Fe-Mn oxides nanoparticles, the overall procedure was same as that of copper chromites excluding precursors which included copper chromite ($CuCl_2·2H_2O$), iron chloride ($FeCl_3·6H_2O$), and manganese chloride ($MnCl_2·4H_2O$).

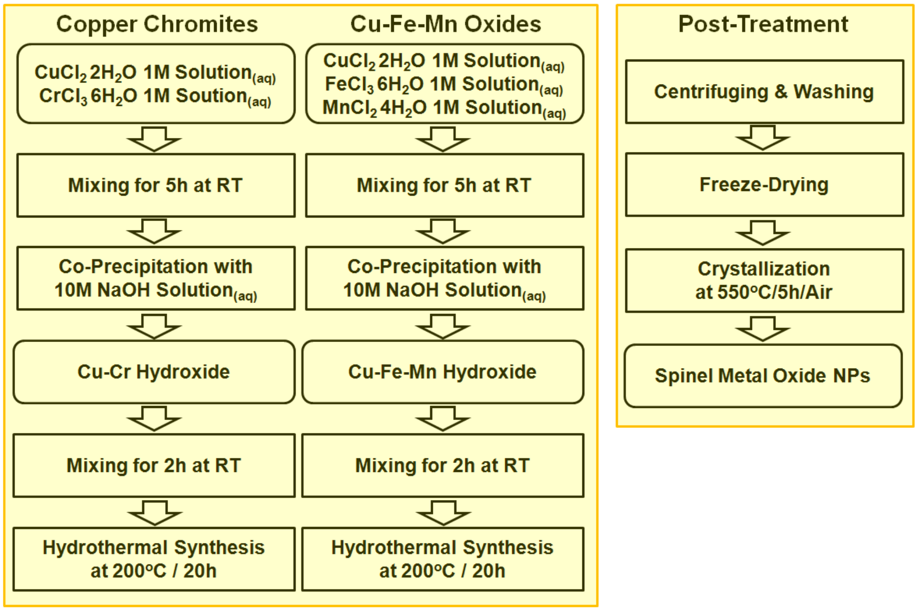

Figure 2-4. Synthesis procedures of copper chromites and Cu-Fe-Mn oxide particles.

2.2.5 Fabrication of tandem structure with $CuFeMnO_4$ and $CuCr_2O_4$ NPs

Using Cu-Fe-Mn oxide nanoparticles and copper chromite nanoarticles, the spectrally selective coating (SSC) layers were fabricated with the procedure shown in Fig. 2-5. Resin (binder) solution of 7 wt% was made of methyl phenyl polysiloxane solution (SILIKOPHEN P80/X, Evonik) diluted with additional solvents (isobutanol, and xylene). In the case of dense SSC layers, black oxide particles were dispersed in the binder solution in weight ratio of 1/0.25 (particles/resin) using a slow ball-milling for 24 h, after which spray-coating was carried out on to Inconel 625 substrate. And then the coated layer was dried at room temperature for 1 day, followed by curing and annealing procedures which were comprised of continuous heat treatments in air (RT - 100 ^{o}C for 10 min – 250 ^{o}C for 2 h – 550 ^{o}C / 3h – 750 ^{o}C / 2 h – RT) with temperature increasing slowly in 5 ^{o}C/min. For porous SSC layers, both black oxide nanoparticles and polymer beads were dispersed in the binder solution in weight ratio of 1.0/0.8/1.1

(particles/beads/resin) with probe-type sonication. The volume ratio of 3 materials for porous layers was calculated to be approximately 1/5/6 (particles/polymer beads/resin). Except those solution compositions, other procedures to make porous SSC layer were same as that of dense SSC layers aforementioned.

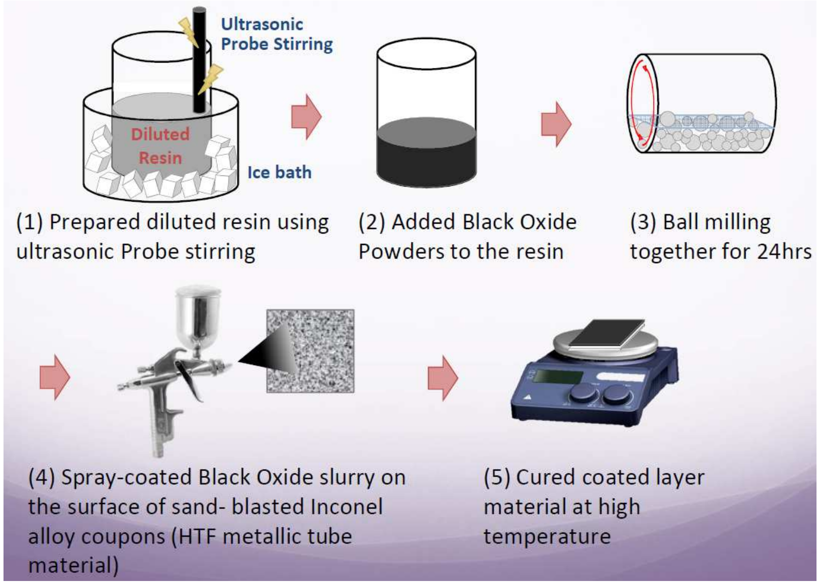

Figure 2-5. Scalable procedure to fabricate the spectrally selective coating layer of solar receivers using spray-coating method.

2.2.6 Characterization

X-ray diffraction (XRD) analysis

X-ray diffraction (XRD) analysis was carried out to investigate the crystal structure of copper oxide nanowires (NWs), cobalt oxide nanoparticles (NPs), spinel-structured copper iron manganese oxide ($CuFeMnO_4$) NPs, and spinel-structured copper chromite ($CuCr_2O_4$) NPs. Crystal structures of synthesized materials were characterized by Bruker D2 Phaser XRD with Cu K_α (λ=0.154 nm) as the radiation source. The scanning of 2θ angle (degree) was made in the range of 10 °-80 ° with a scanning rate of ~0.0406 deg/step/sec.

Scanning electron microscopy (SEM)

By SEM (Oxford, acceleration voltage of 10 kV) were imaged the structures of copper oxide NWs, cobalt oxide NPs, $CuFeMnO_4$ NPs NPs, $CuCr_2O_4$ NPs, the surface morphology of spectrally selective coating (SSC) layers, and tandem structured SSC layers.

Energy-dispersive X-ray spectroscopy (EDX)

The copper oxide phases existing at different positions in the cross-sectional area of copper oxide NWs structure were analyzed using energy-dispersive X-ray spectroscopy (EDX) installed with scanning electron microscopy (SEM) (Oxford), with an acceleration voltage of 10 kV.

Transmission electron microscope (TEM)

Synthesized nanomaterials were analyzed with transmission electron microscope (TEM) (FEI Tecnai F20 G^2) operated at the acceleration voltage of 200 kV in bright field (BF) mode and high resolution (HR) mode, followed by fast Fourier transform (FFT) analysis to confirm the crystal structures.

Electron energy loss spectroscopy (EELS)

The presence of boron in the shell layer of Si-Si boride NPs was confirmed by electron energy loss spectroscopy (EELS) for estimation of boron content. For EELS analysis, the sample was imaged with TEM (FEI Tecnai TF-20 FEG) operated at 200 kV in high-angle annular dark-field (HAADF) scanning transmission electron microscope (STEM) mode. Line scanning of EELS was made in STEM mode using a nominal 1 nm electron beam and a Gatan Enfina DigiPEELS spectrometer.

Thermo-gravimetric analysis (TGA)

With thermo-gravimetric analysis (TGA), the thermal oxidation resistance was evaluated by measuring the total weight gain of particles during heating in a pure oxygen atmosphere for Si - Si boride core-shell NPs. Measurements were carried out at two different holding temperatures of 750 ^{o}C and 850 ^{o}C. Samples were heated at a rate of 20 ^{o}C/min to the maximum temperatures and held there for 2 hrs.

Fourier transform infrared spectroscopy (FT-IR)

Fourier transform infrared spectroscopy (FT-IR) (Nicolet 6700 analytical MCT FT-IR Spectrometer) was used to analyze the effect of Si boride shell on the IR absorbance behavior of the annealed Si-Si boride NPs and bare Si NPs. The spectrum was scanned with the data spacing of 0.4 cm^{-1}.

Visible/infrared (IR) reflectance measurement system

Visible/infrared (IR) reflectance measurement system was fabricated with an integration sphere (4″ LabSphere®, Spectraflect® coated) assembled with an Andor® Shamrock 303i spectrometer equipped with Si and InGaAs-based detectors. The optical reflectance of SSC layers was measured with incidence angle of 12.5^{o} in the spectrum range of 300-2000 nm for SSC layers at room temperature.

Figure of Merit (FOM)

To compare the conversion efficiency of solar to thermal energy in SSC layers of solar receivers, figure of merit (FOM) value was evaluated for various SSC layers. The figure of merit (FOM) means the ratio of absorption energy subtracted by emission energy released from a heated solar receiver compared to solar energy irradiating to the solar receiver and is defined as follows (Equation 1).

$$F = \frac{\int_0^\infty \big(1 - R(\lambda)\big) I(\lambda) d\lambda - \frac{1}{C}\left[\int_0^\infty (1 - R(\lambda)) B(\lambda, T) d\lambda\right]}{\int_0^\infty I(\lambda) d\lambda} \qquad (1)$$

where R(λ) is the spectral reflectivity, I(λ) is the spectral solar irradiance per square meter as defined by the reference solar spectral irradiation(ASTM G173), B(λ,T) is the spectral thermal emission of a black body at temperature T, and C is the concentration ratio. In this research, the wavelength ranges from λ=300 nm to λ=20 μm to calculate FOM value and the reflectance measured at 2 μm is extrapolated to be the reflectance in IR spectrum from 2 to 20 μm. For large concentration ratio of mirror-focused sunlight such as solar power tower type of CSP systems, the optical absorption (related to optical reflectance properties) is the dominant factor rather than emitted energy from solar recevier. FOM was calculated with T = 750 °C and C = 1000 which is the conditions of the next generation CSP plant.

FOM endurance evaluation

FOM endurance of the fabricated SSC layers was evaluated with thermal test in air atmosphere. Thermal cycling from room temperature to 750 °C was carried out with 100 cycles and isothermal annealing at 750 °C for 500 h under air environment was applied for SSC layers including $CuFeMnO_4$(PT)/$CuCr_2O_4$(DB), Co_3O_4(PT)/Co_3O_4(DB), Lab-coated Pyromark(DS), and CSP company-made Pyromark sample as described in Fig. 2-6 and Table 2-1. (PT: a porous top layer, DB: a dense bottom layer, DS: a dense single layer).

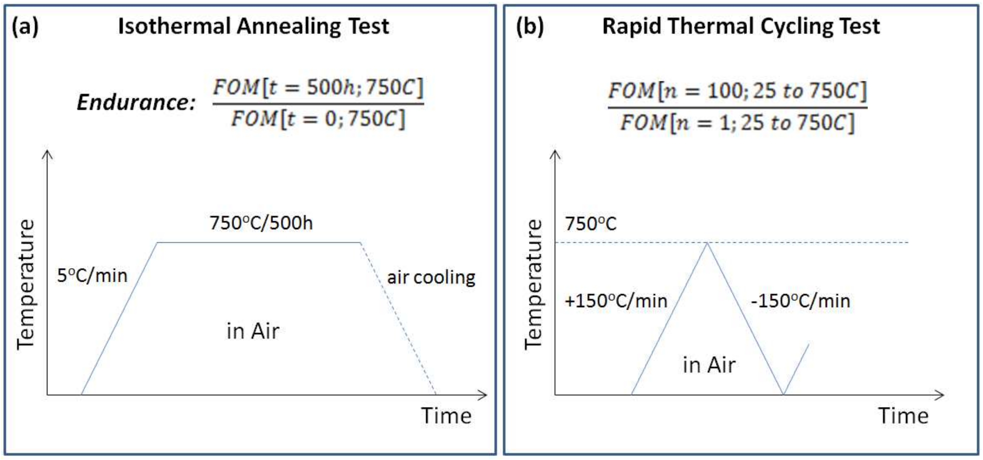

Figure 2-6.Temperature profile for thermal test to evaluate FOM endurance of SSC layers including (a) isothermal annealing tests and (b) rapid thermal cycling tests.

Table 2-1. 4 types of SSC samples evaluated with thermal test in air atmosphere.

Test Samples	CFM(PT)/$CuCr_2O_4$(DB)	Co_3O_4(PT)/Co_3O_4(DB)	Pyromark (DS) (Lab-Coated)	Pyromark (CSP Company)
	synthesized NPs-solution-coating	synthesized NPs-solution-coating	commercial paint-solvent modified	commercial paint-coated by CSP comp.

Adhesion evaluation of coating layer by a tape test

The tape testing method was used to determine the adhesion quality of SSC layers to Inconel 625 substrates. This method is a modified version of ASTM D3359. Pressure sensitive tape of 3M 600 with ¾ inch width was used for the adhesion evaluation. A strip of 3M 600 tape was attached to the coating layer and pressed firmly across the surface of the SSC layer using a rubber eraser. Within 90±30 sec, the tape was removed rapidly by shearing (pulling in plane with the surface). For evaluation, photos of both a removed tape and a substrate were taken and the percentage of survived area was calculated compared to total sample area without considering the edge area by image processing with ImageJ software.

2.3 Results and Discussion

2.3.1 Si boride-coated Si core-shell NPs resistant to thermal oxidation

2.3.1.1 Shell formation and composition

Sodium borohydride ($NaBH_4$) powder material starts to melt at 400 ^oC to form a molten salt of Na^+ $[BH_4]^-$ [7], followed by decomposition reactions at 450 ^oC into [NaH + B + $1.5H_2$] or [Na + B + $2H_2$] [8]. During the shell-forming procedure occurring when the temperature reaches 500 ^oC, phases such as a molten salt phase, a decomposed gas phase (H_2) and solid phases can coexist. In this mixed-phase state at 500 ^oC, boron atoms from $NaBH_4$ can diffuse and react with Si atoms to form a desirable Si boride nanoshell on the surface of Si nanoparticles, which can serve as an oxidation-resistant protective layer.

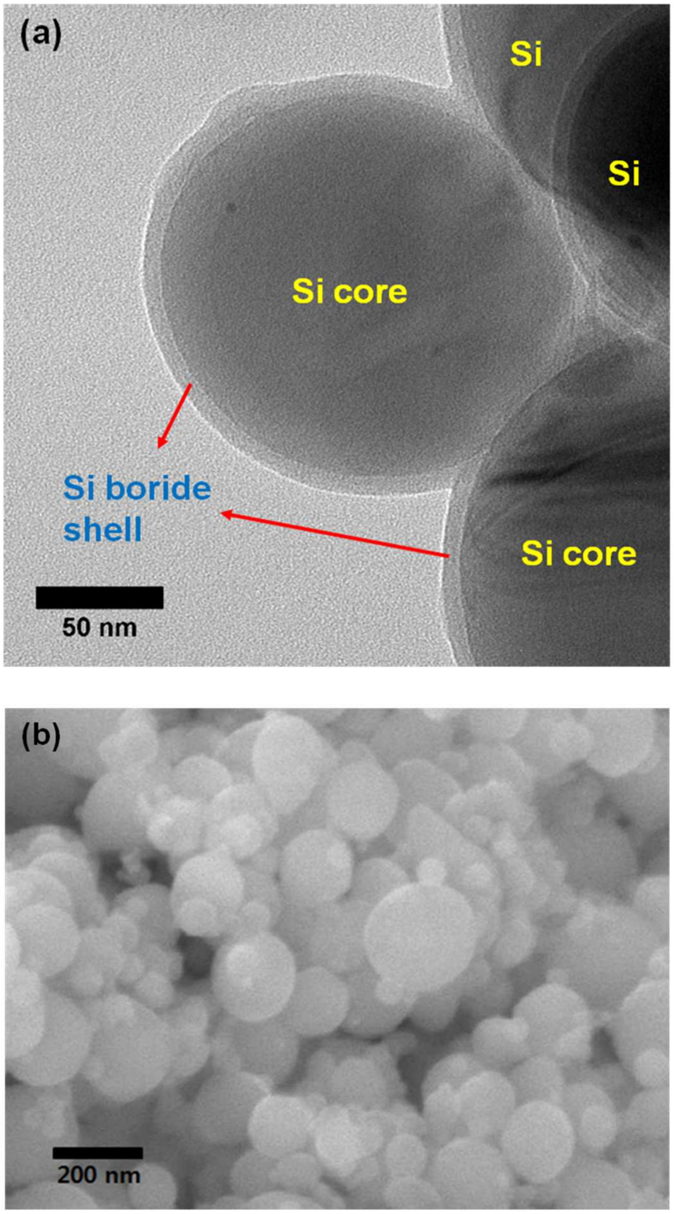

Figure 2-7. Microstructural images of as-made Si - Si boride core-shell nanoparticles ; (a) TEM image showing 10~20 nm thick Si boride shell, and (b) lower mag SEM image of overall core-shell nanoparticles.

Various structural and compositional analyses of the $NaBH_4$–reacted Si nanoparticles were performed using SEM, TEM, EELS and FT-IR. The microstructures of as-made, core-shell nanoparticles of Si - Si boride are shown in Fig. 2-7. The TEM image, Fig. 2-7(a), clearly indicates the core-shell configuration with Si core (~ 150 nm diameter) and a well defined and conformal Si boride shell (10~20 nm). The overall morphology and size distribution of Si boride-coated Si nanoparticles are depicted in the SEM image of Fig. 2-7(b), which shows some distribution of the particle diameter of 50-200 nm, arising from the size distribution of the starting Si nanoparticles.

Shown in Fig. 2-8 are TEM micrograph (Fig. 2-8(a)) and the corresponding FFT pattern (Fig. 2-8(b)) for the core-shell NPs with the annealed and passivated Si boride shell. The core is a polycrystalline silicon which is represented by main (111) crystal structure with P1 pattern as well as other crystalline structures such as Si (311) with P4 pattern, as shown in Fig. 2-8(b). The shell is composed of the mixture of some crystalline phases (the inset in Fig. 2-8(a)) including Si boride (P2, and P3 patterns in Fig. 2-8(b)) and some amorphous phases including Si-B amorphous phase, borosilicate and silica which was formed during the annealing and shell-passivation procedure. The P2 pattern in Fig. 2-8(b) has d-spacing of 2.8142 □ which corresponds to the d-spacings of SiB_3 (104), SiB_6 (260), or SiB_6 (351) as summarized in the Table □. Another crystalline pattern, P3 in Fig. 2-8(b) has d-spacing of 2.5633 □ which is close to the d-spacings of SiB_3 (113), SiB_3 (202), SiB_6 (162) or SiB_6 (450).

EELS analysis was utilized to confirm the existence of boron as well as the composition in the shell of the core-shell nanoparticles. The diameter of Si-Si boride NP analyzed by EELS was approximately 80 nm in STEM image as indicated in Fig. 2-9(a) where the shell thickness of the core-shell particle was about 10 nm. The line scanning of EELS analysis was made for the region along 28 nm length along the direction from the core side (the core covered with shell) to the shell side (near the edge of the particle).

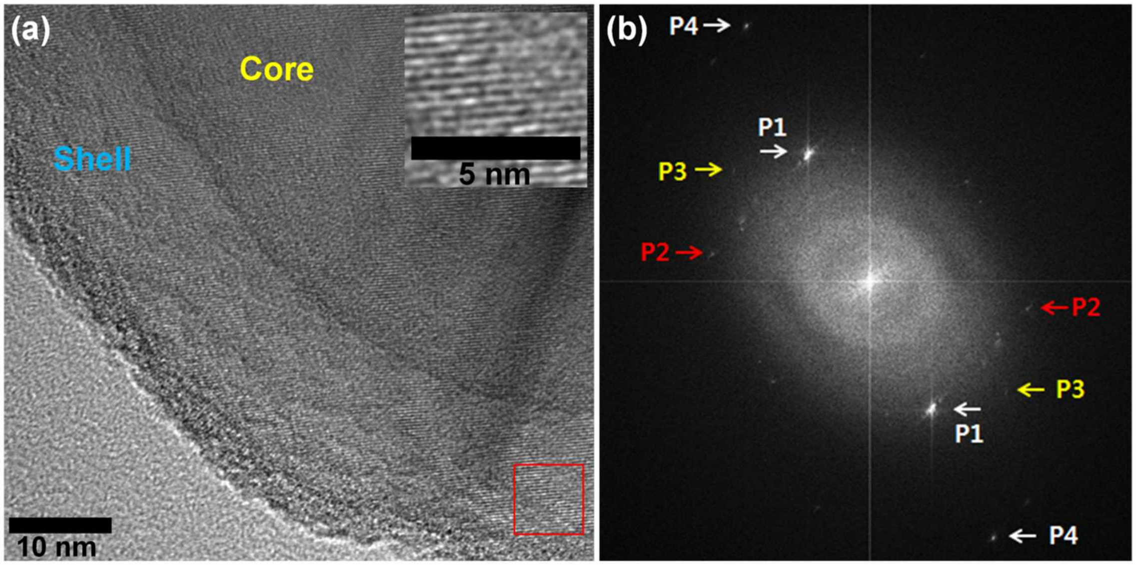

Figure 2-8. (a) TEM image near the shell area of a Si - Si boride core-shell nanoparticle with the inset showing the lattice image taken from red-lined square area in the shell area (lower right in Fig. 2-8(a)), and (b) corresponding FFT patterns for the image (a) showing some crystal phases (P2, P3 in (b)).

Through this line-scanning in STEM mode, EELS spectrum could be measured for each Si and B, as shown in Fig. 2-9(b). Line [I] in Fig. 2-9(b) and (c) indicates the boundary between the shell-coated core region (the left side of line [I]) and pure shell region (the right side of line [I]). For the line scanning of the core part (the left side of line [I] in Fig. 2-9(b)), the electron beam passes the top shell, Si core, and bottom shell of the spherical particle in that order. For the line scanning of the shell part (the right side of line [I] in Fig. 2-9(b)), the beam goes through only the shell with progressively less material scanned as the beam moves out to the edge of the spherical particle.

The fractional compositions of core and shell in Si-Si boride NP were calculated (Fig. 2-9(c)) using the EELS spectrum which had the counts of energy loss signal for every 1 nm step (Fig. 2-9(b)). After a single spectrum (60 eV to 725 eV) was acquired at every 1 nm, the many spectra were then converted into a line scan graph.

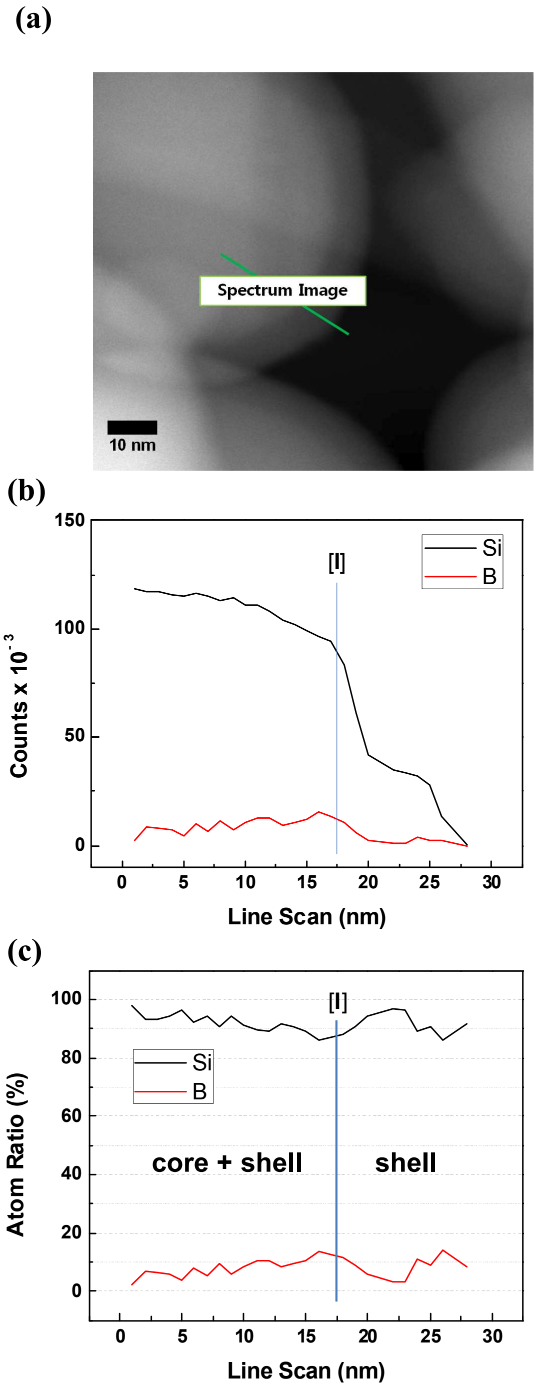

Figure 2-9. (a) STEM image showing the line-scan part (green line, spectrum image) of EELS in the core-shell Si - Si boride NPs, (b) EELS spectrum showing the counts of energy loss signal for each element (Si and B) on line-scanning from the core side to the shell side, and (c) the composition of core side and shell side in Si-Si boride core-shell nanoparticle, calculated from the EELS spectrum.

The principal edge values of energy loss for each element, 99 eV and 188 eV were used to measure signals of Si and B element, respectively. The shell part is detected approximately from 17 nm to 28 nm on the Line Scan axis in Fig. 2-9(b) and (c), if considering both STEM image and EELS spectrum. The core part is thought to be from 0 nm to 17 nm on the Line Scan axis, where both core material (Si) and shell materials (Si, and Si boride) exist.

It can be estimated from Fig. 2-9(c) that the atom ratio of Si/B in the shell part is 5/1 ~ 30/1, which means that B content is a smaller amount than Si in the overall area of the shell. In the phase diagram of Si-B alloy, the alloy with Si/B atom composition of 5/1~30/1 is composed of two phases including Si and SiB_3 [9]. Therefore, the shell of the annealed Si-Si boride NPs is thought to consist of binary phases including crystalline SiB_3 phase and Si phase except amorphous phasesas observed in TEM image and FFT pattern of Fig. 2-8.

2.3.1.2 Effect of Si boride shell on the absorbance of IR spectrum

FT-IR measurement was made for the annealed Si - Si boride NPs and bare Si NPs in order to compare infrared (IR) absorbance behaviors of these two types of particles in relation with the effect of Si boride shell. Bare Si particles have the strong absorbance peaks in the region of 1100 ~ 1000 cm^{-1} and 880 ~ 834 cm^{-1}, as shown in Fig. 2-10(a). The absorbance peak of 1100 ~ 1000 cm^{-1} was reported for the vibration of Si-O bonding and the peak of 880 ~ 834 cm^{-1} results from the vibration of O-Si-O bonding [10]. The synthesized core-shell NPs display a new absorbance peak at 940 cm^{-1} and a new broad band composed of two peaks in the region of 777 ~ 677 cm^{-1}, which are expected to be affected by boron-containing bonds of the Si boride shell formed by the diffusion of boron atoms into Si surface based on the following analysis.

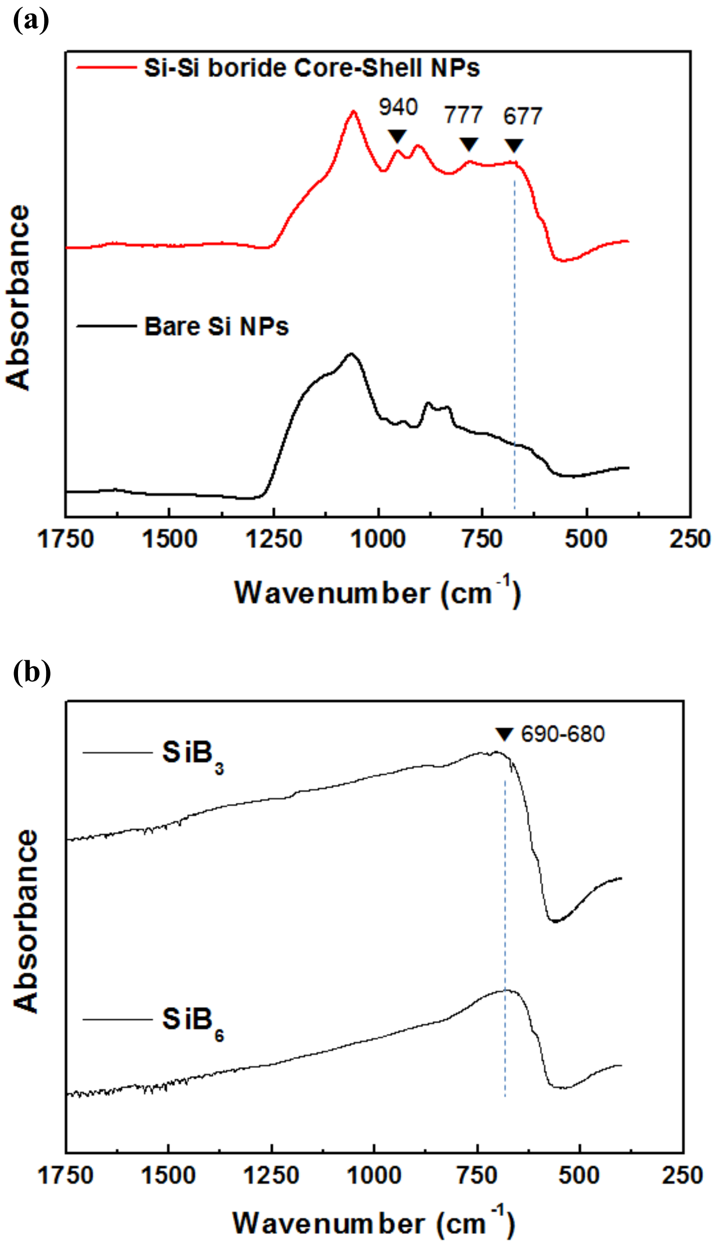

Figure 2-10. FT-IR analysis showing (a) Si - Si boride NPs have new absorbance peaks containing a broad band with two peaks of 777 ~ 677 cm^{-1} and another peak of 940 cm^{-1}compared to bare Si NPs, and (b) the main absorbance is made at 690-680 cm^{-1} for SiB$_3$, and SiB$_6$ material.

As illustrated in Fig. 2-10(b), the SiB_3 and SiB_6 particles have the main absorbance peaks in the range of 690 ~ 680 cm^{-1}. The vibration band for B-B bonding was reported to occur approximately in the range of 1100 ~ 600 cm^{-1} [11]. One absorbance peak (677 cm^{-1}) of the broad band (777 ~ 677 cm^{-1}) for Si - Si boride NPs matches with the main absorbance peaks of SiB_3 (690 ~ 680 cm^{-1}) and SiB_6 (690 ~ 680 cm^{-1}) particles. Si-O-B bonding was reported to have the absorbance peak in two wavenumbers of 930 and 680 cm^{-1} [10], which seems to represent a similar absorption behavior to that of the Si - Si boride NPs with the absorbance peaks (940 cm^{-1} and 677 cm^{-1} in Fig. 2-10(a)). Also, B-O bonding was reported to make an absorption at the wavenumber of 1400 cm^{-1} [10], where the synthesized Si - Si boride NPs show the broad and weak absorbance peak, as can be seen in Fig. 2-10(a). Based on this FT-IR analysis, it can be concluded that the new absorbance peaks of Si-Si boride NPs result from the formation of Si boride shell which is composed of boron-reacted materials including the forms of Si-B alloy (Si boride), and SiO_2-B_2O_3 (borosilicate).

2.3.1.3 Improved resistance to thermal oxidation

The thermal oxidation resistance was measured with TGA in a pure oxygen atmosphere for Si - Si boride nanoparticles. The total weight gain of particles resulting from the thermal oxidation was compared to that of bare Si nanoparticles. We utilized accelerated oxidation method by using pure oxygen atmosphere at high temperatures.

Shown in Figure 2-11 are the comparative TGA analysis data showing the enhanced thermal oxidation resistance of the Si - Si boride core-shell NPs compared to the bare Si NPs. Thermal oxidation was measured based on the weight change of TGA

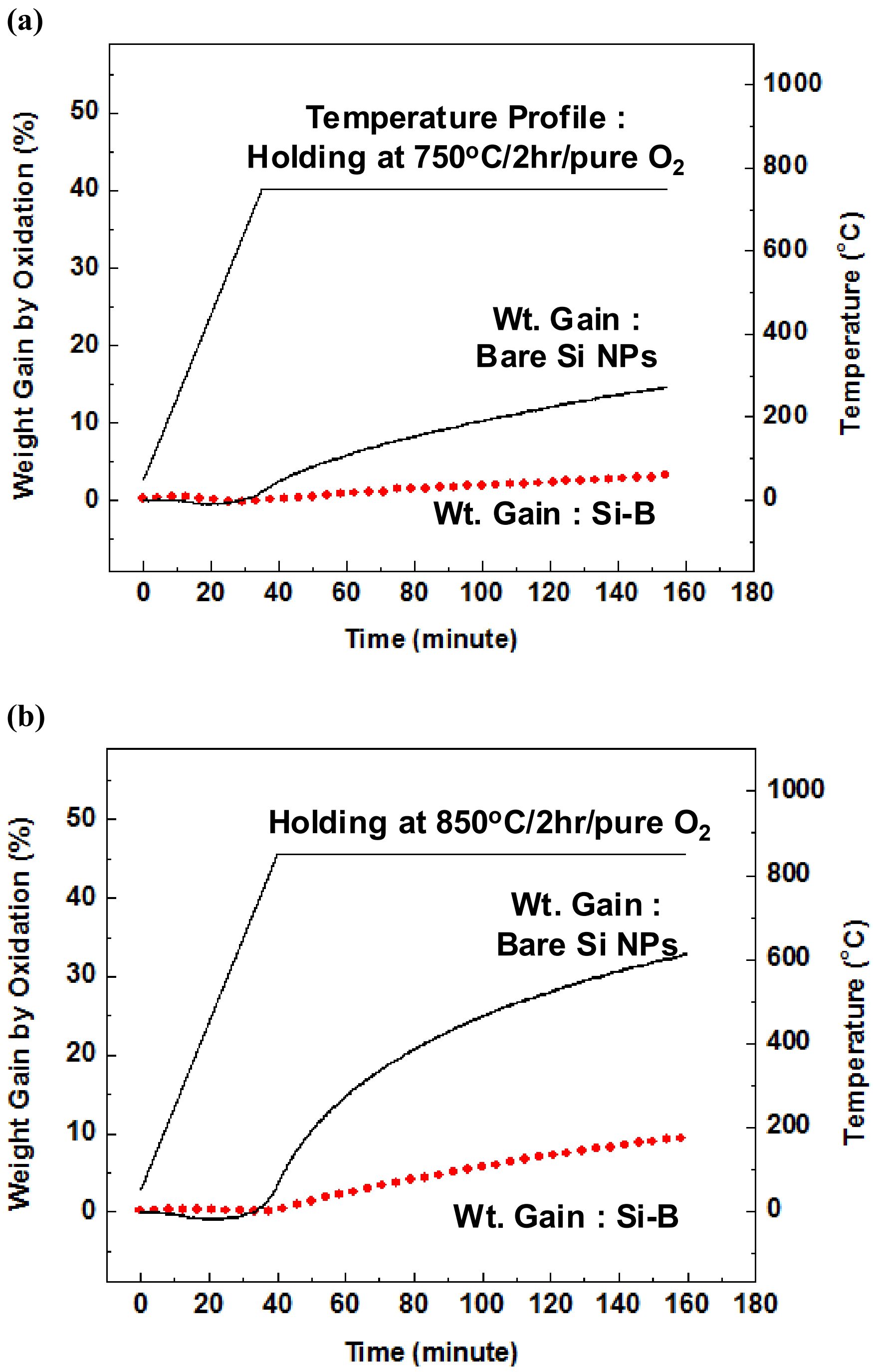

Figure 2-11. Accelerated TGA analysis comparing bare Si nanoparticles to the surface-protected, core-shell structured Si - Si boride nanoparticles (Si-B), (a) at 750 °C, and (b) at 850 °C in pure oxygen atmosphere.

during a temperature increasing step and a temperature holding step at 750 ^{o}C (Fig. 2-11(a)) and 850 ^{o}C (Fig. 2-11(b)). These accelerated oxidation tests in pure oxygen atmosphere by TGA indicate that the core-shell Si-Si boride NPs with boron-alloyed shells exhibit a much higher resistance to thermal oxidation than bare Si NPs. After holding at 750 □ for 2 h in TGA test, the core-shell NPs had a much smaller amount of weight gain (3.2 wt%) by a factor of 4.6 compared to that of bare Si NPs (14.6 wt%). Similarly as for the 750 ^{o}C TGA, the 850 ^{o}C TGA results also indicate that the weight gain (9.4 wt%) of the core-shell nanoparticles decreased much by a factor of 3.5 in comparison to bare Si NPs (33 wt%), after the temperature holding step of 850 ^{o}C / 2 h.

This significantly enhanced oxidation resistance of the core-shell structured Si - Si boride NPs results from the contribution of the conformally present shell layer which consists of crystalline Si borides (SiB_3, or SiB_6) and other vitreous phases including borosilicate. From the previously reported researches, it can be expected that crystalline β-SiB_3 [12], and vitreous borosilicate layer [13-16] helps to decrease oxidation rate. The reduced oxidation data clearly indicates that the oxygen diffusion through the Si boride shell layer in the core-shell NPs is significantly slower than through the pure Si material.

2.3.1.4 Optical properties of SSC layers

High temperature applications of semiconductors are receiving more attention these days, for example, more efficient solar cells and thermoelectric devices using concentrated/focused sunlight with the naturally higher operating temperatures [17-19]. Therefore, high temperature oxidation resistant coating on a semiconductor surface is generally desirable. While the main focus of this research is on the improved oxidation resistance of Si based semiconductor nanomaterials at high temperatures for potential applications to a variety of devices, one example of such possible applications of the surface-protected Si nanoparticles is for efficient sunlight absorption in the concentrating solar power (CSP) power generating system. Therefore, the optical reflection measurement was made on SSC layers composed of Si - Si boride NPs coated on Inconel substrate and exposed to high temperatures, as compared to bare Si NPs processed in a similar manner.

The reflection measurement was made with the form of spectrally selective coating (SSC) layer composed of Si - Si boride NPs and another Si NPs casted on Inconel substrate as shown in Fig. 2-12 in order to compare the thermal stability of optical property based on the reflection measurement with annealing at high temperature in air atmosphere. As can be seen in Fig. 2-12, the prepared SSC layers with Si-Si boride NPs exhibits very little change in the surface color from the initial dark brown for as-prepared sample even after they were exposed to 850 ^{o}C annealing for 10 h in air. This implies that the Si - Si boride NPs can provide a strong resistance to thermal oxidation. On the contrary, SSC layers made of bare Si NPs have quite an obvious change of surface color from the intial light brown to orange color when exposed to 850 ^{o}C for 5 h, then to nearly white color after exposure to 850 ^{o}C for 10 h (Fig. 2-12). These changes to lighter colors are caused by easy oxidation of bare Si NPs at high temperature in air.

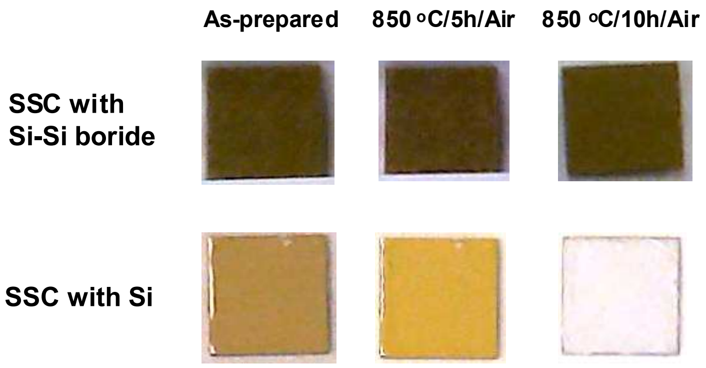

Figure 2-12. Surface color change of SSC layers after annealing at 850 ºC with the high temperature exposing time increasing up to 10 h under air atmosphere.

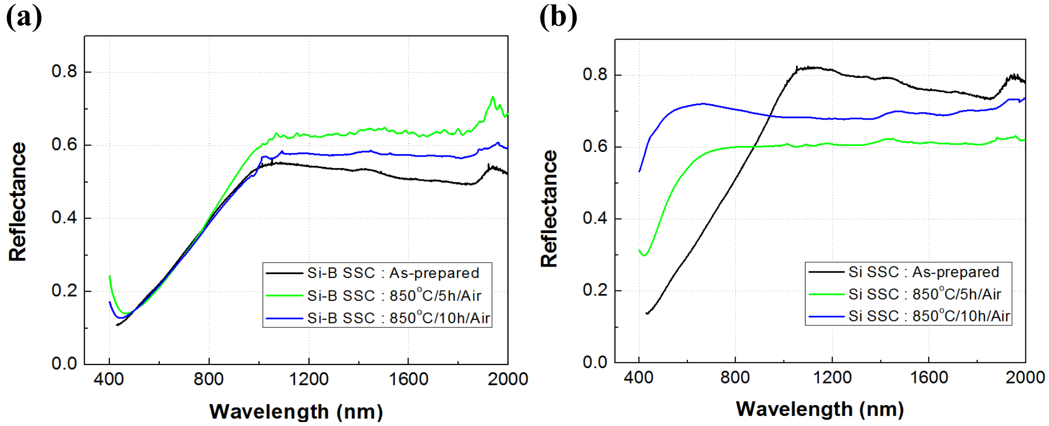

Figure 2-13. Reflectance measurements of high temperature exposed SSC layers made of (a) Si - Si boride NPs (Si-B), and (b) bare Si NPs.

Fig. 2-13 shows the comparison of the optical reflectance between the SSC layer of Si - Si boride NPs and that of Si NPs. As shown in Fig. 2-13(a), from long to short wavelengths, the reflectance starts decreasing abruptly at the wavelength of 1.05~1.08 µm, corresponding to bandgap of Si (1.13 µm or 1.12 eV) [20], and continues to reduce more gradually to 400 nm in the visible spectrum. If the transition point of reflectance is defined as the cut-off wavelength of reflection, it can be analyzed from Fig. 2-13(a) that the cut-off point of SSC layers with Si - Si boride NPs remains stable near the wavelength regime of 1.05~1.08 μm even though the reflectance in the near-IR regime was somewhat affected by the high temperature exposure, with the reflectance after 10 h exposure at 800 ^oC stabilizing toward the original value in the as-made samples (further research is required for understanding of specific effects of high temperature annealing parameters). Compared to the stable cut-off wavelength behavior of the SSC layer comprising the surface-protected Si NPs, the SSC layer with bare Si NPs exhibits a profound change upon 850 ^oC exposure, with the cut-off wavelength becoming significantly shorter from 1.05~1.08 μm in the near IR regime to 645 nm in the visible spectrum regime as shown in Fig. 2-13(b). After annealing at 850 ^oC, the reflectance of visible spectrum in SSC layers with Si - Si boride NPs are much more stable than that with bare Si NPs which experiences more increment of reflectance with annealing time increasing as shown in Fig. 2-13(b). This implies that most part of the bare Si NP was transformed into an insulating SiO_2 phase upon exposure to 850 ^oC for 10 h in air atmosphere in agreement with the color changes shown in Fig. 2-12.

While further R&D will be required to optimize the surface protection structures and their behavior, the sunlight receiver made of SSC layers with surface-protected Si - Si boride type NPs can be expected to enable a more stable/reliable electricity generation during high temperature operation in various solar thermal applications than with pure surface-unprotected semiconductor materials. Furthermore, the reflectance values in the visible spectrum representing a greater amount of sunlight energy is substantially lower in SSC layers with Si - Si boride NPS than that with bare Si NPs, which also allows much more efficient sunlight absorption so as to reach higher thermal efficiency.

2.3.2 Tandem-structured SSC layers with CuO NWs and Co_3O_4 NPs

2.3.2.1 Characterization of CuO NWs and Co_3O_4 NPs

The XRD analysis indicates that the scraped-off copper oxide nanowires (NWs) two crystal phases including CuO phase and Cu_2O phase (* mark) as shown in Fig. 2-15(a). For CuO crystal structure, two main planes of $(\bar{1}11)$ and (111) are observed at $2\theta = 35.6^{\circ}$ and 38.7°, respectively in end-centered monoclinic system [21]. For Cu_2O crystal structure there are three planes including (110), (111) and (200) at $2\theta = 29.5^{\circ}$, 36.3°, and 42.3°, respectively in primitive cubic system [22]. CuO phase can come from the crystal structure of nanowires and Cu_2O phase in XRD analysis can originate from the material in the copper oxide bottom layer from which the copper oxide NWs grow. Because the some chunks of bottom layer can be taken out together with nanowires during the strong scraping during the razor blade removal process.

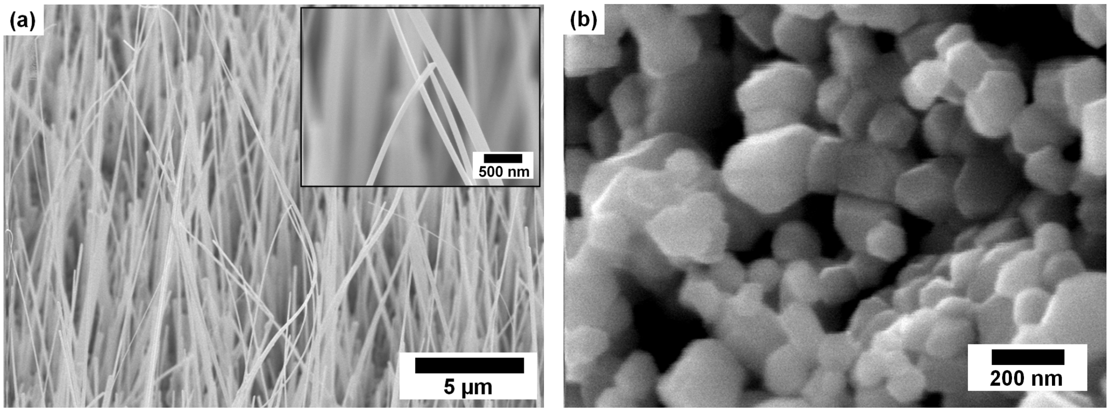

Figure 2-14. SEM images observed for (a) copper oxide NWs longer than 5 µm with a diameter of 100-200 nm, and (b) cobalt oxide NPs having mainly 100-200 nm in particle size.

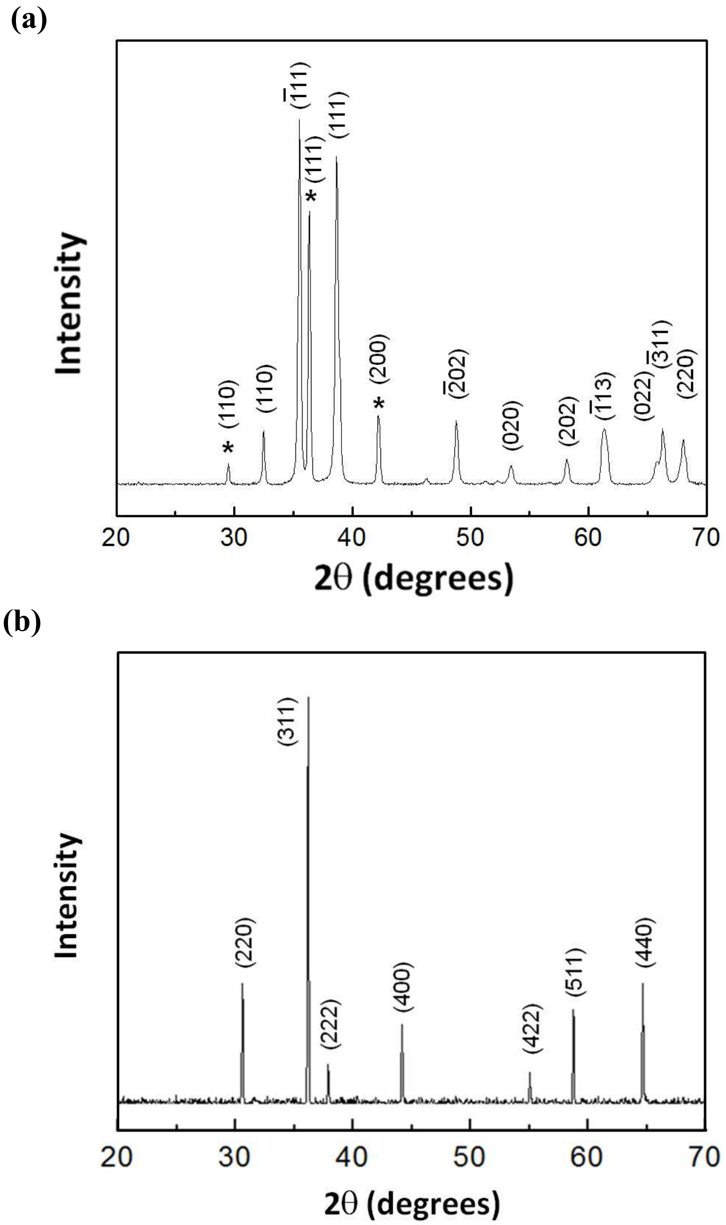

Figure 2-15. (a) XRD analysis of copper oxide nanowires (NWs) scraped off from the copper foil, showing two types of copper oxide NWs consisting of CuO and Cu_2O phase (* mark), and (b) XRD analysis of cobalt oxide nanoparticles (NPs) exhibiting the crystal structure of Co_3O_4.

In addition to the previous research on CuO NWs [23], our TEM and EDX analysis also confirm that the copper oxide nanowire is composed of only CuO crystal phase with band gap of 1.2-1.4 eV while the bottom layer copper oxide (from which the

CuO nanowires grow) contains CuO in the upper portion of the layer while some Cu_2O phase is present in the lower part of the bottom oxide layer. The Cu_2O phase is known to be a larger band gap copper oxide with 2.17 eV [24, 25]. The crystal structure of a single copper oxide nanowire is shown in the inset of the TEM image in Fig. 2-16(a). The FFT pattern in Fig. 2-16(b) obtained for all area of the nanowire in Fig. 2-16(a) shows that the copper oxide nanowire consists of only CuO phase containing (101), (110), (111), $(\bar{2}02)$, (202), (022) and $(\bar{2}04)$ plane which corresponds to lattice plane spacing of 3.138 Å, 2.739 Å, 2.356 Å, 1.885 Å, 1.570 Å, 1.425 Å and 1.195 Å, respectively. The cross-sectional SEM image of CuO NW layer obtained by tilting 90° was analyzed by EDX analysis at three points (a: nanowire at 2 μm above the nanowire bottom surface, b: 1.5 μm underneath the nanowire bottom surface (within the bottom copper oxide layer), and c: 8 μm underneath the nanowire bottom surface) as exhibited in Fig. 2-17. This EDX analysis at point **a** on nanowires indicates that the composition of overall nanowires is ~ 1/1 (Cu/O) in atomic ratio which is in accordance with CuO phase as identified by TEM and FFT in Fig. 2-16. The first point beneath nanowire's bottom surface (point **b**) is confirmed to be composed of ~1/1 (Cu/O) in atomic ratio corresponding to CuO phase, while the second point beneath the nanowire bottom surface (point **c**) shows ~2/1 (Cu/O) in atomic ratio matching with Cu_2O phase.

The nanowire layer (above 5 μm thickness) is all made of CuO phase as identified by TEM. The upper portion of the oxide layer (from which the CuO nanowires grow) is ~5 um thick and also CuO phase as identified by EDX analysis. The lower portion of the bottom oxide layer contains some Cu_2O. Therefore, the optical reflectance behavior is mostly dominated by the CuO phase which is located at outermost two layers having total thickness of above 10 μm. During CSP operation at high temperature, it is likely that the Cu_2O phase will eventually oxidize further to become CuO, which is considered to be a beneficial reaction.

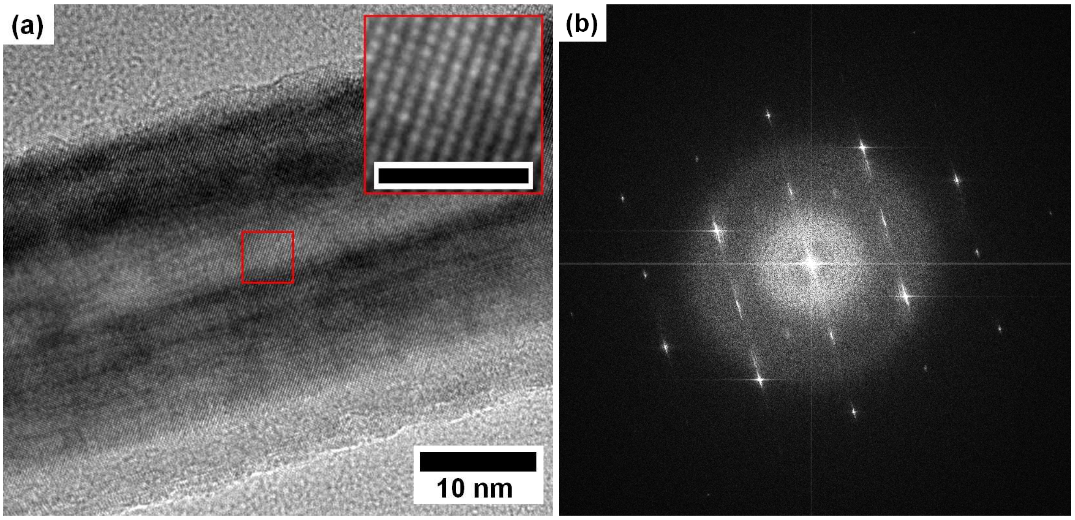

Figure 2-16. (a) Images of a single CuO nanowire by TEM analysis where an inset image is a magnified crystal structure of CuO for a red-lined square area (a black scale bar = 2 nm), and (b) FFT patterns obtained from all area of the nanowire in Fig. 2-16(a).

For study of the stability of CuO phase at high temperature, the copper oxide nanowire layer was annealed at 500 °C for 10 h under air atmosphere and the overall atomic composition of Cu/O was measured with EDX as shown in Fig. 2-18. The atomic composition of CuO in nanowires and in the upper portion of the oxide bottom layer are stable enough to maintain ~1/1 ratio of Cu/O, which implies that the formed CuO phase can be expected to retain the stable crystal structure and optical properties during CSP operation.

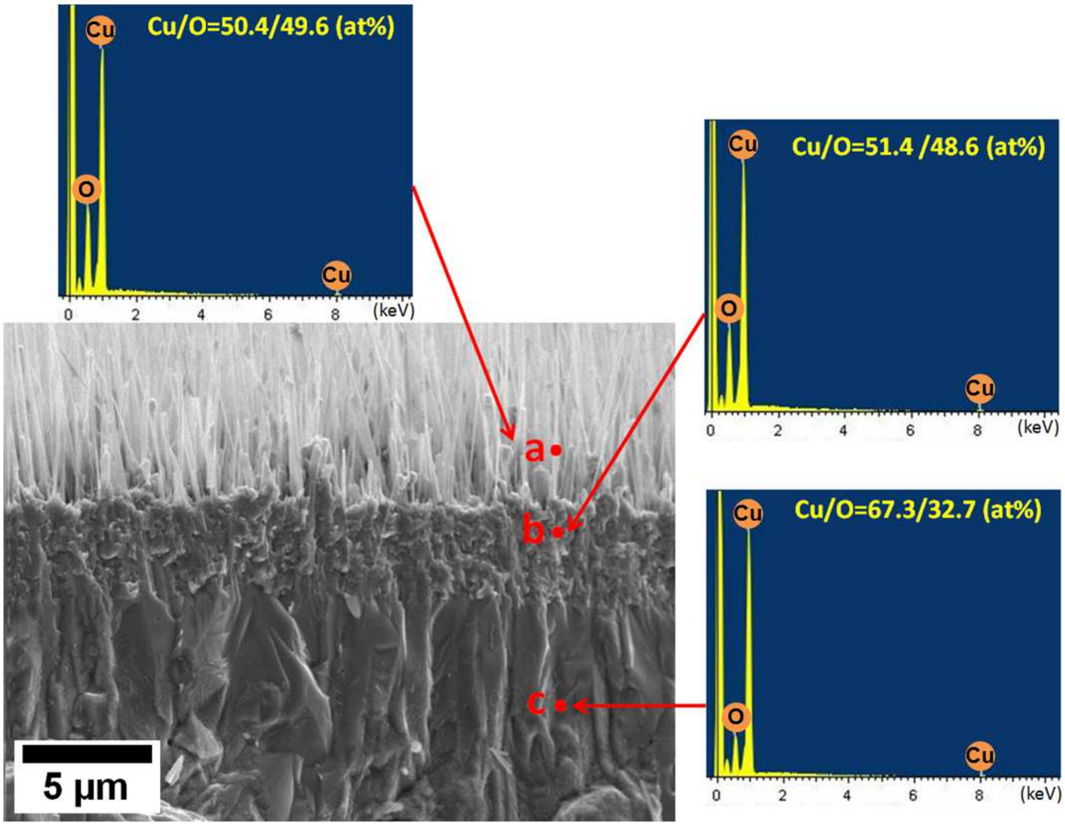

Figure 2-17. EDX analysis made with observation of a cross-sectional SEM image (tilt angle: 90 °) of as-prepared copper oxide NWs layer showing two phases (CuO, and Cu_2O) depending on the position (a: nanowire at 2 µm above nanowire bottom surface, b: 1.5 µm underneath the nanowire bottom surface, and c: 8 µm underneath the nanowire bottom surface). The small peaks at 0.2-0.4 keV come from the carbon tape used for sample holding.

Fig. 2-15(b) shows XRD analysis of cobalt oxide nanoparticles (NPs) annealed at 750 °C for 2 h in air. This analysis confirms that the hydrothermally synthesized cobalt oxide NPs are Co_3O_4 phase which has a main plane of (311) at $2\theta = 36.2^{o}$ in face-centered cubic system [26].

The SEM image in Fig. 2-14(a) shows that the copper oxide NWs are longer than 5 µm in length and have 100-200 nm in diameter as can be seen more clearly in an inset image in Fig. 2-14(a). The spacing between adjacent nanowires appears to be roughly

500 nm to 2 um. The aspect ratio of nanowires is higher than ~25, which is believed to be beneficial for higher absorption efficiency due to light trapping effect [27-30]. The SEM image in Fig. 2-14(b) exhibits that cobalt oxide NPs annealed at 750 °C for 2 h have mainly 100-200 nm in particle size, although some particles have a diameter as small as 50 nm.

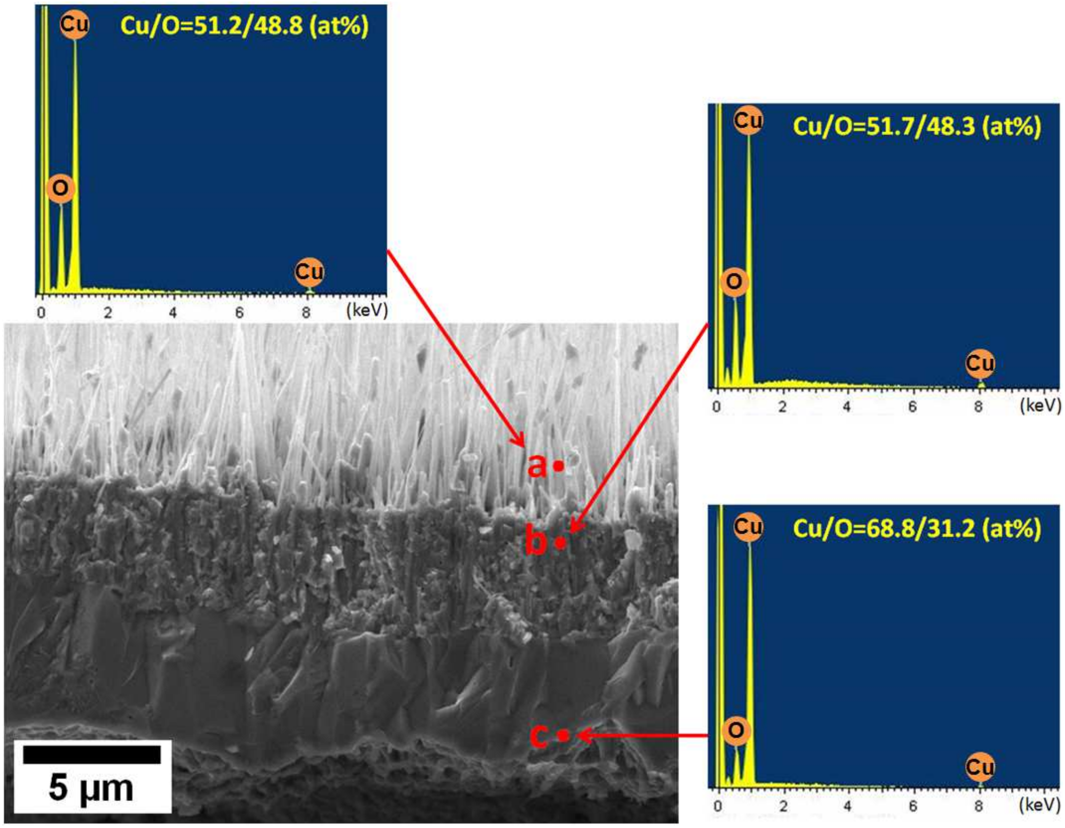

Figure 2-18. EDX analysis is made with observation of a cross-sectional SEM image (tilting angle: 90 °) for annealed copper oxide NWs layer at 500 °C for 10 h under air atmosphere at similar position to the as-prepared sample (a: nanowire at 2 µm from bottom surface, b: 1.5 µm underneath bottom surface, and c: 8 µm underneath bottom surface). The small peaks at 0.2-0.4 keV come from a carbon tape for sampling.

2.3.2.2 Tandem-structured SSC layer by spray-coating

Tandem structure of solar absorbers can be fabricated with copper oxide nanowires (NWs) coated with the solution of cobalt oxide nanoparticles (NPs) by means of either spray-coating or dip-coating with the aforementioned concept explained in the left side procedure of Fig. 2-3.

Spray-coating of cobalt oxide NPs solution is made onto copper oxide NW layer of Fig. 2-14(a). Due to the vertically aligned nanowire structure of copper oxide, the cobalt oxide solution, even with nanoparticle size, is difficult to uniformly penetrate all the way down to the bottom of nanowires through their interspace gap regions. Therefore, a micro-ball type of cobalt oxide structure with a partial penetration into copper oxide NWs is formed when spray-coating is carried out, as shown in Fig. 2-19(b).

Even though the cobalt oxide NPs are not infiltrated into the bottom of the CuO nanowire array, the optical reflectance data in Fig. 2-19(a) shows that this type of tandem structure decreases near-IR reflectance due to the absorption of near-IR by Co_3O_4 NPs. The reflectance of visible light spectrum increases slightly compared to the copper oxide NWs only structure due to the addition of someCo_3O_4 NPs. Figure of merit (FOM) value increases a little from 0.864 to 0.875 when the copper oxide NWs is hybridized into a tandem structure with the addition of cobalt oxide NPs by spray-coating because the overall absorbed solar energy is larger in cobalt oxide NPs-sprayed copper oxide NWs due to the more substantial reduction of reflectance in the near-IR spectrum range relatively to the increment of the reflectance in the visible spectrum range.

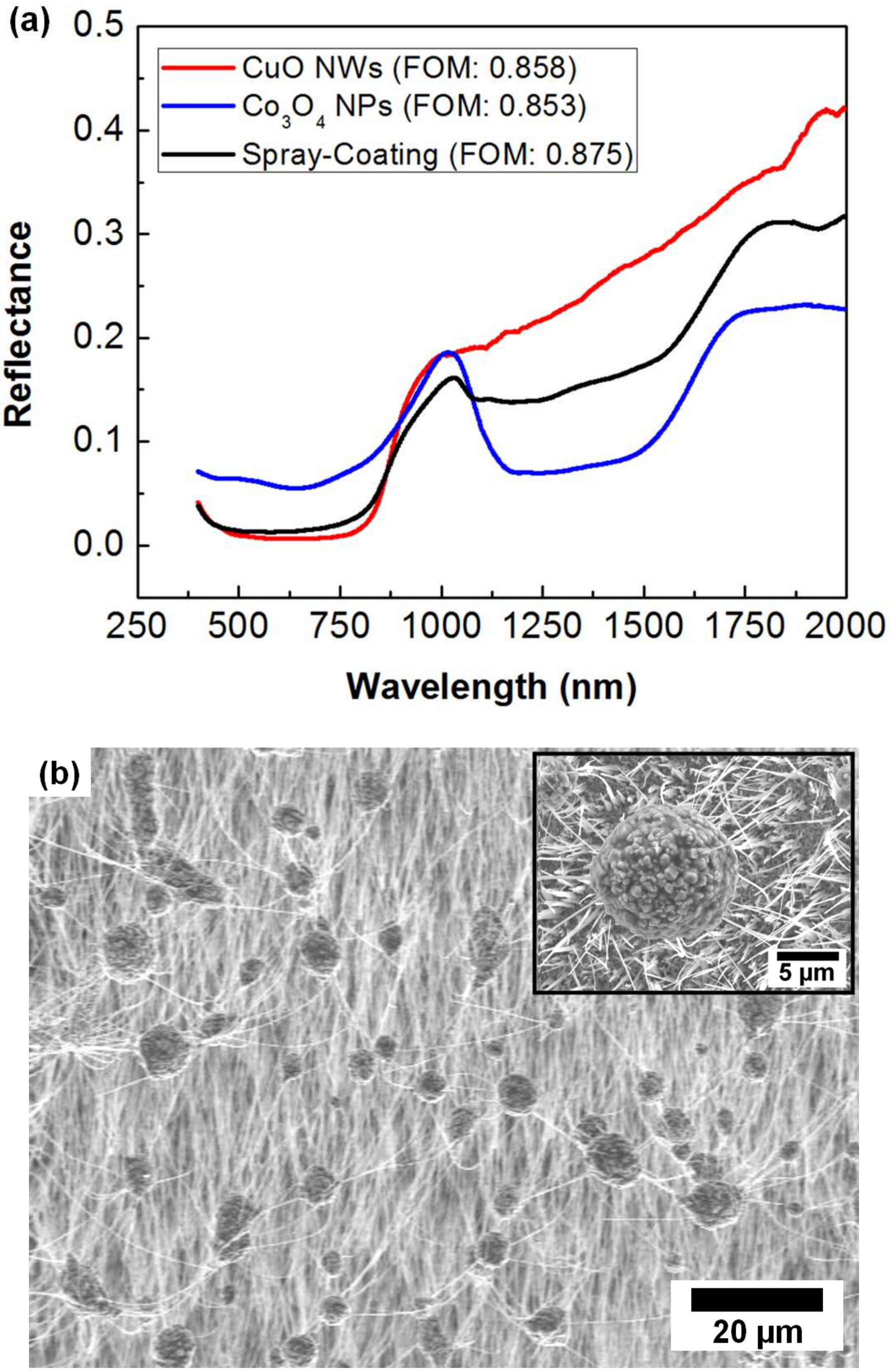

Figure 2-19. (a) Comparison of the optical reflectance and FOM between the tandem SSC layer by spray-coating, and the SSC layer of copper oxide NWs only, or the SSC layer of cobalt oxide NPs only, and (b) SEM image of tandem SSC layer made by spray-coating of cobalt oxide NPs onto vertical copper oxide NWs.

2.3.2.3 Tandem-structured SSC layer by dip-coating

Comparison of optical reflectance and FOM among different SSC layers, shown in Fig. 2-20(a), indicates that the optical reflectance properties are sensitive to the SSC layer structures and how they are produced. As compared to the rapid spray-coated structures, a slower process of dip-coating allows the cobalt oxide nanoparticles (NPs) to penetrate deeper into the spaces between copper oxide nanowires (NWs) having a relatively small spacing of ~500 nm to 2 um between adjacent nanowires. In addition, cobalt oxide NPs can also be entangled with copper oxide NWs, which may enable the formation of multi-scaled structures composed of the combination of microscale and nanoscale structures of nanowires and nanoparticles, as observed in Fig. 2-20(c-1)-(d-2). The presence of some pore structures may also contribute to enhanced sunlight absorption. In order to make cobalt oxide NPs to infiltrate into copper oxide NW structures more efficiently, a cycle of vacuum suction/venting process is devised for the dip-coating process. The vacuum is not a high vacuum but a typical, mechanical pump type of low vacuum was sufficient. The vacuum process extracts and removes most of entrapped air from copper oxide NWs structure, and this process causes the cobalt oxide NPs in solution to be sucked into the spaces that the air pocket previously occupied. Subsequent venting step allows the air to come in which generates such a large pressure difference between vacuum state and atmospheric pressure that cobalt oxide NP solution is pushed and driven into the interspace of aligned copper oxide NWs. Repeated vacuum/vent processes further improves the formation of tandem mixed structure and the sunlight absorption and the FOM properties are accordingly also improved as will be discussed later.

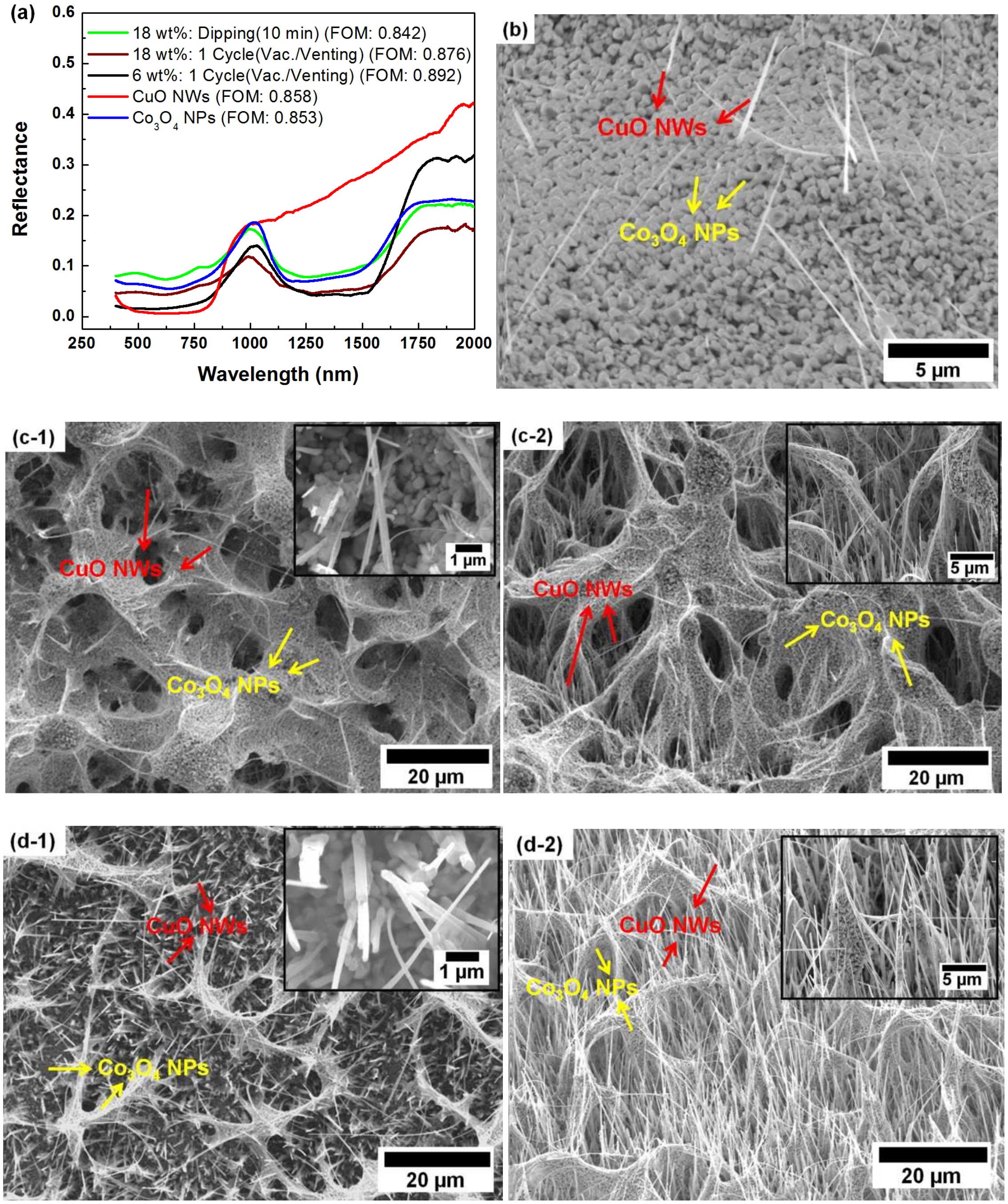

Figure 2-20. (a) Comparison of optical reflectance and FOM among different SSC layers, (b) a top view surface image of tandem SSC layer made by 10 min dip-coating in 18 wt% cobalt oxide solution without using a vacuum process, (c-1) a top view surface image and (c-2) a tilted surface image of tandem SSC layer made by dip-coating with 1 cycle of vac./venting in 18 wt% cobalt oxide solution, and (d-1) a top view surface image and (d-2) a tilted surface image of tandem SSC layer made by dip-coating with 1 cycle of vac./venting in 6 wt% cobalt oxide solution.

It is seen that without using the vacuum/venting process, the cobalt oxide NPs hardly get into the inter-nanowire spacing, as can be seen in Fig. 2-20(b) but instead cover up the surface of the CuO nanowire structure as an almost continuous particle layer. Copper oxide NWs are rarely seen to protrude out of the cobalt oxide NP layer, except a few NWs which has very little affect on optical properties of SSC layers. As expected, the optical reflectance data of this monotonous structure shows a similar reflectance behavior to that of the SSC layer fabricated with cobalt oxide NPs only (Fig. 2-20(a)) and the FOM value of this structure is only 0.842 which is not high enough to absorb sufficient solar energy. This dip-coated sample without using vac./venting procedure produces a structure covered mostly with Co_3O_4 particles, with very few number of CuO nanowires protruding (Fig. 2-20(b)), so it is essentially Co_3O_4 particle surface. The spray-coating method to produce the Co_3O_4 particle SSC layer tends to have a high porosity and roughness as represented in Fig. 2-21. Therefore, the Co_3O_4 layer of Fig. 2-21 produces a slightly lower reflectance in the visible spectrum range.

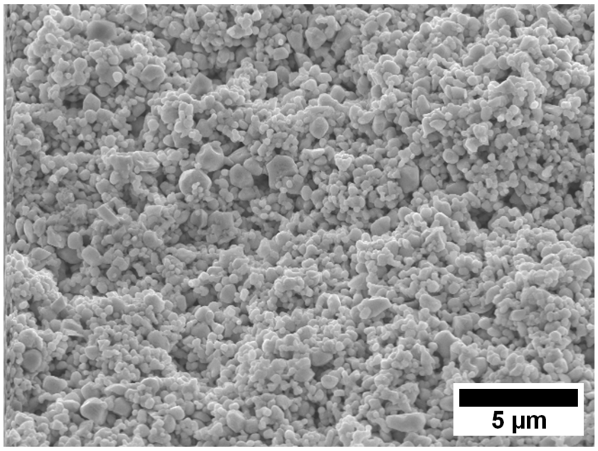

Figure 2-21. SEM image of the surface in SSC layer which was made of only Co_3O_4 NPs and with the spray-coating method.

The vacuum/venting process was utilized to make further advanced dip-coating structures with the concentrated solution of 18 wt%. After placing the copper oxide NW sample into cobalt oxide NP solution, the vacuum is made for 20 sec followed by a fast venting process with air, which may cause some interesting mechanical disturbance on the coating structure. As shown in Fig. 2-20(c-1) and (c-2), copper oxide NWs and cobalt oxide NPs form combined complex structures where copper oxide NWs are entangled with themselves coated with cobalt oxide NPs. In more details, a top side of this sample displays a spire-like roof layer of cobalt oxide NPs in Fig. 2-20(c-1) whose inset image shows the bottom surface coated with cobalt oxide NPs at interspaces between the copper oxide NWs. The tilted images including a magnified inset image in Fig. 2-20(c-2) exhibit the entangled tripod-like structure of copper oxide NWs mixed with cobalt oxide NPs. Fig. 2-20(a) demonstrates that this 3-dimensionally entangled tripod-like structure can decrease the reflectance in both visible and near-IR spectrum regime and obtain a higher FOM value of 0.876, compared to the sample made by a continuous dipping (Fig. 2-20(b)).

To better control the degree of entangling of copper oxide NWs and agglomeration of cobalt oxide NPs, the dip-coating solution was diluted to 6 wt%, that is, 1/3 of initial concentration, as the third approach. This third dip-coating method also uses the procedure of vacuum/venting, but due to the reduced solid concentration of nanoparticles and the binder resin, the insertion of the nanoparticles into the nanowire spacing gets easier. From the top view surface image (Fig. 2-20(d-1)) and a tilted view (Fig. 2-20(d-2)), the occupied area by a spire-like top layer of cobalt oxide NPs is diminished (Fig. 2-20(d-1)) and micro-cone structure of cobalt oxide NPs is formed (see the inset of Fig. 2-20(d-2)) instead of the tripod-like structure observed in Fig. 2-20(c-2). The dip-coating with a diluted solution of 6 wt% essentially maintains the nanowire structure of copper oxide after the dip-coating of cobalt oxide NPs so that a more or less uniform multi-scaled micro-nano structure can be made, which can be more effective in absorbing sunlight in both visible spectrum and near-IR spectrum.

Optical reflectance measurements in Fig. 2-20(a) shows that this multi-scaled tandem structure (Fig. 2-20(d-1) and (d-2)) coated with the diluted solution of 6 wt% exhibits much lower reflectance in visible spectrum and similarly reduced reflectance in near-IR spectrum range, compared to the entangled tripod-like structure (Fig. 2-20(c-1) and (c-2)) made of cobalt oxide solution with higher concentration of 18 wt%. The FOM value of this structure increases up to 0.892 which is much higher than the structure of Fig. 2-20(c-1) and (c-2). The lower reflectance in visible spectrum results from the well-preserved nanowire structure of copper oxide and the similarly low reflectance of near-IR (1.0-1.55 μm) is attributed to the cone-type of microstructure of cobalt oxide NPs as well as the layer of cobalt oxide NPs coated on the bottom of copper oxide NWs as can be seen in the inset of Fig. 2-20(d-1). In the spectrum ranging from 1.55 μm to 2.0 μm, the dip-coated layer with 6 wt% solution shows a steeper increase of reflectance than that with 18 wt% solution. The diluted 6 wt% Co_3O_4 particles layer has less amount of Co_3O_4 than the 18 wt% Co_3O_4 layer. It can be recognized that Co_3O_4 particles layer reflects less IR spectrum ranging from 1.0 μm to 2.0 μm than CuO nanowires layer as can be compared in Fig. 2-20(a). Lower concentration of Co_3O_4 particles can make thinner layer of Co_3O_4 particles and will result in less absorption which enable the SSC layer to have higher reflectance in IR spectrum compared to SSC layer coated with an 18 wt% solution (brown-colored graph in Fig. 2-20(a)). This behavior of reflectance increasing steeply from 1.55 μm will be useful for the CSP or other solar thermal application which needs to have cut-off wavelength around 1.55 μm in order to reduce the emission loss of infrared spectrum. For instance, in the parabolic trough type concentrated solar power systems, the cut-off wavelength of 1.5 um is helpful to increase FOM value by diminishing the amount of IR emission at 700 °C [1].

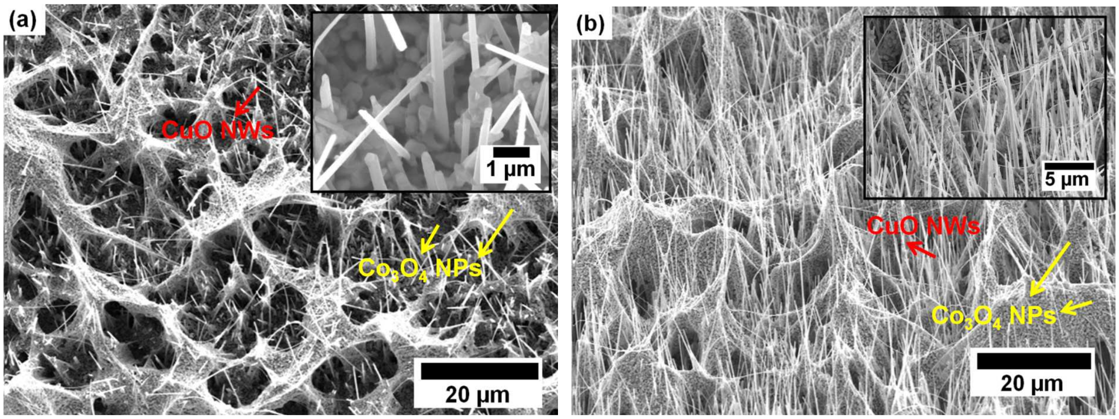

Figure 2-22. SEM images showing (a) a top view surface image and (b) a tilted surface of tandem SSC layer made by dip-coating with 3 cycles of vac./venting procedures in 6 wt% cobalt oxide solution.

To optimize the procedure of vacuum/venting cycle, the dip-coating is also made with 3 cycles of vacuum/venting by which more cobalt oxide NP material is pushed into the CuO NW structure so that an increased amount of cobalt oxide layer is expected to be deposited onto the bottom of CuO NW structure. The inset image of Fig. 2-22(a) shows that the bottom of copper oxide NWs is covered with cobalt oxide NPs. Repeated vacuum/vent processes further improves the formation of tandem mixed structure with more cobalt oxide NPs deposited, with the sunlight absorption and the FOM properties accordingly improved. For example, 3 cycles of vacuum/venting process for dip-coating with the diluted solution of 6 wt% forms a somewhat larger area of a spire-like roof layer of cobalt oxide NPs (Fig. 2-22(a)), compared to the structure made with just 1 cycle of vacuum/venting procedure (Fig. 2-20(d-1)). From tilted images in Fig. 2-22(b), it can be observed that cobalt oxide NPs form micro-cone structure similar to the structure in the inset image of Fig. 2-20(d-2).

Optical reflectance measurement in Fig. 2-23 indicates that the 3 cycle procedure slightly increases the reflectance of visible spectrum but noticeably decreases the reflectance of near-IR as well as short wavelength IR spectrum. The small increase of reflectance in the visible spectrum results from the diminished nanowire structure of copper oxide caused by the addition of more nanoparticles and wider spire-like roof area of cobalt oxide NPs. The thicker cobalt oxide layer which can be expected by 3 repetition cycles absorbs a larger amount of sunlight near-IR spectrum (1.6-2.0 μm) to result in the decreased reflectance in that wavelength regime. In the near-IR spectrum range, shorter near-IR (0.8-1.6 μm) is more important to a solar absorber due to its higher energy than longer near-IR (above 1.6 μm). The SSC layer made by 3 cycles of vacuum/vent processing has FOM value of 0.891 which is very similar to that (0.892) of SSC layer by 1 cycle dip-coating.

For a contrast experiment, a SSC layer was fabricated using the mixture solution (1/1 w/w) of Co_3O_4 particles and CuO nanowires which were scraped off from the copper foil. Using the same condition and ball-mixing procedure as the previous Co_3O_4 layer, the mixture solution was spray-coated on Inconel substrate and the reflectance of the sample was measured. Fig. 2-24 indicates that the reflectance of the mixture sample is much higher in all spectrum range than the dip-coated SSC layer made with 6 wt% and vac./venting procedure. One possible reason for such a behavior is that the nanowires can be inadvertently shortened much during the ball-mixing process, thus the SSC layer has no structure advantage on entrapping sunlight, compared to SSC layer of vertically standing nanowires.

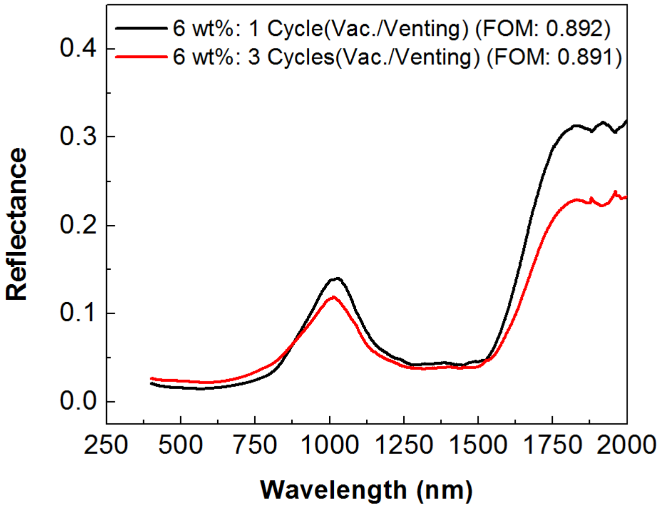

Figure 2-23. Reflectance and FOM values for tandem SSC layers fabricated by dip-coating with 1 cycle and 3 cycles of vac./venting process in 6 wt% cobalt oxide solution.

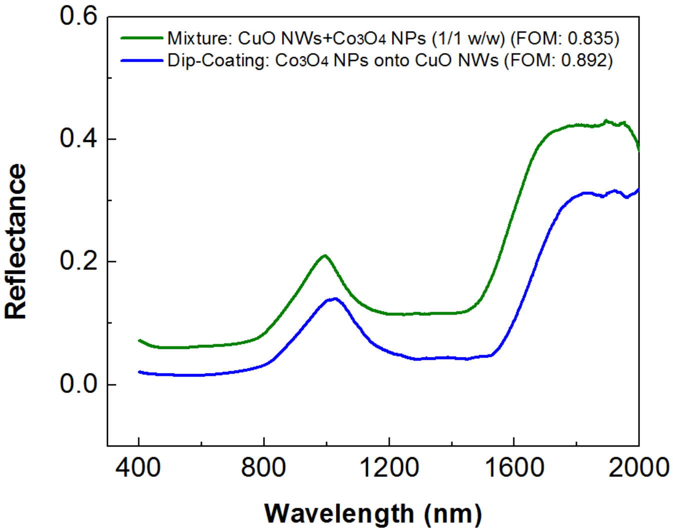

Figure 2-24. Reflectance and FOM values for SSC layer made of a mixture of Co_3O_4 NPs and CuO NWs (1/1 w/w) with spray-coating method.

2.3.2.4 Tandem-structured SSC layer by transferring of CuO NWs layer

Copper oxide nanowire (NW) layer separated from Cu foil is composed of a horizontally configured copper oxide flat layer (1-2 μm thick) at the bottom from which copper oxide NWs have grown, as indicated in Fig. 2-25(a). Fig. 2-25(b) represents the final attached structure consisting of copper oxide NWs layer / polysiloxane binder resin layer / cobalt oxide NPs layer. It is expected that pure copper oxide NWs layer without cobalt oxide NPs is able to absorb more visible spectrum while the cobalt oxide NPs layer under copper oxide NW layer can absorb the near-IR spectrum transmitted through the copper oxide NW layer positioned above the nanoparticle layer, as explained in the aforementioned concept section (Fig. 2-3).

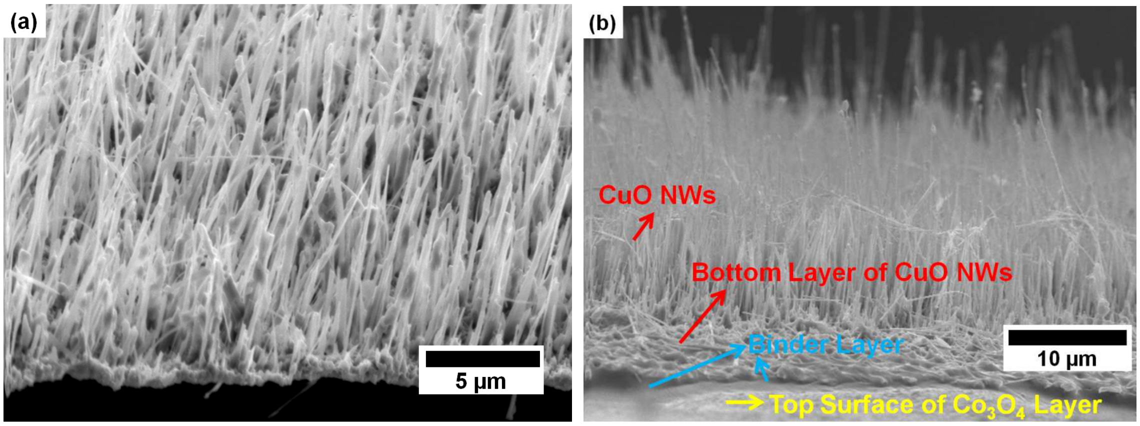

Figure 2-25. SEM images representing (a) a stand-alone copper oxide NWs layer obtained by etching Cu metal layer, and (b) a transferred copper oxide NWs layer attached onto cobalt oxide layer with a thin binder resin layer.

The reflectance of visible spectrum is similarly as low as the pure copper oxide NW sample, but the reflectance of near-IR spectrum is not decreased as low as pure cobalt oxide layers, as shown in Fig. 2-26. The data in Fig. 2-26 indicates that the reflectance value in the shorter near-IR spectrum for the SSC layer fabricated by transferring the CuO NW layer is higher than that for the SSC layer of pure cobalt oxide NPs and lower than that for the SSC layer of pure copper oxide NWs, as well as SSC layer made by the spray-coating. Copper oxide NWs may reflect near-IR spectrum partially before it is transmitted to the bottom layer of Co_3O_4 NPs. Table 2-2 shows FOM values of the representative SSC layers including SSC layer fabricated by the transfer method. The tandem SSC layer by transferring has FOM value of 0.886 which is much higher than that of pure copper oxide NWs, pure cobalt oxide NPs and spray-coated SSC layers, but lower than that of efficiently dip-coated SSC layer.

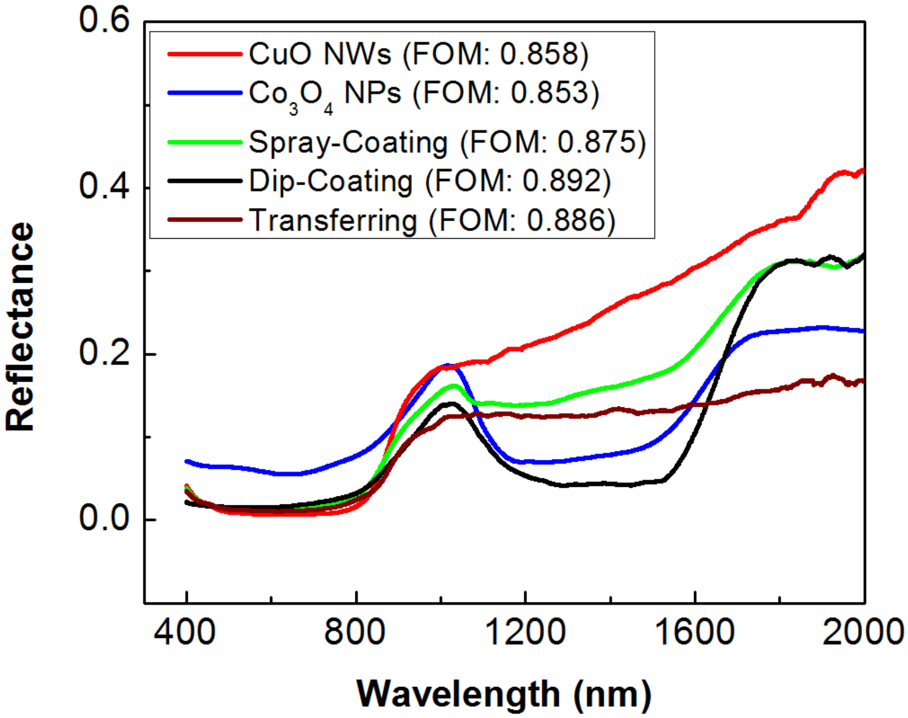

Figure 2-26. Optical reflectance and FOM compared among structured SSC layers including a copper oxide NWs layer only, a cobalt oxide NPs layer only, a spray-coated tandem SSC layer, a dip-coated tandem SSC with 1 cycle of vac./venting process in 6 wt% cobalt solution, and a transferred tandem SSC layer.

Table 2-2. Calculated FOM values from reflectance measurement of SSC layers.

SSC Layers	FOM
Copper Oxide NWs only	0.858
Co_3O_4 NPs only	0.853
Tandem SSC by Spray-Coating	0.875
Tandem SSC by Dip-Coating (1 cycle, 6 wt%)	0.892
Tandem SSC by Transferring	0.886

2.3.3 Tandem-structured SSC layers with $CuFeMnO_4$ and $CuCr_2O_4$

2.3.3.1 Characterization of spinel Cu-contained nanoparticles

Two types of Cu-contained black oxide nanoparticles were fabricated and their crystal structures can be analyzed with XRD as shown in Fig. 2-27. As-prepared $CuCr_2O_4$ particles have a main plane (211) at $2\theta = 35.19\ ^{o}$ and have a tetragonal crystal system with body-centered lattice [31]. After thermal cycling (RT-750 ^{o}C / 100 cycles) and isothermal annealing (750 ^{o}C / 500 h) in air, the particles can retain the original $CuCr_2O_4$ crystal structure and their particle size just grows by sintering effect at high temperature, as can be found in Fig. 2-27(a). Based on this XRD analysis, $CuCr_2O_4$ nanoparticles are thermally stable at 750 ^{o}C in air environment because there is no new phase appearing after those thermal tests. And also the crystal structure of as-prepared Cu-Fe-Mn oxide nanoparticles can be confirmed to be $CuFeMnO_4$ crystal structure by XRD analysis [32], as exhibited in Fig. 2-27(b). These $CuFeMnO_4$ nanoparticles prove to be stable at 750 ^{o}C in air atmosphere because new phase does not emerge in XRD analysis after thermal tests including a thermal cycling test and an isothermal annealing test. It can be just found that the particle size increases after thermal tests, which is the similar phenomenon to $CuCr_2O_4$ resulting from sintering effect.

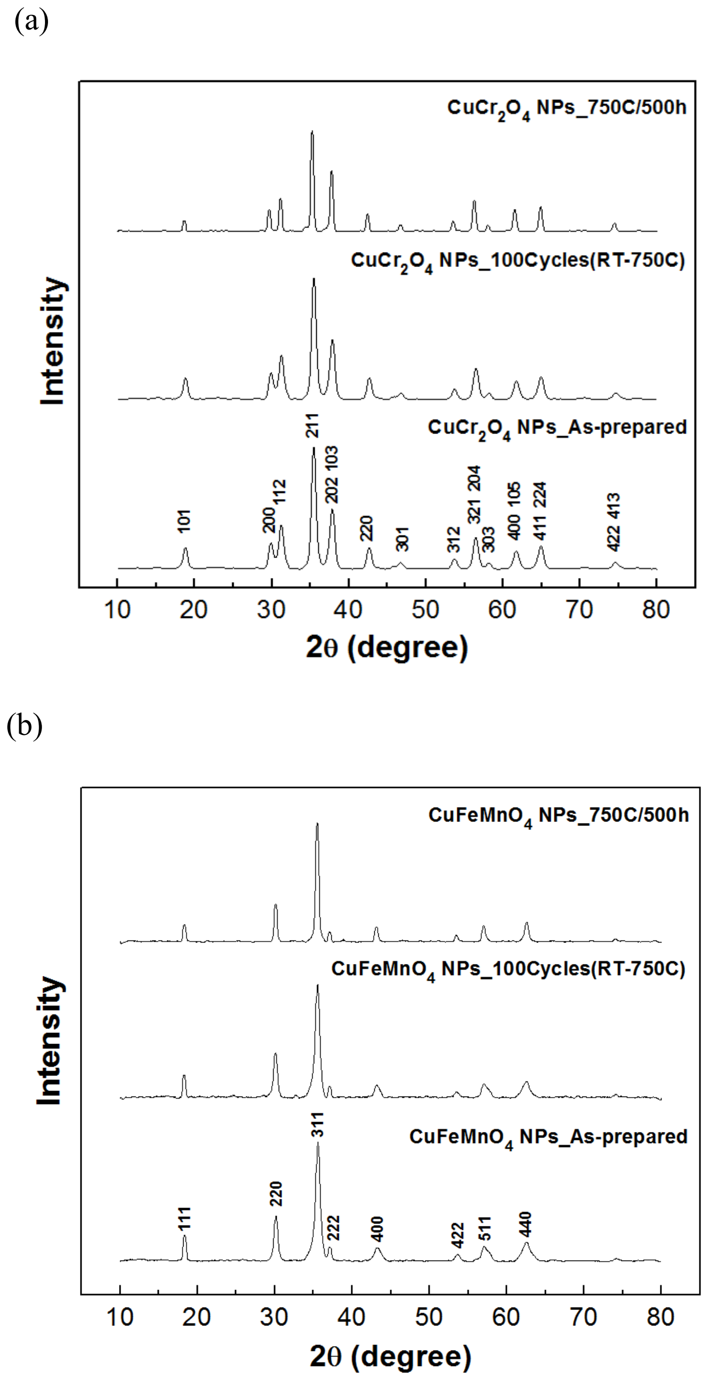

Figure 2-27. XRD analysis for (a) synthesized $CuCr_2O_4$ nanoparticles and (b) $CuFeMnO_4$ nanoparticles in as-prepared state, after thermal cycling (RT-750 °C / 100 cycles) in air, and after isothermal annealing at 750°C for 500h under air environment.

2.3.3.2 Optimization of atomic composition and crystallization temperature

One copper chromite nanoparticles were synthesized hydrothermlally with atomic ratio of 1/1 (Cu/Cr) and another copper chromite was synthesized with atomic ratio of 1/2 (Cu/Cr). And they were crystallized as a final step of synthesis at different temperature conditions; 550 °C for 5 h in air, and 750 °C for 2 h in air. Fig. 2-28 shows SEM images of those various copper chromites fabricated with two different atomic ratios and two different crystallization temperatures.

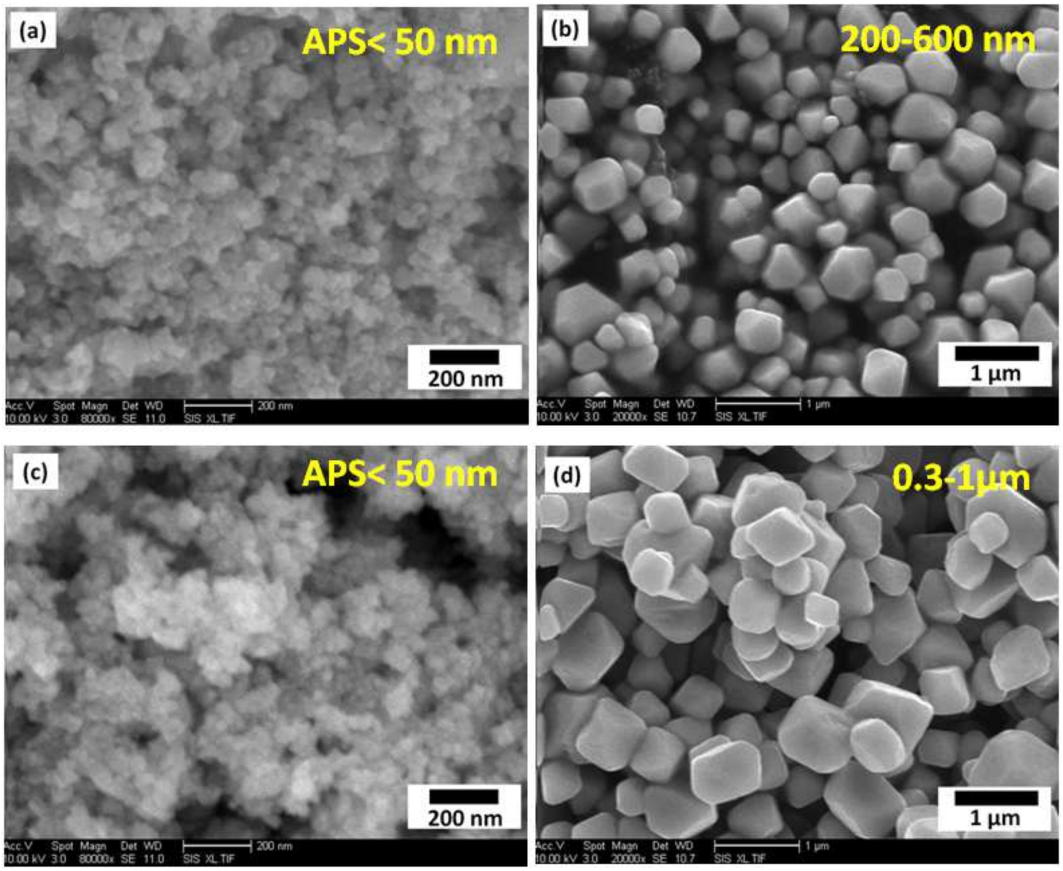

Figure 2-28. SEM images of copper chromite nanoparticles synthesized with different conditions: (a) atomic ratio of Cu/Cr = 1/1 and crystallized at 550°C/5h/air, (b) atomic ratio of Cu/Cr = 1/1 and crystallized at 750°C/2h/air, (c) atomic ratio of Cu/Cr = 1/2 and crystallized at 550°C/5h/air, and (d) atomic ratio of Cu/Cr = 1/2 and crystallized at 750°C/2h/air.

Copper chromites crystallized at 550 °C for 5 h in air show the particle size smaller than 50 nm irrelevantly to the atomic ratios of Cu and Cr as displayed in Fig. 2-28 (a) (Cu/Cr = 1/1) and (c) (Cu/Cr = 1/2). When crystallized at 750 °C for 2 h in air, one copper chromite (Cu/Cr = 1/1) increases particle size to be 200-600 nm as shown in Fig. 2-28 (b) and another copper chromite (Cu/Cr = 1/2) grows to be 300 nm – 1 μm in size as can be seen in Fig. 2-28 (d).

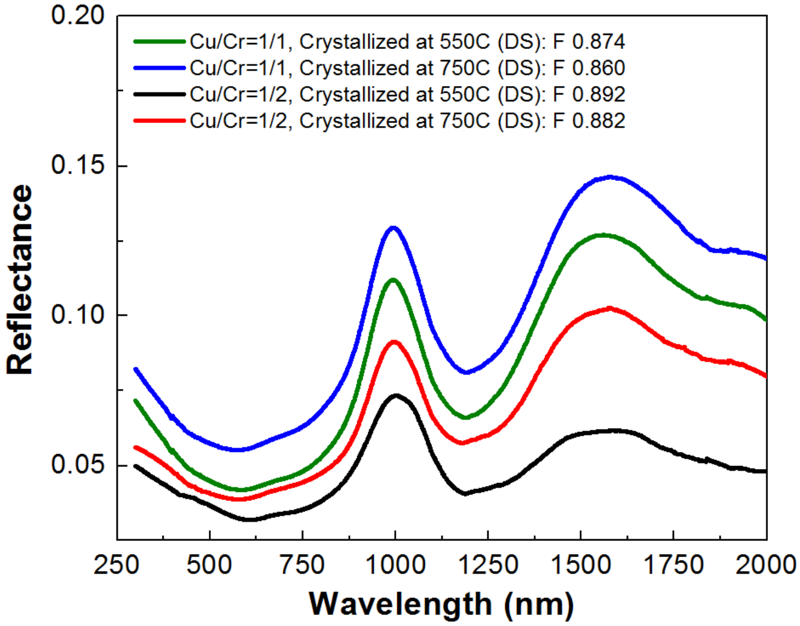

Figure 2-29. Relfectance measurements of copper chromite SSC layers having a dense single layer on Inconel substrate and fabricated with copper chromited nanoparticles synthesized with different conditions. (DS: a dense single layer, F: Figure of Merit)

Fig. 2-29 explains the reflectance behaviors and FOM values of spectrally selective coating (SSC) layers fabricated with aforementioned 4 different copper chromites particles using the preparation method of a dense layer introduced in the experimental section. Based on results of reflectance measurement, it can be known that the SSC layer of copper chromite particles with more Cr amount and crystallized at lower temperature shows the lowest reflectance and highest FOM value (0.892). Therefore, it can be decided that the optimized copper chromite is $CuCr_2O_4$ crystallized at 550 ^oC, considering both the reflectance measurement result and XRD analysis.

$CuFeMnO_4$ nanoparticles crystallized at 550 ^oC for 5 h in air have particle size of 100-200 nm which is smaller than $CuFeMnO_4$ particles crystallized at 750 ^oC for 2 h in air, as recognized in Fig. 2-30. Based on particle size, the crystallization condition can be chosen to be 550 ^oC / 5 h / air for the fabrication of $CuFeMnO_4$ nanoparticles, because SSC layers made of smaller nanoparticles expect to show lower reflectance than that of larger particles with same atomic composition just like the result in Fig. 2-29.

Fig. 2-31 exhibits reflectance measurement results and FOM values of dense SSC layers made of Cu-Fe-Mn oxide nanoparticles having 5 different atomic compositions of Cu/Fe/Mn. Copper iron manganese oxide particle optimized for the SSC layer of a solar receiver can be selected to be $CuFeMnO_4$ nanoparticles (Cu/Fe/Mn = 1/1/1) crystallized at 550 ^oC for 5 h under air atmosphere because its reflectance is lower than other samples and achieves the highest FOM (0.881) as indicated in Fig. 2-31. From this experiment, some useful results are induced in regard to optical properties change of SSC layers with atomic compositions. A SSC layer of Cu-Fe-Mn oxide with a larger amount of Fe (Cu/Fe/Mn = 0.5/2.0/0.5) shows very high reflectance in near-IR spectrum longer than 750 nm, which brings low FOM (0.855). Although it has high spectrally selectivity at ~ 750 nm between visible spectrum and near-IR spectrum, the cut-off wavelength is recommended to shift from 750 nm to 1.5-2.5μm [1] in order to increase the conversion efficiency of solar to thermal energy (FOM) of solar receivers. On the other hand, a SSC layer with a smaller amount of Fe (Cu/Fe/Mn = 1.125/0.75/1.125) shows low reflectance in near-IR spectrum having FOM (0.871). A SSC layer with a large amount of Cu (Cu/Fe/Mn = 2.0/0.5/0.5) shows high reflectance in both visible and near-IR spectrum which makes low FOM (0.865). And a SSC layer with a large amount of Mn (Cu/Fe/Mn = 0.5/0.5/2.0) does not increase reflectance much compared to the SSC layer with the composition of 1/1/1 (Cu/Fe/Mn).

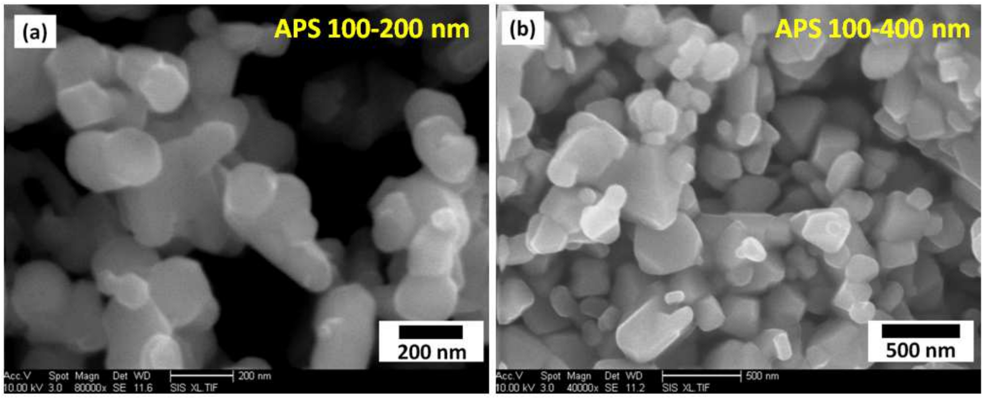

Figure 2-30. SEM images of $CuFeMnO_4$ nanoparticles crystallized at (a) 550ºC/5h, and (b) 750ºC/2h under air environment.

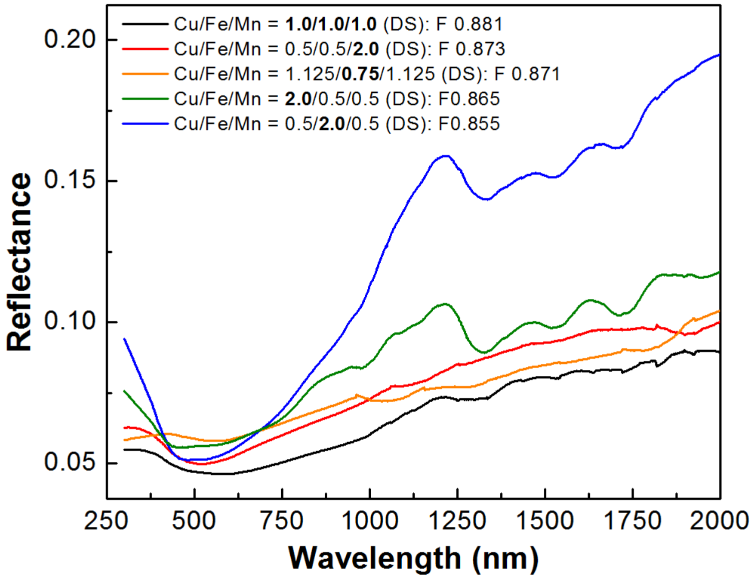

Figure 2-31. Reflectance measurements of SSC layers with a dense single layer structure composed of Cu-Fe-Mn oxide nanoparticles having different atomic compositions.

2.3.3.3 Tandem-structured SSC layers with a porous top layer

Using synthesized Co_3O_4 nanoparticles, porous top layers were fabricated for 2-layered tandem structures by means of polymer beads method. As described in the experimental part, the mixture solution was made of Co_3O_4 particles, polymer beads and polysiloxane resin with volume ratio of 1/5/6 in the order. Spray-coating solutions were made of cross-linked polymer beads with different size including 400 nm beads, 1.3 μm beads, 1.5 μm beads, a mixture of 1.3 μm and 400 nm beads (7/3 volume ratio), and a mixture of 5 μm, 1.3 μm, and 400 nm beads (3/5/2 volume ratio), which contributes to make porous morphology by decomposition during annealing procedure at 550°C in air. The porous SSC layer fabricated with polymer beads (1.3 μm and 400 nm) shows more porous surface morphology with both nanopores and micropores as shown in Fig. 2-32 (b), compared to a dense SSC layer fabricated without polymer beads of Fig. 2-32 (a).

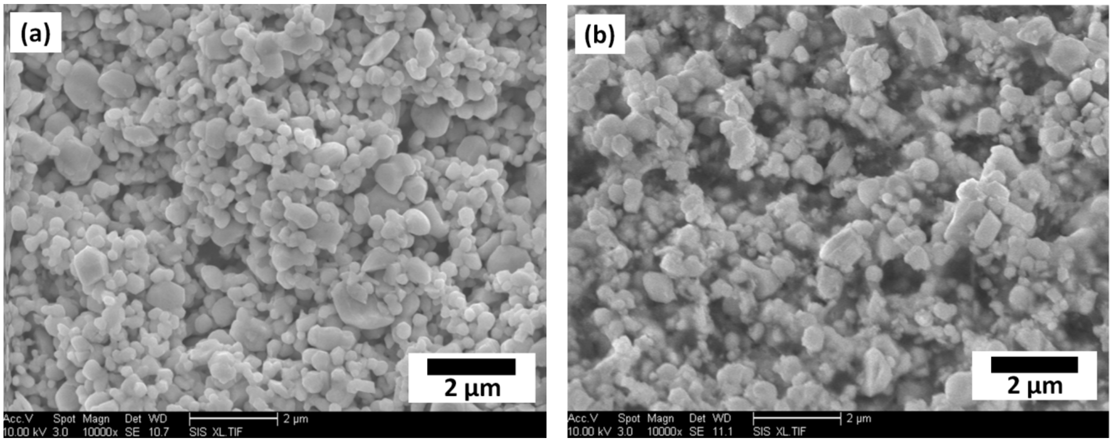

Figure 2-32. SEM images of (a) a dense top surface of SSC layer fabricated with Co_3O_4 nanoparticles, and (b) a porous surface of SSC layer coated with a solution composed of Co_3O_4 NPs dispersed with 1.3 μm sized polymer beads and 400 nm sized polymer beads which were burnt out after a spray coating procedure.

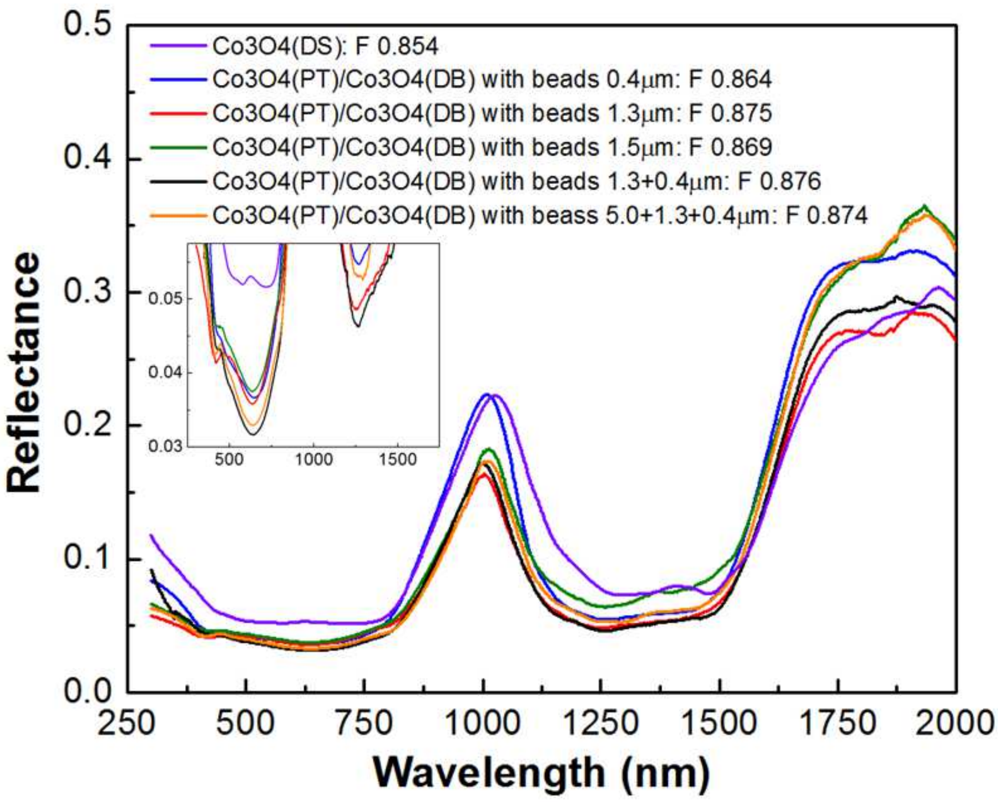

Figure 2-33. Reflectance comparison between a dense SSC layer of Co_3O_4 NPs and SSC layers having a porous top layer fabricated with various polymer beads compositions. (DS: a dense single layer, PT: a porous top layer, DB: a dense bottom layer).

Fig. 2-33 compares the reflectance between a dense SSC layer of Co_3O_4 and 2-layered SSC layers with a porous top layer fabricated with polymer beads. 2-layered SSC layers of Co_3O_4 particles with the structure of a porous top layer and a dense bottom layer shows lower reflectance and higher FOM values compared to a dense SSC layer of Co_3O_4 particles, because of their porous layers composed of nano-porous and micro-porous structures. From the result of reflectance measurement in Fig. 2-33, it is inferred that 1.3 μm beads affect more to decrease reflectance than 400 nm beads and 5 μm beads. And the mixture of 1.3 μm and 400 nm beads contributes more to decrease reflectance than beads with same size and the mixture containing 5 μm beads. In the SSC layer fabricated with the mixture of 1.3 µm and 400 nm beads, nano-porous structure formed by 400 nm beads play a role of decreasing reflectance in visible spectrum and micro-pores generated by 1.3 µm beads can decrease reflectance of near-IR spectrum. By means of the porous top layer, 2-layered Co_3O_4 SSC sample obtains lower reflectance and higher FOM (0.876) as exhibited in Fig. 2-33.

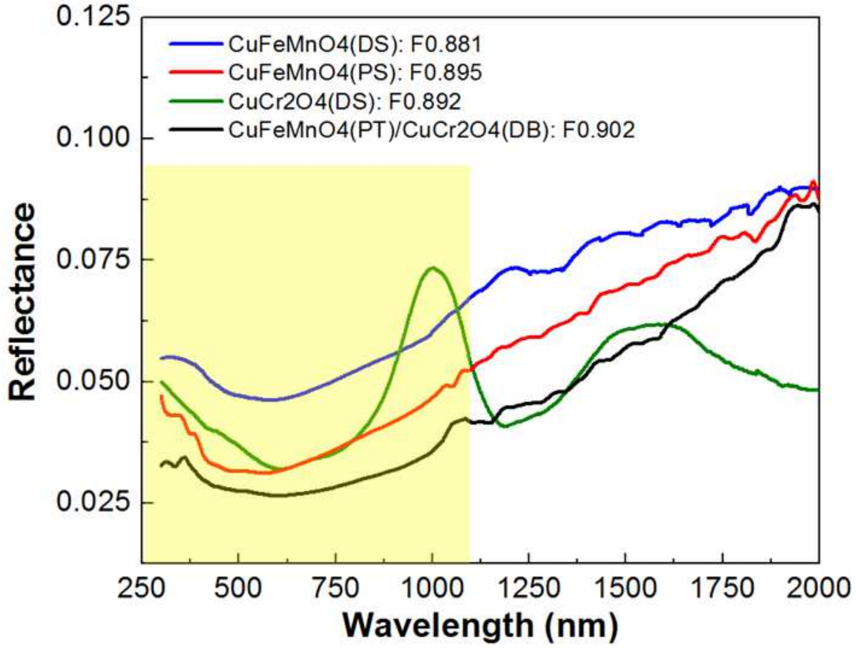

Figure 2-34. Reflectance and FOM comparison between SSC layers: A dense single layer of $CuFeMnO_4$ NPs, A porous single layer of $CuFeMnO_4$ NPs, A dense single layer of $CuCr_2O_4$, and two-layered SSC structure with a porous $CuFeMnO_4$ top layer and a dense $CuCr_2O_4$ bottom layer. (PS: a porous single layer)

The optimized condition to form the porous layer was applied to fabricate porous SSC layers of $CuFeMnO_4$ particles. Fig. 2-34 shows that a porous SSC layer of $CuFeMnO_4$ particles has lower reflectance than a dense SSC layer of $CuFeMnO_4$ particles and 2-layered tandem structure with a porous top layer of $CuFeMnO_4$ and a dense bottom layer of $CuCr_2O_4$ decreases reflectance much in wide spectrum range obtaining higher FOM (0.902). When considering a dense SSC layer of $CuCr_2O_4$ particles and a porous layer of $CuFeMnO_4$ particles, the SSC layer of $CuCr_2O_4$ has the property of lower reflectance in near-IR spectrum longer than 1.1 μm compared to the porous SSC layer of $CuFeMnO_4$ particles. And the porous SSC layer of $CuFeMnO_4$ particles exhibits the property of lower reflectance in visible spectrum and near-IR spectrum shorter than 1.1 μm, as shown in Fig. 2-34. This 2-layered SSC sample of $CuFeMnO_4$ and $CuCr_2O_4$ nanoparticles can obtain lower reflectance and higher FOM (0.902) resulting from the effect of tandem structure which absorbs more both visible spectrum and near-IR spectrum, compared to the single layered SSC samples.

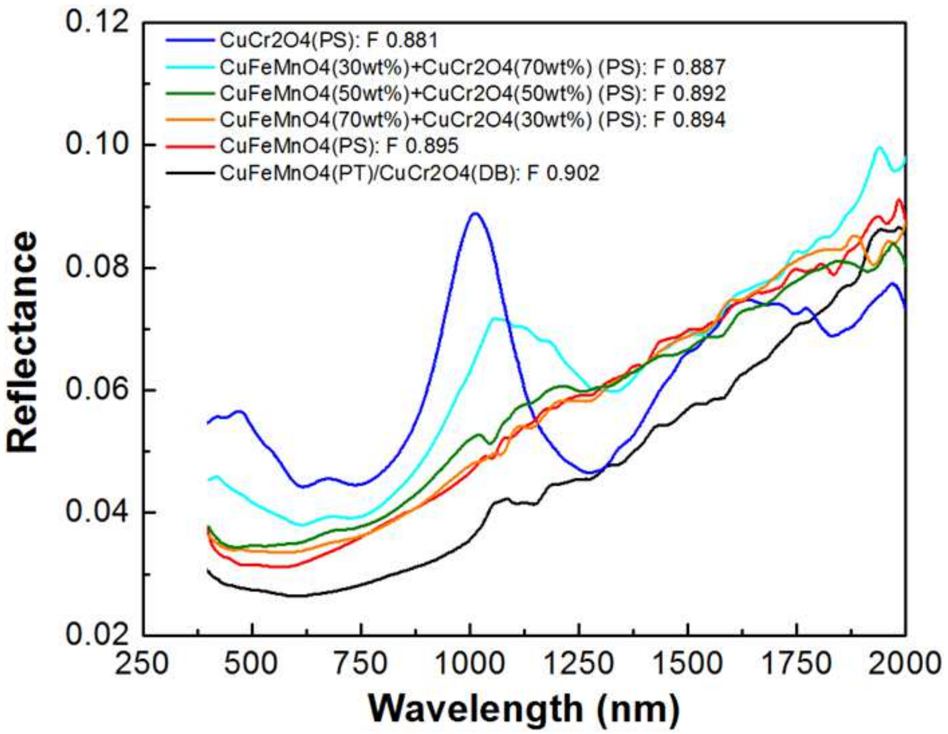

Figure 2-35. Reflectance and FOM comparison between tandem-structured SSC with 2-layered structure ($CuFeMnO_4$(PT)/$CuCr_2O_4$(DB)) and SSC samples with a porous single layer coated with mixed particles of $CuFeMnO_4$ and $CuCr_2O_4$.

Another type of porous SSC layers were fabricated with mixtures of $CuFeMnO_4$ and $CuCr_2O_4$ nanoparticles to be compared with 2-layered tandem structure. In porous SSC samples made of the mixture composition, the larger amount of $CuFeMnO_4$ particles they have, the lower reflectance and the higher FOM they obtain, as recognized in Fig. 2-35. But 2-layered tandem structure SSC sample with a porous top layer of $CuFeMnO_4$ and a dense bottom layer of $CuCr_2O_4$ still has best performance among all samples.

2.3.3.4 FOM endurance by thermal cycling test

In this thermal cycling test, CSP company-made Pyromark sample was included and compared to lab-coated Pyromark sample which was fabricated with modified Pyromark paint in our lab by mixing additional solvents. Lab-coated pyromark and other our samples were fabricated by spray-coating but CSP company-made Pyromark sample's fabrication procedure and solution recipe were not known exactly.

Fig. 2-36 shows that Co_3O_4/Co_3O_4 sample is most stable in reflectance of visible spectrum after thermal cycling test (750^{o}C/100cycles/air). Both $CuFeMnO_4/CuCr_2O_4$ sample and lab-coated Pyromark sample has similar behaviors that reflectance increased in visible spectrum and decreased in near-IR spectrum above 1 um. The reflectance increment in visible spectrum can be induced by the reduction of surface pores in nano-scale by high temperature effect. But dominant factors affecting the reflectance decrease in near-IR above 1μm have to be studied in more details in future research. And CSP company-made Pyromark sample increased reflectance much more in all spectrum range.

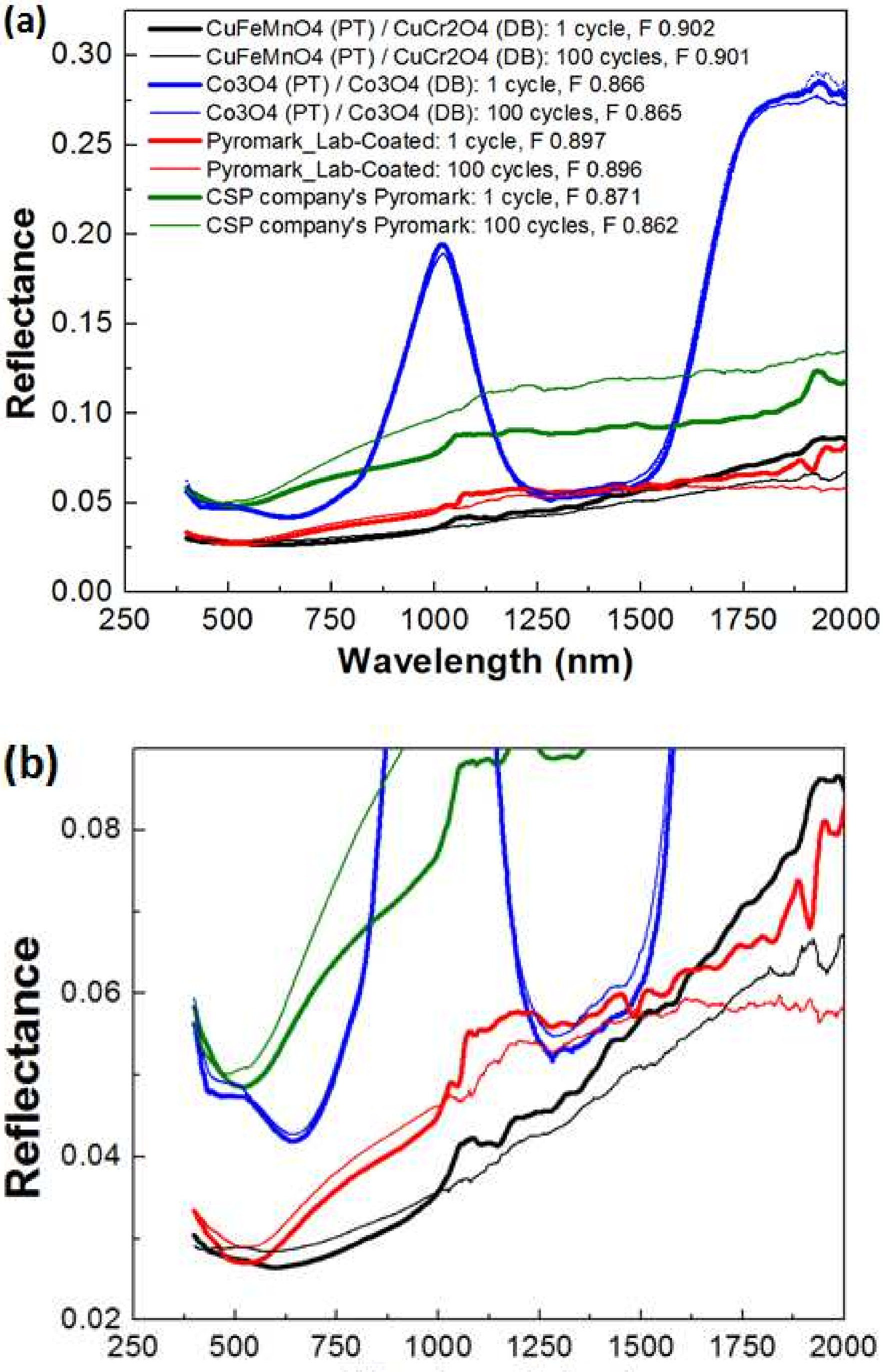

Figure 2-36. Behaviors of reflectance and FOM value in tested 4 types of SSC samples obtained after thermal cycling of 1 cycle and 100 cycles from room temperature to 750°C in air atmosphere. Figure (b) is a zoomed-in graph for detailed observations in low reflectance range.

As shown in Table 2-3, all 4 types of samples satisfy FOM endurance goal (≥0.98). But only $CuFeMnO_4/CuCr_2O_4$ sample can reach both FOM endurance and high FOM goal (>Pyromark). CSP company-made Pyromark sample has lowest FOM endurance which can be caused by delamination problems as seen in Fig. 2-37. This delamination can expand from many micro cracks in coating layer of CSP company-made Pyromark sample which can be observed in Fig. 2-38 (d-2). When there are many cracks, reflectance can increase because spectrum can pass through cracks and reach Inconel substrate on which spectrum can be reflected more than SSC layer.

Table 2-3. FOM endurance of SSC samples after thermal cycling test of 100 cycles (RT-750°C) calculated with FOM values.

	1 cycle	100 cycles	Endurance
(a) $CuFeMnO_4$(PT)/$CuCr_2O_4$(DB)	0.902	0.901	**0.9989**
(b) Co_3O_4 (PT)/Co_3O_4 (DB)	0.866	0.865	**0.9988**
(c) Pyromark_Lab-Coated (DS)	0.897	0.896	**0.9989**
(d) Pyromark_CSP Company	0.871	0.862	**0.9897**

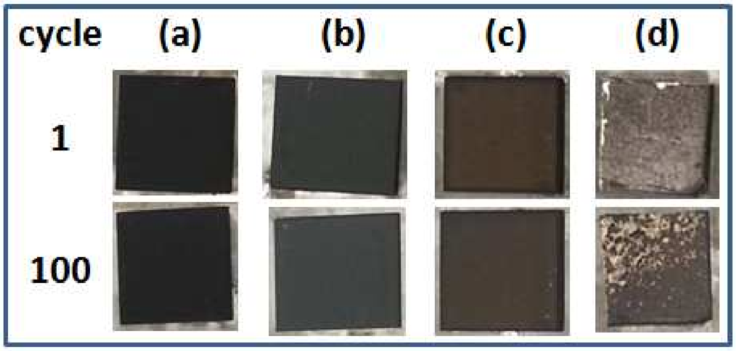

Figure 2-37. Photo images taken after thermal cycling of 1cycle and 100 cycles from room temperature to 750°C in air environment for 4 types of SSC samples: (a) $CuFeMnO_4$(PT)/$CuCr_2O_4$(DB), (b) Co_3O_4(PT)/Co_3O_4(DB), (c) Lab-coated Pyromark, and (d) CSP company-made Pyromark SSC sample.

After thermal cycling test (RT-750°C/100cycles/air), porous surface morphologies of $CuFeMnO_4/CuCr_2O_4$ sample and Co_3O_4/Co_3O_4 sample were preserved well to be similar to 1-cycled samples in miro-scaled image, as can be seen in Fig. 2-38 (a-1), (a-2), (b-1) and (b-2). These two-layered samples contain both nano-porous and micro-porous surface structure, which can decrease reflectance in both visible and near-IR spectrum. Nano-scaled morphology change can be studied in future research to analyze the effect of morphology change on reflectance through thermal tests in more details.

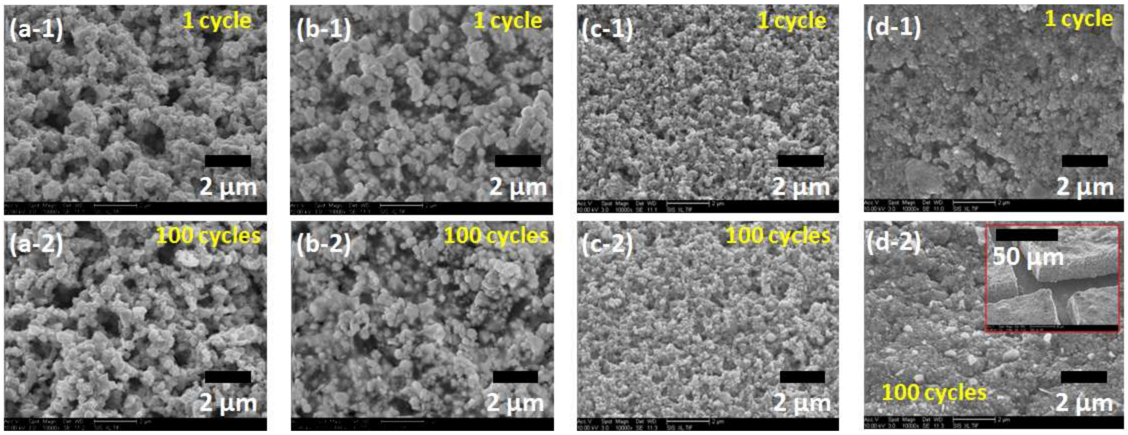

Figure 2-38. SEM images of surface morphologies of SSC samples after thermal cycling of 1 cycle and 100 cycles (RT-750°C) in air: (a) $CuFeMnO_4$(PT)/$CuCr_2O_4$(DB), (b) Co_3O_4(PT)/Co_3O_4(DB), (c) Lab-coated Pyromark, and (d) CSP company-made Pyromark SSC sample.

When evaluating the porous structure based on these SEM images, lab-coated Pyromark and CSP company-made Pyromark sample has much more dense surface structure than $CuFeMnO_4/CuCr_2O_4$ sample and Co_3O_4/Co_3O_4 sample, as shown Fig. 2-38 (c-1), (c-2), (d-1) and (d-2). Pyromark samples contain only very small nanopores on surface which cannot decrease reflectance in wide spectrum including visible and near-IR spectrum. Especially CSP company-made Pyromark sample has the most dense surface structure which is less effective to damp volume change during temperature change and can bring about many micro-cracks like inset image in Fig. 2-38 (d-2) and finally the delamination problem that CSP companies are suffering from.

2.3.3.5 FOM endurance by isothermal test

CSP company-made Pyromark sample was not placed for this isothermal test because it has delamination problem which cannot make uniform measurement. Fig. 2-39 shows that all samples increased reflectance in wide spectrum range including visible spectrum and near-IR spectrum, which can be affected much by the most harsh thermal test conditions (750°C/500h/air). For instance, the porous surface morphology with nano-scaled pores and micro-scaled pores can be degraded at high temperature (750°C) for 500h, which can contribute to increase the reflectance in wide spectrum.

As shown in Fig. 2-39 (b), in $CuFeMnO_4/CuCr_2O_4$ sample and lab-coated Pyromark sample 1μm peak emerged after isothermal annealing at 750°C. This new 1 μm peaks may result from the new formation of CuO phase after a long time annealing at high temperature, because the layer made of CuO nanoparticles increases reflectance in near-IR spectrum from 800 nm wavelength, as shown in Fig. 2-40. The reason of 1 μm reflectance peak has to be studied in future research.

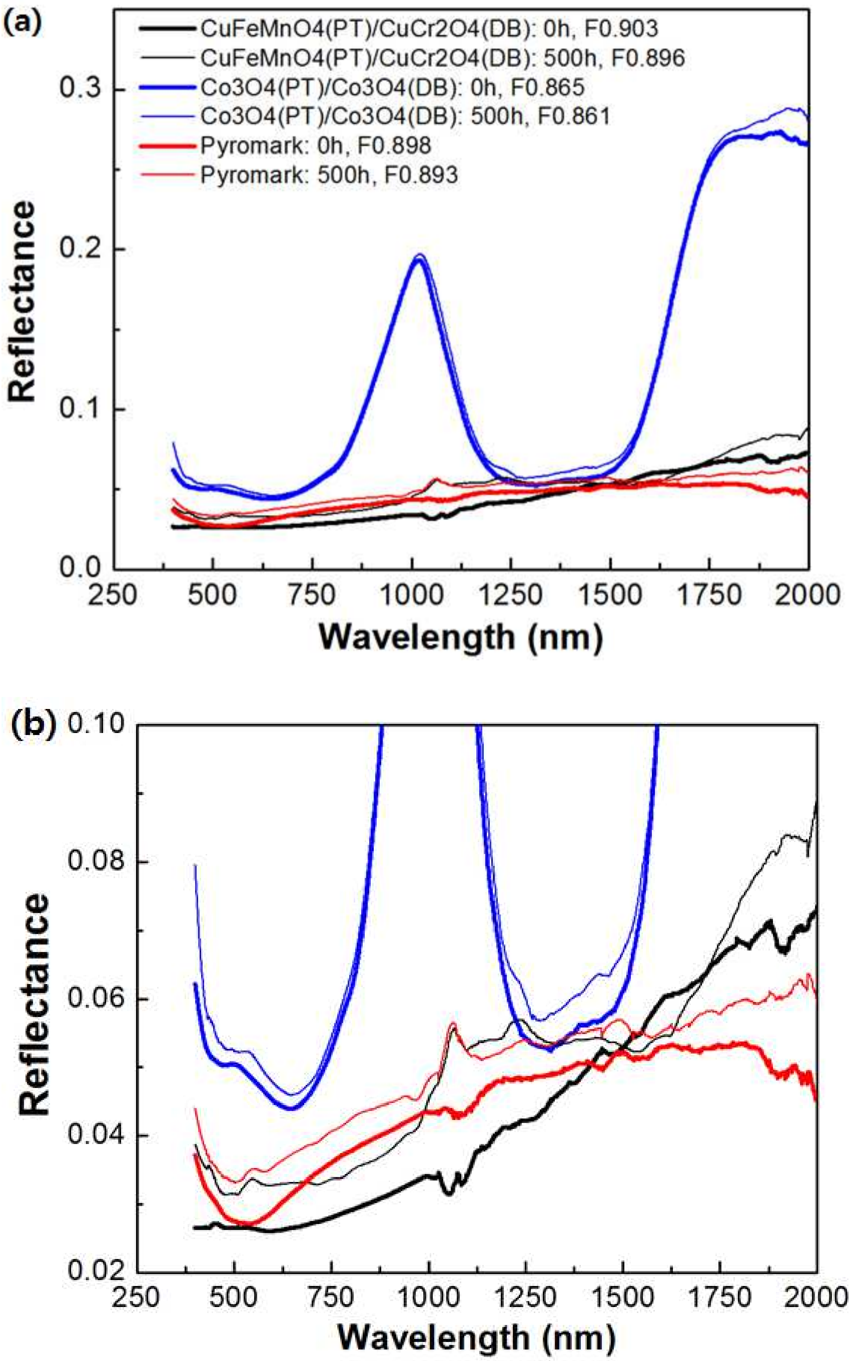

Figure 2-39. Behaviors of reflectance and FOM value in tested 4 types of SSC samples obtained before and after isothermal test at 750°C for 500h in air atmosphere. Figure (b) is a zoomed-in graph for detailed observations in low reflectance range.

In Table 2-4, all samples satisfy FOM endurance goal but only $CuFeMnO_4/CuCr_2O_4$ sample can satisfy both FOM endurance (0.98) and high FOM goal (>Pyromark). That is, after the most harsh isothermal test at 750°C for 500h in air, FOM of $CuFeMnO_4/CuCr_2O_4$ sample still keeps 0.895 and 0.896.

Table 2-4. FOM endurance of SSC samples after isothermal test at 750°C for 500h in air.

	0h	500h	FOM Endurance
$CFM/CuCr_2O_4$	0.903	0.896	**0.9922**
Co_3O_4/Co_3O_4	0.865	0.861	**0.9954**
Pyromark	0.898	0.893	**0.9944**

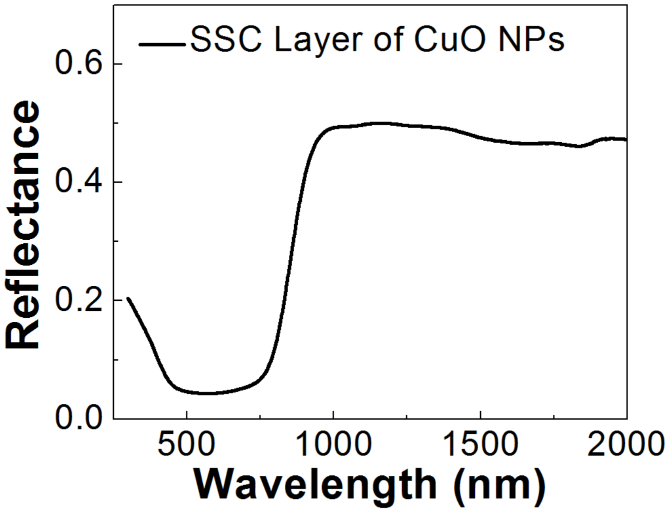

Figure 2-40. Reflectance measured for SSC layer fabricated with CuO nanoparticles and annealed at 750°C/2h/air.

After the isothermal annealing at 750°C/500h/air, the porous surface structure was almost preserved but the particle growth could be observed as shown in Fig. 2-41(a-2). This growing of particle and crystal can reduce the degree of surface porosity, by which reflectance can increase in all spectrum range. In lab-coated Pyromark sample, it has more dense surface structure which can make micro-cracks in as-prepared state as shown in Fig. 2-41(c-1). This micro-crack will be the driving force for delamination after a long time use at high temperature.

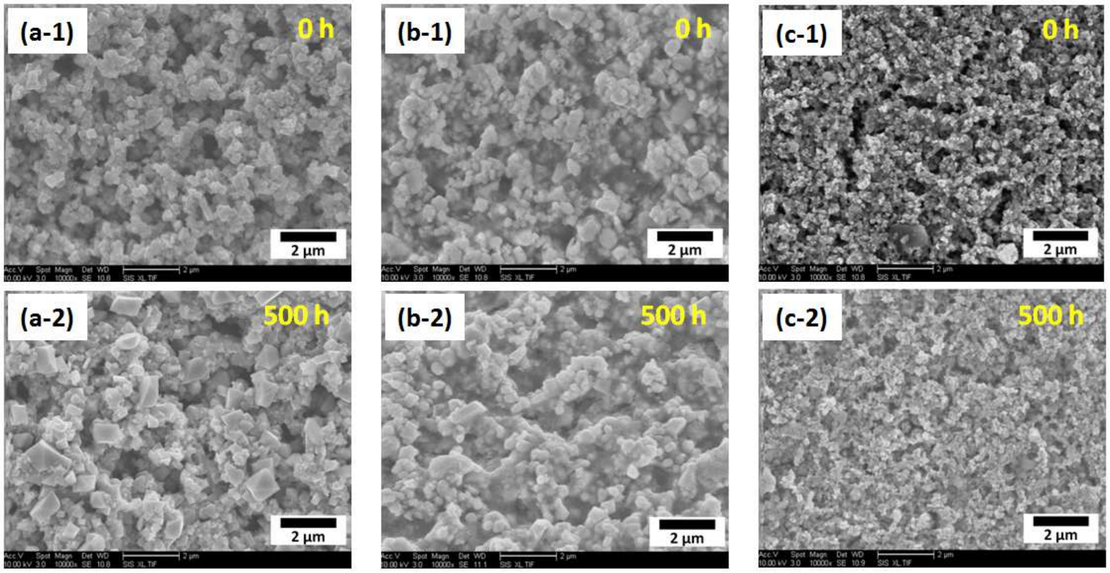

Figure 2-41. SEM images of surface morphologies of SSC samples obtained before and after isothermal test at 750°C for 500h in air: (a) $CuFeMnO_4$(PT)/$CuCr_2O_4$(DB), (b) Co_3O_4(PT)/Co_3O_4(DB), and (c) Lab-coated Pyromark SSC sample.

2.3.3.6 Adhesion of coating layer

SunShot milestone of adhesion is to keep a survived area percent ≥ 95%, after thermal tests. Fig. 2-42 shows that $CuFeMnO_4$/$CuCr_2O_4$ sample has a good adhesion performance satisfying milestone (95%), after all thermal tests. And Figure 15 also shows that the repaired $CuFeMnO_4$/$CuCr_2O_4$ sample has a good adhesion performance which is better than milestone (95%), after isothermal test (600°C/1000h/air).

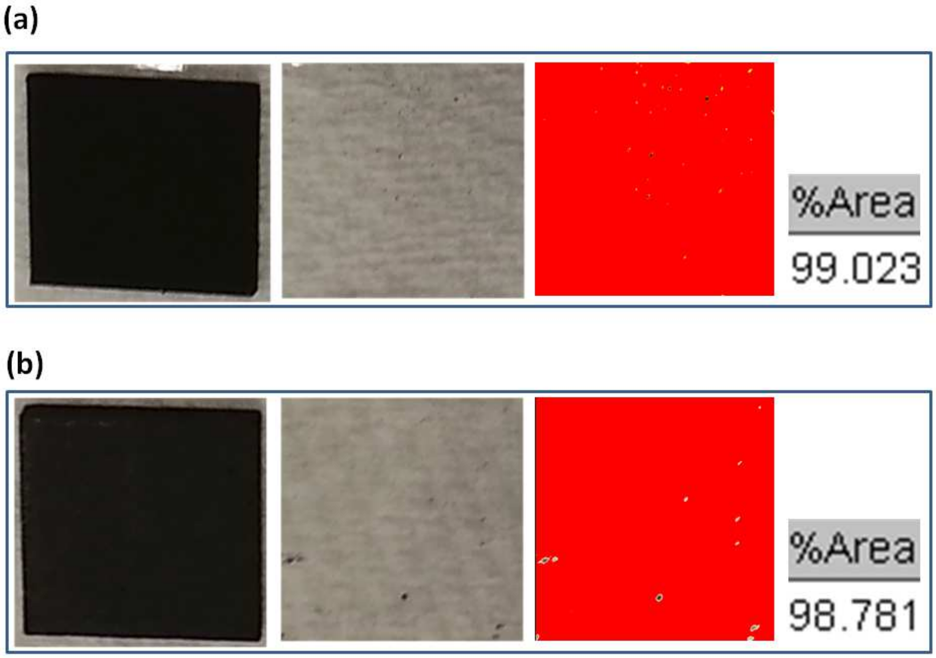

Figure 2-42. Adhesion test results of $CuFeMnO_4$(PT)/$CuCr_2O_4$(DB) SSC layer (a) after thermal cycling of 100 cycles (RT-750°C), and (b) after isothermal annealing at 750°C for 500h in air atmosphere. From the left in (a) and (b), sample photos, detached tape photos, analyzed images by ImageJ software, and the percent of survived area (red-colored area) are displayed in sequence.

2.4 Summary

To develop the solar receiver which has FOM ≥ 90 %, thermal stabiligy (FOM endurance ≥ 98 %), and strong adhesion (the remaining area by tape test ≥ 95%), this research proceeded with 3 approach ways including core-shell particles, nanowire forests structure, and 2-layered tandem structures.

Firstly, Si boride-coated Si core-shell type of nanoparticles was developed for semiconductor nanoparticles with high thermal oxidation resistance. Compared to bare Si NPs, it has remarkably slower oxidation rate by 3 times at 850 ^{o}C in air.

Secondly, the tandem-structured spectrally selective coating layer fabricated with CuO NWs layer and Co_3O_4 NPs by dip-coating method absorbs much more sunlight in spectrum shorter than 1.7 μm than a pure CuO NWs layer and a pure Co_3O_4 NPs SSC layer, utilizing the nanowires structure to decrease reflectance of visible spectrum and intrinsic properties of Co_3O_4 material to decrease reflectance of near-IR spectrum. And it has the cutoff wavelength at 1.7 μm above which infrared spectrum is reflected more. From these optical properties, the dip-coated tandem-structured SSC layer with CuO NWs and Co_3O_4 NPs achieves high FOM of 0.892 (conversion efficiency of solar to thermal energy: 89.2%).

Thirdly, 2-layered tandem structure SSC layer was devised with a porous $CuFeMnO_4$ top layer and a dense $CuCr_2O_4$ bottom layer and shows higher FOM value (0.903) than Co_3O_4 SSC layer and a SSC layer made with a commercial Pyromark black paint. From FOM endurance tests, 2-layered $CuFeMnO_4$/$CuCr_2O_4$ SSC sample keeps FOM endurance above 0.99 after 750^{o}C test for 500h in air which is a very harsh environment. Adhesion of coating layer in CFM/$CuCr_2O_4$ sample is strong enough to retain the coating layer above 98.5% after tape tests. This final SSC layer can satisfy the goal of solar receiver which will be used for next generation concentrating solar power plants to decrease the cost of electricity generation.

2.5 Acknowledgments

This chapter, in full, is composed of two reprints and a prepared manuscript for submission. The first is a reprint of the material as it appears in Nano Energy 9 (2014) 32-40, “Si boride-coated Si nanoparticles with improved thermal oxidation resistance”, Tae Kyoung Kim, Jaeyun Moon, Bryan VanSaders, Dongwon Chun, Calvin Gardner, Jae-Young Jung, Gang Wang, Renkun Chen, Zhaowei Liu, Yu Qiao, and Sungho Jin. The second is a reprint of the material as it appears in Nano Energy 11 (2015) 247-259, “Tandem structured spectrally selective coating layer of copper oxide nanowires combined with cobalt oxide nanoparticles”, Tae Kyoung Kim, Bryan VanSaders, Jaeyun Moon, Taewoo Kim, Chin-Hung Liu, Jirapon Khamwannah, Dongwon Chun, Duyoung Choi, Alireza Kargar, Renkun Chen, Zhaowei Liu, and Sungho Jin. The third is currently being prepared for submission to a SCI journal, “Two-layered tandem structures with copper-contained spinel metal oxide nanoparticles”, Tae Kyoung Kim, Bryan VanSaders, Elizabeth Caldwell, Sunmi Shin, Youngjin Kim, Zhaowei Liu, Renkun Chen, and Sungho Jin. The dissertation author was the primary investigator and author of these aforementioned three papers.

2.6 References

[1] J. Moon, D. Lu, B. VanSaders, T.K. Kim, S.D. Kong, S. Jin, R. Chen, and Z. Liu, Nano Energy **8**, 238 (2014).

[2] C.K. Ho, Proceedings of ASME 2012 6th International Conference on Energy Sustainablity & 10th Fuel Cell Science, ES FuelCell 2012-91374 (Draft).

[3] T.K. Kim, J. Moon, B. VanSaders, D. Chun, C.J. Gardner, J.-Y. Jung, G. Wang, R. Chen, Z. Liu, Y. Qiao, and S. Jin, Nano Energy **9**, 32 (2014).

[4] T.K. Kim, B. VanSaders, J. Moon, T. Kim, C.-H. Liu, J. Khamwannah, D. Chun, D. Choi, A. Kargar, R. Chen, Z. Liu, and S. Jin, Nano Energy **11**, 247 (2015).

[5] X. Jiang, T. Herricks, and Y.Xia, Nano Lett. **2**, 1333 (2002).

[6] A. Kargar, Y. Jing, S.J. Kim, C.T. Riley, X. Pan, and D. Wang, ACS Nano **7**, 11112 (2013).

[7] Y. Filinchuk, A.V. Talyzin, D. Chernyshov, and V. Dmitriev, Phys. Rev. **B76**, 092104-1 (2007).

[8] J. Urgnani, F.J. Torres, M. Palumbo, and M. Baricco, Int. J. Hydrog. Energy **33**, 3111 (2008).

[9] R.W. Olesinski, and G.J. Abbaschian, Bull. Alloy Phase Diagr. **5**, 478 (1984).

[10] K. Murase, T. Ogino, and Y. Mizushima, Jpn. J. Appl. Phys. **22**, 1771 (1983).

[11] G.-R. Yang, Y.–P. Zhao, and B.Y. Tong, Mater. Res. Soc. Symp. Proc. **426**, 83 (1996).

[12] J.R. Salvador, D. Bilc, S.D. Mahanti, and M.G. Kanatzidis, Angew. Chem. Int. Ed. **42**, 1929 (2003).

[13] P.C. Innocenzi, M. Guglielmi, M. Gobbin, and P. Colombo, J. Eur. Ceram. Soc. **10**, 431 (1992).

[14] M. Guglielmi, D. Festa, P.C. Innocenzi, P. Colombo, and M. Gobbin, J. Non-Cryst. Solids **147 and 148**, 474 (1992).

[15] J.A. Lemberg, and R.O. Ritchie, Adv. Mater. **24**, 3445 (2012).

[16] K. Kobayashi, K. Maeda, H. Sano, and Y. Uchiyama, Carbon **33**, 397 (1995).

[17] D. Kraemer, B. Poudel, H.-P. Feng, J.C. Caylor, B. Yu, X. Yan, Y. Ma, X. Wang, D. Wang, A. Muto, K. McEnaney, M. Chiesa, Z. Ren, and G. Chen, Nat. Mater. **10**, 532 (2011).

[18] M. Jang, Y. Park, M. Jun, Y. Hyun, S.-J. Choi, and T. Zyung, Nanoscale Res. Lett. **5**, 1654 (2010).

[19] L.L. B varanowski, G.J. Snyder, and E.S. Toberer, Energy Environ. Sci. **5**, 9055 (2012).

[20] S.M. Sze, Physics of Semiconductor Devices, 2nd Ed., Wiley, New York, 1981, pp15.

[21] S. Asbrink, and A. Waskowska, J. Phys. : Condens. Matter **3**, 8173 (1991).

[22] R. Restori, and D. Schwarzenbach, Acta Crystallogr. **B42**, 201 (1986).

[23] X. Jiang, and T. Herricks, Y. Xia, Nano Lett. **2**, 1333 (2002).

[24] J. Ghijsen, L.H. Tjeng, J. vanElp, H. Eskes, J. Westerink, and G.A. Sawatzky, Phys. Rev. **B38**, 11322 (1988).

[25] F.P. Koffyberg, and F.A. Benko, J. Appl. Phys. **53**, 1173 (1982).

[26] J.P. Picard, G. Baud, J.P. Besse, and R. Chevalier, J. Less-Common Met. **75**, 99 (1980).

[27] K. Peng, Y. Xu, Y. Wu, Y. Yan, S.-T. Lee, and J. Zhu, Small **1**, 1062 (2005).

[28] L. Tsakalakosa, J. Balch, J. Fronheiser, B.A. Korevaar, O. Sulima, and J. Rand, Appl. Phys. Lett. **91**, 233117-1 (2007).

[29] M.D. Kelzenberg, S.W. Boettcher, J.A. Petykiewicz, D.B. Turner-Evans, M.C. Putnam, E.L. Warren, J.M. Spurgeon, R.M. Briggs, N.S. Lewis, and H.A. Atwater, Nat. Mater. **9**, 239 (2010).

[30] J. Zhu, and Y.Cui, Nat.Mater. **9**, 183 (2010).

[31] O. Crottaz, F. Kubel, H. Schmid, J. Mater. Chem. **7**, 143 (1997).

[32] PDF 00-020-0358.

CHAPTER 3: CNT-Embedded $LiCoPO_4$ NanoComposites for High Voltage Cathode of Lithium-Ion Batteries

This chapter, in full, is currently being prepared for submission to a SCI journal. “Carbon nanotube-embedded lithium cobalt phosphate nanocomposites for high voltage cathode of lithium ion batteries”, Tae Kyoung Kim, Cyrus S. Rustomji, Hyung-Man Cho, Duyoung Choi, Dongwon Chun, Elizabeth Caldwell, Jun Hyun Han, Renkun Chen, and Sungho Jin. The dissertation author was the primary investigator and author of this paper.

3.1 Introduction

Lithium-ion batteries with high energy density is still necessary to be developed for the application of energy storage systems and electrical vehicles which will expand the renewable power plants and decrease the carbon dioxide green house effect emitted from vehicles. Lithium-ion batteries can have high energy density by means of large capacity (mAh/g) and high operation voltage (V) because the gravimetric energy density means the product of capacity and voltage divided by weight. As mentioned in chapter 1, $LiCoPO_4$, $LiNiPO_4$, and $LiNi_{0.5}Mn_{1.5}O_4$ can be candidates as a high voltage cathode material. Among them, $LiCoPO_4$ (LCP) cathode shows discharging voltage of ~4.7 V which is located between Li $Ni_{0.5}Mn_{1.5}O_4$ and $LiNiPO_4$ voltage and has a theoretical capacity of ~ 167 mAh/g, which results in the energy density of ~ 800 Wh/kg. With a graphite anode in an electrolyte solution, a LCP cathode in a battery cell has a following reaction which shows charging voltage of ~ 5.0V and discharging voltage of ~ 4.7V.

$$\mathrm{LiCoPO_4+C_6} \xrightleftharpoons[\text{discharging: \textasciitilde 4.7V}]{\text{charging: \textasciitilde 5.0V}} \mathrm{Li_{1\text{-}x}CoPO_4+Li_xC_6}$$

This LCP material has orthorhombic crystal system with tetrahedron of P-O bonding and octahedron of Co-O bonding and olivine structure [1] as exhibited in Fig. 3-1. In the olivine crystal structure, Li^+ ion can diffuse one-dimensionally. On the other hand, in a spinel structure of $LiNi_{0.5}Mn_{1.5}$, lithium ion can diffuse three-dimensionally and in a layered structure of $LiCoO_2$, lithium ion diffuses two-dimensionally.

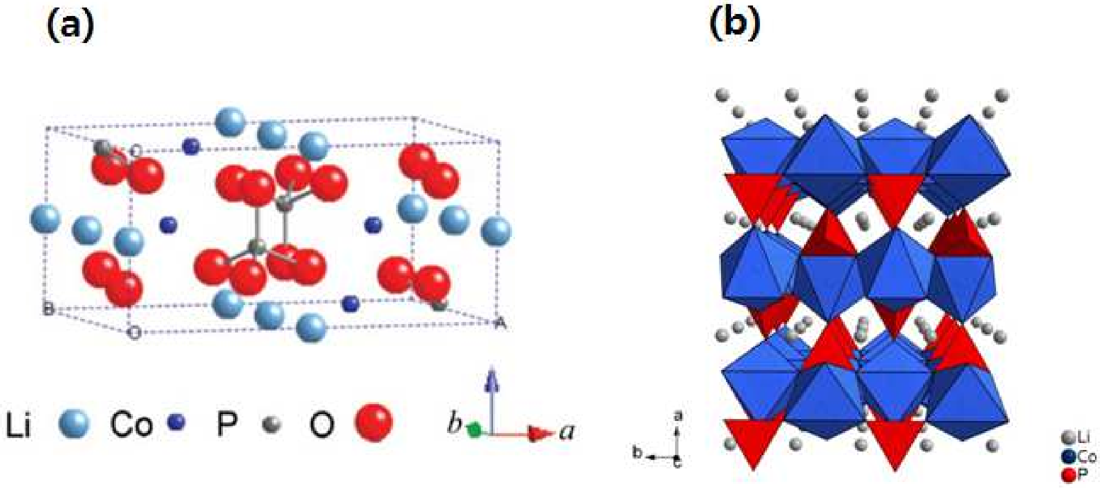

Figure 3-1. (a) Crystal structure of $LiCoPO_4$ with orthorhombic crystal system and (b) olivine structure [1].

Although there have been many researches on $LiCoPO_4$ cathode, it have not been commercialized because of poor cycle life and lower capacity than what is expected from the theoretical capacity. These drawbacks of LCP electrodes can be caused by low electrical conductivity of ~ 10^{-15} S/cm which is much lower than $LiFePO_4$ (~ 10^{-9} S/cm) with the same olivine structure [2], [3]. The low electron mobility can give a rise to too slow charge transfer reactions (intercalation/de-intercalation of Li^+ ion) to be used for rechargeable batteries.

Carbon nanotubes have been well known for their prominent potentials which can be applied for various fields such as electronic devices, semiconductors, and nanocomposite materials. Semiconductor property and metallic property can be obtained depending on the type of single-wall carbon nanotubes distinguished by the roll-up direction (zigzag, armchair, chiral) from graphene sheet. And multi-wall carbon nanotubes (MWCNT) shows usually metallic properties because they are composed of many types of SWCNTs as shown in Fig. 3-2. TEM images in Fig. 3-2 exhibit MWCNT having 35-40 nm in outer diameter and a bundle of SWCNTs where each SWCNT has 2-3 nm in diameter [4].

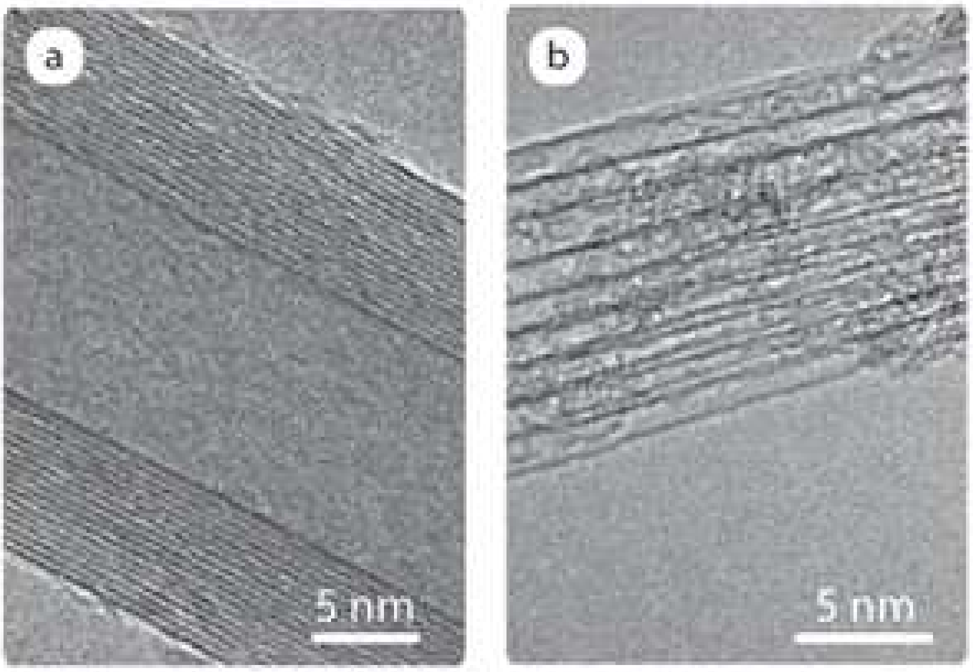

Figure 3-2. (a) Muli-wall carbon nanotube and (b) a bundle of single-wall carbon nanotubes [4].

From Table 3-1, it can be known that MWCNT has higher electrical conductivity (10^6-10^7 S/cm) than carbon black and graphite, from which carbon nanotubes are expected to contribute to shorten the path of electron movement inside LCP particles when carbon nanotubes can be embedded into LCP particles.

Table 3-1. The comparison of BET surface and electrical conductivity in some carbon materials [5].

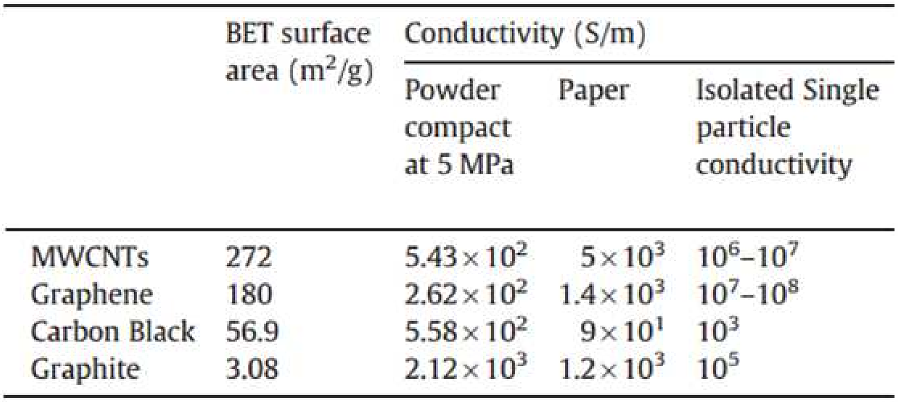

	BET surface area (m^2/g)	Conductivity (S/m)		
		Powder compact at 5 MPa	Paper	Isolated Single particle conductivity
MWCNTs	272	5.43×10^2	5×10^3	10^6–10^7
Graphene	180	2.62×10^2	1.4×10^3	10^7–10^8
Carbon Black	56.9	5.58×10^2	9×10^1	10^3
Graphite	3.08	2.12×10^3	1.2×10^3	10^5

Because of high theoretical energy density of $LiCoPO_4$ material, many researchers have been trying to improve the cycle life and actual capacity of battery cell with LCP cathode. Hydrothermal synthesis was used to fabricated nanoparticles, nanorods, and nanoplates as shown in Fig. 3-3 (a), and carbon-coated LCP particles were made by citric-acid aiding sol-gel synthesis like Fig. 3-3 (b). And LCP-carbon fiber composites were produced by depositing LCP particles onto nonwoven carbon fiber webs as seen in Fig. 3-3 (c). Although carbon nano-fibers were mixed with LCP particles, the impedance measurement showed large charge transfer resistance of ~ 150 Ω, as indicated in a graph of Fig. 3-3 (c). It can be found that the post-mixing of carbon fibers with LCP particles does not decrease much the charge transfer resistance of LCP particles because carbon fibers are located only outside of $LiCoPO_4$ partcles. From these literature reviews including high electrical conductivity of carbon nanotubes and the less effect of post-mixed LCP-carbon nanofiber composites, carbon nanotubes-embedded structure into $LiCoPO_4$ particles is expected to be more desirable for high voltage cathode of lithium-ion batteries.

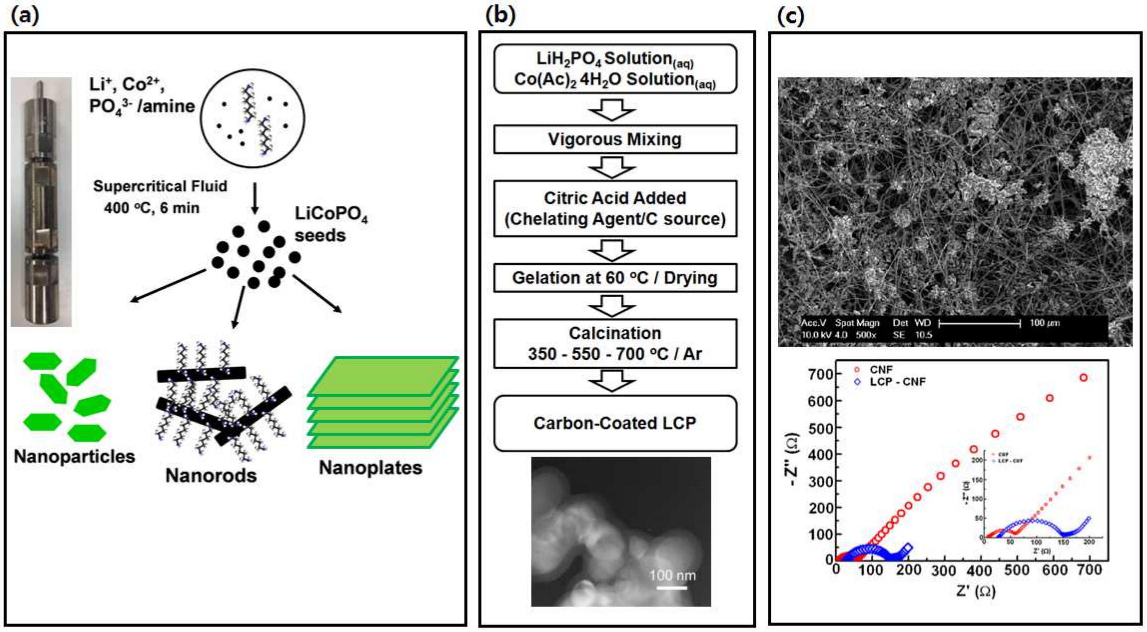

Figure 3-3. A few types of previous researches on $LiCoPO_4$ cathode; (a) nanoparticles, nanorods, and nanoplates synthesized hydrothermally [6], (b) carbon-coated LCP particles by sol-gel synthesis [7], and (c) LCP-carbon fiber composites [8].

3.2 Materials and Methods

3.2.1 Synthesis of CNT-embedded $LiCoPO_4$ nanocomposite particles

To make the carbon nanotube-embedded structure inside $LiCoPO_4$ (LCP) particles, multi-wall carbon nanotubes (MWCNTs) were dispersed in process of gelation of three precursors (LiCl, $Co(Ac)_2 \cdot 4H_2O$, and $(NH_4)_2HPO_4$), as shown in Fig. 3-4. At first, aforementioned three precursors and MWCNTs were mixed by a slow ball-mixer with YSZ ball. After moving the mixed dry powders containing MWCNTs into a glass beaker, de-ionized water (D.I.water) was added slowly in a small amount during mixing with a high shear impeller until gelation could be observed to begin as displayed in Fig. 3-4. The mixing and dispersion procedure of MWCNTs continued for 2 h after the gelation appeared in order to make MWCNTs distributed more uniformly in a gel induced from LCP's precursors and D.I.water. Gelation can result from the formation of $[Li(H_2O)_4]^+PO_4^{3-}[Co(H_2O)_6]^{2+}$ complex ion compound by adding D.I. water to the mixture of precursors, because LiCl, $Co(Ac)_2{\cdot}4H_2O$ and $(NH_4)_2HPO_4$ precursor can form $[Li(H_2O)_4]^+$ cation, $[Co(H_2O)_6]^{2+}$ cation, and PO_4^{3-} anion, respectively.

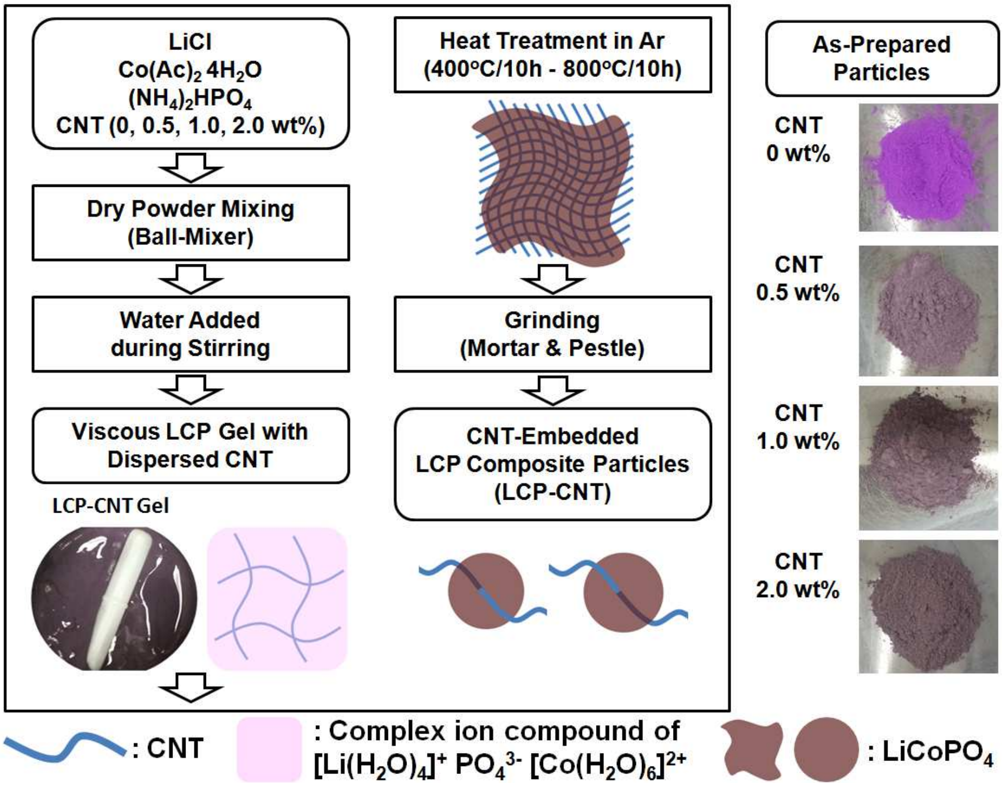

Figure 3-4. Synthesis procedure of CNT-embedded $LiCoPO_4$ nanocomposite particles using sol-gel process.

The gel slurry containing the dispersed MWCNTs was poured into an alumina crucible, followed by placing the crucible into an alumina tube of a furnace. Air was removed from the alumina tube by purging with Ar gas for 2 h at room temperature (RT) and then heat-treatment was carried out during continuous purging with temperature profile of 'RT – 400 ^{o}C / 10 h – 800 ^{o}C / 10 h – RT' which has temperature rate of 5 ^{o}C/min. After the heat-treatment was finished, CNT-embedded LCP composite particles (LCP-CNT composites) could be obtained by grinding heat-treated composites with mortar and pestle. Photos in a right side of Fig. 3-4 exhibit the synthesized particles of bare LCP and CNT-embedded LCP particles having different CNT amount. The bare LCP particles without CNT look pink and LCP-CNT composites are getting more dark color with dispersed CNT amount increasing.

3.2.2 Electrode and coin cell fabrication

Coating slurries for electrodes were prepared by mixing bare LiCoPO4 particles or LCP-CNT composite particles, carbon black, and PVdF binder in weight ratio of 8/1/1 (LCP/carbon black/binder) in n-methyl-2-pyrollidone solvent. After mixing the slurry for 1 day, the slurry was coated on aluminum foil (15 μm thick) with wire-wound rod (Meyer bar, #60, Gardner Company) followed by drying at 100 ^{o}C for 12 h in a vacuum oven, from which bare LCP cathode and LCP-CNT composite cathode could be fabricated to have 25-30 μm thick coating layer. For comparison, a post-mixed LCP-CNT composite electrode was also made by mixing bare LCP particles (99 wt%) with MWCNTs (1 wt%) when making a coating slurry.

Coin cells were made with the assembly of a cathode/LP30/Li metal anode with polyethylene separator (23 μm thick) in 2016 coin cell case. LP30 electrolyte was purchased from BASF and composed of $LiPF_6$ salt dissolved in EC and DMC. Especially, the inner surface of cathode case was covered with a gold layer by sputtering in order to prevent the case from oxidation at high voltage.

3.2.3 Characterization

X-ray diffraction (XRD) analysis

X-ray diffraction (XRD) analysis was carried out to confirm the crystal structure of carbon nanotubes, bare LiCoPO4 particles, and LCP-CNT composite particles. XRD measurement was made by Bruker D2 Phaser XRD with Cu K_α (λ=0.154 nm) as a radiation source. The scanning of 2θ angle (degree) was made in the range of 10 ^{o}-80 ^{o} with a scanning rate of ~0.0406 deg/step/sec.

Raman spectroscopy

After making a flat layer of particles on a slide glass plate, carbon nanotubes, bare LCP, and LCP-CNT composite particles were measured with a raman spectroscopy machine (Renishaw) with 514 nm Ar-laser.

Scanning electron microscopy (SEM)

The size and shape of particles and carbon nanotubes were observed by SEM (Oxford, acceleration voltage of 10 kV). Especially, carbon nanotubes protruding from LCP particles were observed.

Transmission electron microscope (TEM)

LCP-CNT composite particles were analyzed with transmission electron microscope (TEM) (FEI Tecnai F20 G^2) operated at the acceleration voltage of 200 kV in bright field (BF) mode and high resolution (HR) mode. SAED pattern was also obtained to confirm the crystal structures during TEM observation.

Battery test (Charging/Discharging)

Coin cells were charged and discharged in a range of 3.0 V – 5.1 V in 0.05C rate with a battery tester (Arbin), based on 1C = 167 mAh/g.

Cyclic voltammetry (CV)

Cyclic voltammetry was measured with BioLogic's instrument in a range of 3.0 – 5.1 V in 1 mV/sec rate, in order to compare intercalation/de-intercalation voltages of lithium ion in cathodes including bare LCP cathode, CNT-embedded LCP-CNT composite cathode, and post-mixed LCP-CNT composite cathode.

Electrochemical impedance spectroscopy (EIS)

To analyze impedance behavior of coin cells with different type of cathodes, EIS was measured with BioLogic's instrument in open circuit voltage (OCV) state after charging up to 5.1 V by the cyclic voltametry with rate of 1 mV/sec.

3.3 Results and Discussion

3.3.1 Materials characterization

The synthesized bare $LiCoPO_4$ (LCP) particles, carbon nanotubes-embedded LCP-CNT composite particles, and multi-wall carbon nanotubes were analyzed with XRD for their crystal structures, as shown in Fig. 3-5. Carbon nanotubes (MWCNTs) have two main peaks of (002) and (100) plane which match well with the published crystal structure information of carbon nanotubes [9], [10]. The synthesized bare LCP particles have a few main peaks for (101), (111), (201), (020), and (311) plane which can confirm the orthorhombic crystal structure [1] and these XRD peaks appear also in LCP-CNT composite particles irrelevantly to the embedded amount of carbon nanotubes as observed in Fig. 3-5. Other XRD peaks which are different from bare LCP particles do not appear in LCP-CNT composite particles, which means MWCNT's embedding does not affect the crystal structure of $LiCoPO_4$ material. In XRD measurement of LCP-CNT composite particles, the XRD peaks of MWCNTs are not distinguishable because of overlapping of main peaks at $2\theta = \sim 26\,^{o}$ and the relatively small amount of MWCNTs compared to $LiCoPO_4$ material.

By Raman spectroscopy measurement for MWCNTs sample in Fig. 3-6, two main peaks are detected at 1348 cm^{-1} and 1583 cm^{-1} which can be assigned to D-band and G-band of MWCNTs, respectively as listed in Table 3-2 and these two Raman bands are generated from graphitic structure of carbon nanotube's walls [11]-[13]. The synthesized bare LCP particles have a main Raman peak at 948 cm^{-1} which is assigned to a symmetric vibration of PO_4^{3-} anion as shown in Fig. 3-6 and Table 3-2 [14]. MWCNT-embedded

LCP-CNT composite particles exhibit main Raman peaks of both LCP and MWCNTs as seen in Fig. 3-6, which gives an evidence of the co-existence of $LiCoPO_4$ and MWCNTs. What is interesting is that D-band and G-band of MWCNTs can be indentified for LCP-CNT composite particles by Raman spectroscopy, although XRD peaks of MWCNTs in LCP-CNT composite sample do not appear apparently. In this aspect, Raman spectroscopy is useful for detecting a small amount of materials in composite materials.

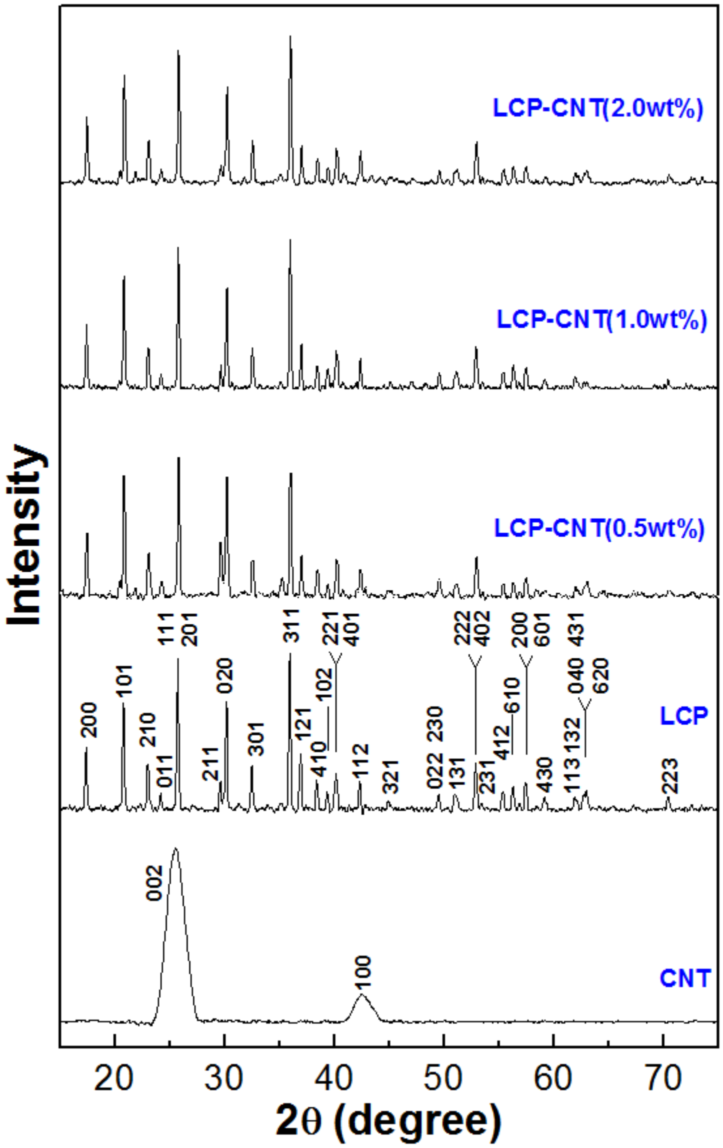

Figure 3-5. XRD analysis for carbon nanotubes (MWCNTs), bare LCP particles, and LCP-CNT composite particles with different amount of MWCNTs.

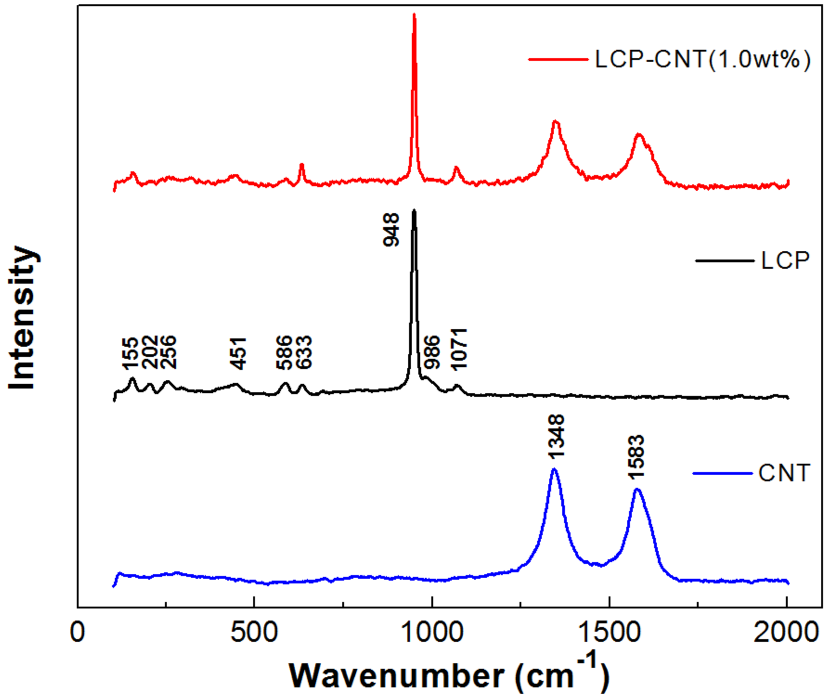

Figure 3-6. Raman spectroscopy measurements for MWCNTs, bare LCP particles, and LCP-CNT composite particles.

Table 3-2. Raman peaks information for carbon nanotubes and $LiCoPO_4$ [11]-[14].

	cm^{-1}	Assignment
CNT	1583	G-band, E_{2g} mode. Symmetric stretching of pairs of carbon sp^2 atoms.
CNT	1348	D-band, A_{1g} mode. Degree of disorder of carbon sp^2 bonds.
LCP	1071	Asymmetric stretching modes of PO_4^{3-} anion.
LCP	948	Intramolecular symmetric stretching of PO_4^{3-} anion. Strongest peak in olivine strectrum.
LCP	633 586 451	Bending modes of PO_4^{3-} anion.

Multi-wall carbon nanotubes used for this research has 10-30 nm in diameter and micro-sized length, as observed in Fig. 3-7 (a). And bare LCP particles and LCP-CNT composite particles have the size of 100 nm – 3 µm. MWCNTs in Fig. 3-7 (c) – (e) are distributed more uniformly than ones in Fig. 3-7 (f) which were just post-mixed with bare LCP particles. In LCP-CNT mixtures (Fig. 3-7 (f)) made by the post-mixing method, there is much agglomeration of MWCNTs which are not embedded or implanted into LCP material but float on the outer surface of LCP particles.

Although MWCNTs have high electrical conductivity of 10^6-10^7 S/cm, the MWCNTs located on the surface of LCP particles cannot contribute on the reduction of resistance of LCP particles. Therefore, it is expected that coin cells with MWCNTs-embedded LCP-CNT composite cathodes will achieve better performance in battery tests.

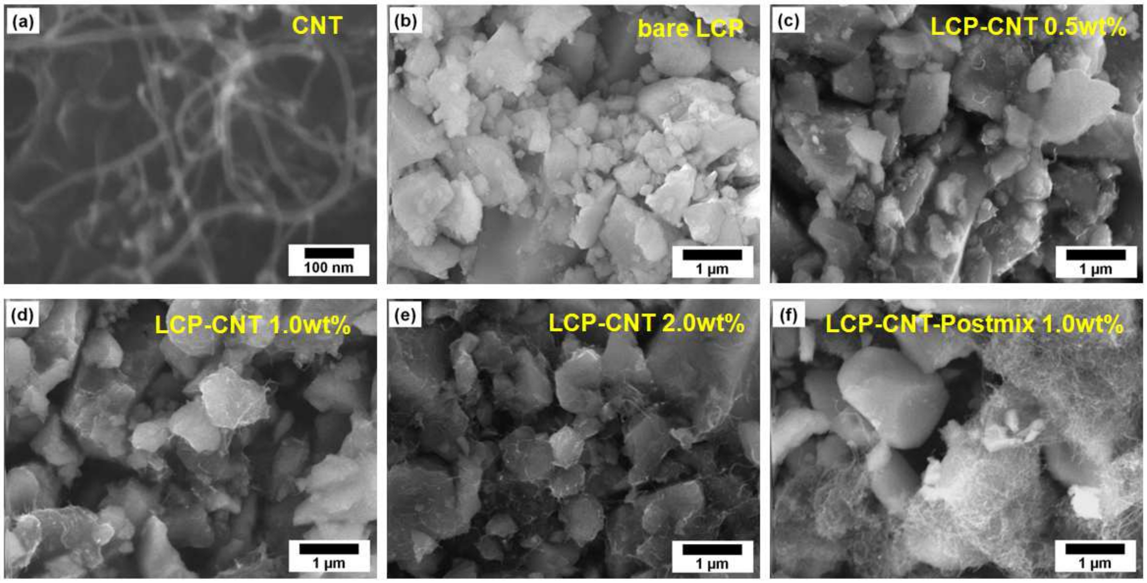

Figure 3-7. SEM images of (a) MWCNTs, (b) synthesized bare LCP particles, (c) LCP-CNT composite particles with 0.5 wt% MWCNTs, (d) LCP-CNT composite particles with 1.0 wt% MWCNTs, (e) LCP-CNT composite particles with 2.0 wt% MWCNTs, and (f) LCP-CNT mixtures by post-mixing of MWCNTs.

3.3.2 Carbon nanotube-embedded structure

TEM and SEM analysis are applied to look into the embedded structure of multi-wall carbon nanotubes (MWCNTs) into $LiCoPO_4$ (LCP) particles. Fig. 3-8 (a) shows a LCP-CNT composite particle which has a lot of MWCNTs inside particles or on the surface of particles, from which it can be assumed that there exist MWCNTs embedded inside LCP particles.

A selected area electron diffraction (SAED) pattern is analyzed for LCP-CNT composite particles during TEM observation as shown in Fig. 3-8 (b) and d-spacing determined in SAED pattern matches with published data of $LiCoPO_4$ material [1]. MWCNTs have similar d-spacing for their (002) and (100) plane to LCP material so that the identification of MWCNTs is difficult with SAED patterns as listed in Table 3-3.

Fig. 3-8 (c) exhibits that one multi-wall carbon nanotube protrudes from the surface of a LCP particle, which implies MWCNTs do not float on the surface of LCP particle but are embedded into LCP particle. When considering both a TEM image in Fig. 3-8 (a) and a SEM image in Fig. 3-8 (c), many short MWCNTs connected with a LCP particle in Fig. 3-8 (a), (c) and (d) can be regarded as some end parts of embedded MWCNTs inside LCP particles and some MWCNTs can exist only outside LCP particles as well.

This embedded structure of MWCNTs inside a LCP particle is highly expected to improve the electron mobility inside the LCP particle which can eventually increase the conductance of a LCP-CNT composite particle.

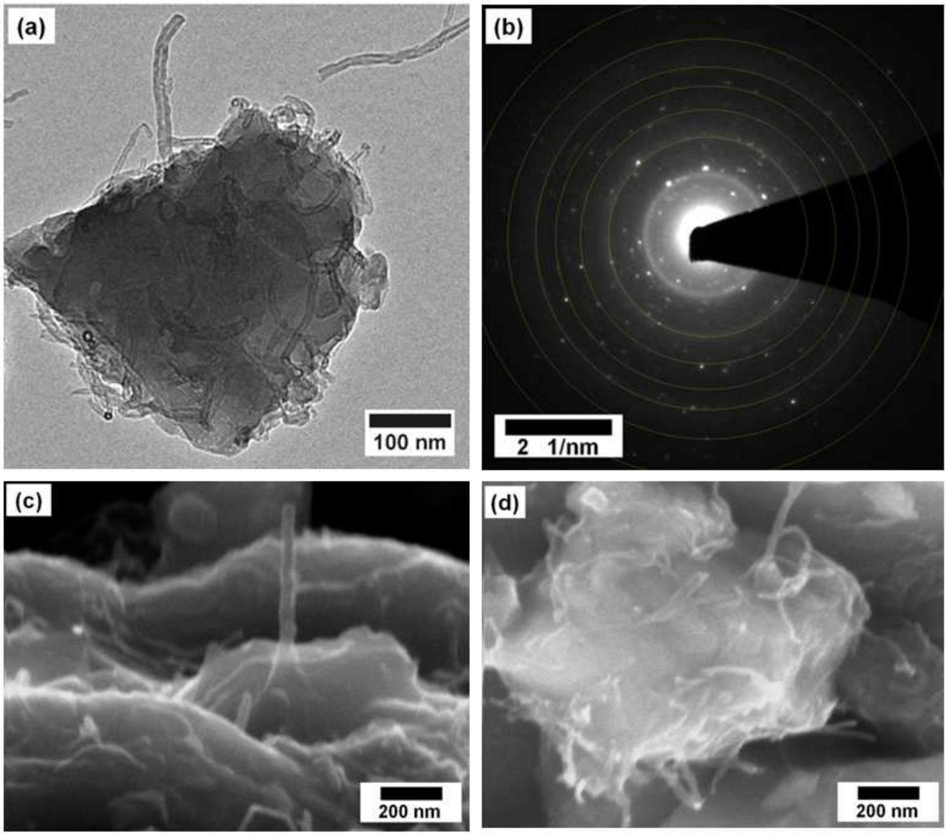

Figure 3-8. (a) TEM image of a LCP-CNT composite particle, (b) SAED pattern of LCP-CNT composite particles, (c) SEM image of MWCNT protruding from LCP surface, and (d) SEM image of a LCP-CNT composite particle.

Table 3-3. d-spacing and crystal planes for $LiCoPO_4$ and carbon nanotubes determined by SAED patterns of Fig. 3-8.

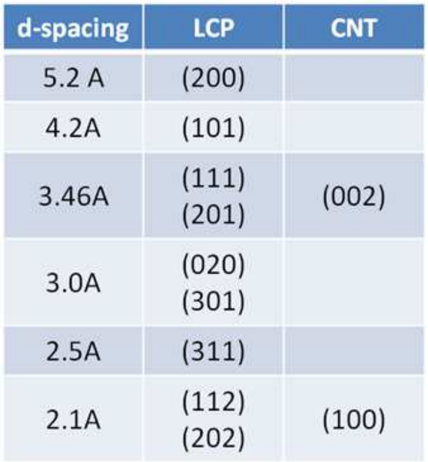

d-spacing	LCP	CNT
5.2 A	(200)	
4.2A	(101)	
3.46A	(111) (201)	(002)
3.0A	(020) (301)	
2.5A	(311)	
2.1A	(112) (202)	(100)

3.3.3 Charging-discharging capacity

Fig. 3-9 displays the first cycle capacity in charging and discharging test for coin cells fabricated with different $LiCoPO_4$ (LCP) cathodes and LP30 electrolyte. Considering the discharging capacity at 4.25 V, the cells have 24.4 mAh/g for bare $LiCoPO_4$ cathode, 35.8 mAh/g for LCP-CNT composite cathode with 0.5 wt% MWCNTs, 52.5 mAh/g for LCP-CNT composite cathode with 1.0 wt% MWCNTs, 43.2 mAh/g for LCP-CNT composite cathode with 2.0 wt% MWCNTs, and 9.1 mAh/g for post-mixed LCP-CNT mixture cathode with 1.0 wt% MWCNTs, as listed in Table 3-4.

All type of coin cells have a much longer charging time compared to discharging time, which can be caused by partial decomposition of LP30 electrolyte at high voltage around 5.0 V (vs. Li anode) [15]. Therefore, only the first cycle behaviors of coin cells are evaluated in order to optimize the amount of MWCNTs in LCP-CNT composite particles and to compare the capacity of cells with LCP-CNT composite cathodes to one of the cell with the post-mixed LCP-CNT mixture cathode.

Based on the discharging capacity as shown in Fig. 3-9, the optimized amount of MWCNTs is 1.0 wt% based on total weight of LCP and MWCNTs, because the capacity gradually increases and reaches the maximum value (52.5 mAh/g) when the amount of MWCNTs increases from 0 wt% to 1.0 wt% but the capacity decreases reversely when MWCNTs are added up to 2.0 wt%.

To explain the main effects on this capacity behavior, a few analysis methods are utilized including cyclic voltammetry, electrochemical impedance spectroscopy, and the relation analysis of capacity to conductance and the amount of MWCNTs, as the following discussions.

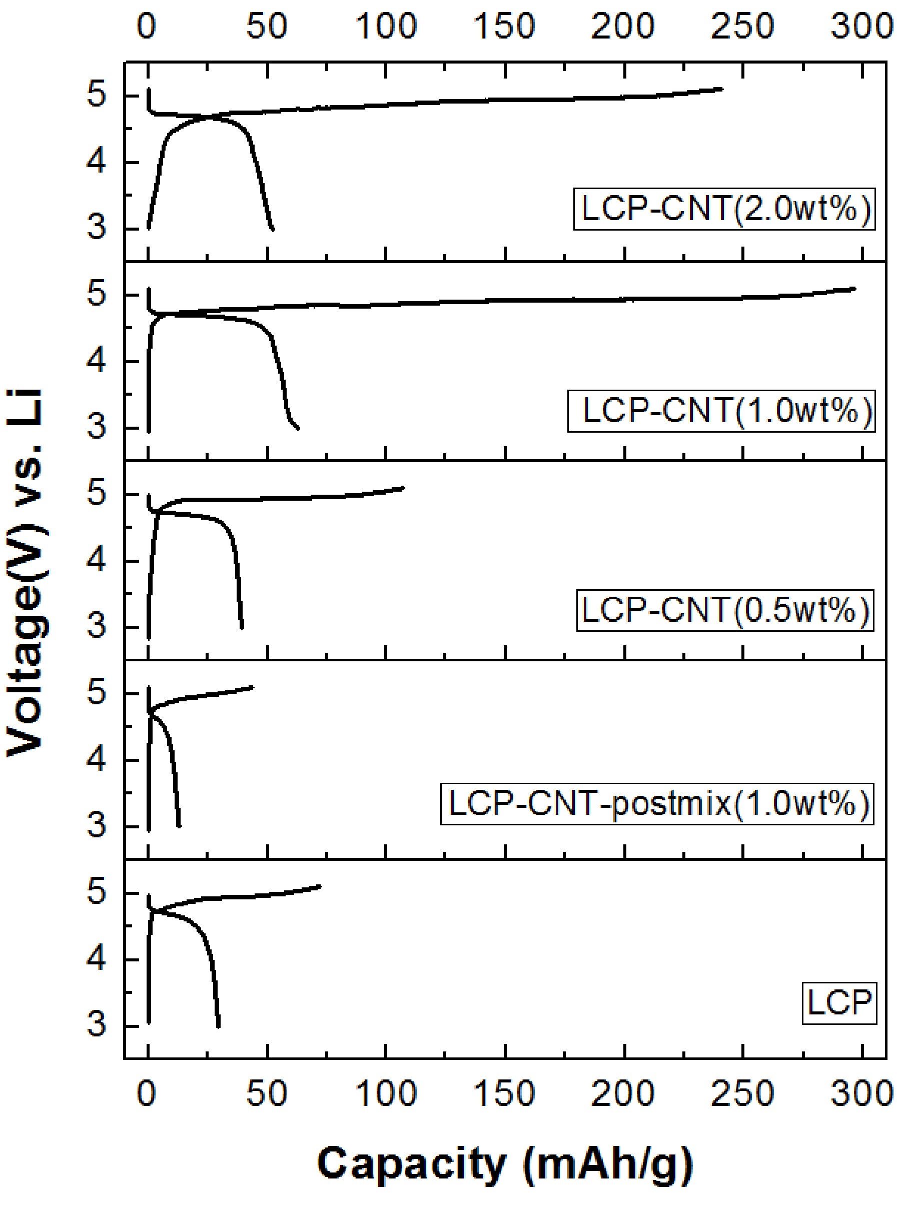

Figure 3-9. The first cycle capacity in charging and discharging tests for coin cells fabricated with a bare LCP cathode, a cathode of LCP-CNT mixture made by post-mixing, and LCP-CNT composite cathodes.

3.3.4 CNT-embedding effect on redox potentials

When another material is added to one cathode material, it can change the redox potentials if two materials have different capacity and reaction potentials and eventually can affect the cell performance. To find out the effect of the embedding of multi-wall carbon nanotubes (MWCNTs) on charging / discharging voltage, cyclic voltammetry was carried out for cells with a bare $LiCoPO_4$ (LCP), a LCP-CNT composite cathode, and a post-mixed LCP-CNT mixture cathode in a scanning rate of 1 mV/sec.

Fig. 3-10 shows that peak voltages of discharging reaction (intercalation of Li^+ ion into cathode) are similarly located around 4.59 - 4.61 V for bare LCP cathode, LCP-CNT composite cathode and post-mixed LCP-CNT mixture cathode. The cell with LCP-CNT composite cathode has slightly lower discharging peak voltage by ~ 20 mV than cells with bare LCP, and post-mixed LCP-CNT mixture cathode. The factor to make the small amount of difference of discharging voltage may be the embedded MWCNTs which have much lower intercalation voltage below 1.0 V (vs. Li/Li^+) [4], but the more study will be necessary in future research to interpret the voltage behavior of MWCNTs-embedded LCP-CNT composite cathode. As expected, the post-mixed LCP-CNT mixture has almost same discharging voltage as bare LCP cathode because MWCNTs in the mixture cathode are not embedded but placed on the surface of LCP particles. Charging (de-intercalation of Li^+ ion from cathodes) voltages for all types of cathodes do not have peaks with maximum current but increases gradually up to 5.1 V, which can be caused by the partial decomposition of LP30 electrolyte as aforementioned.

Carbon nanotubes including single wall nanotubes and multi-wall nanotubes can be intercalated and de-intercalated with Li^+ ion [4]. The voltage of this battery tests ranges from 3.0 V to 5.1 V which cannot make Li^+ ion intercalated into MWCNTs embedded into $LiCoPO_4$ particles. Therefore, it can be decided that the intrinsic capacity of MWCNTs does not affect much the total discharge capacity of LCP-CNT composite cathodes.

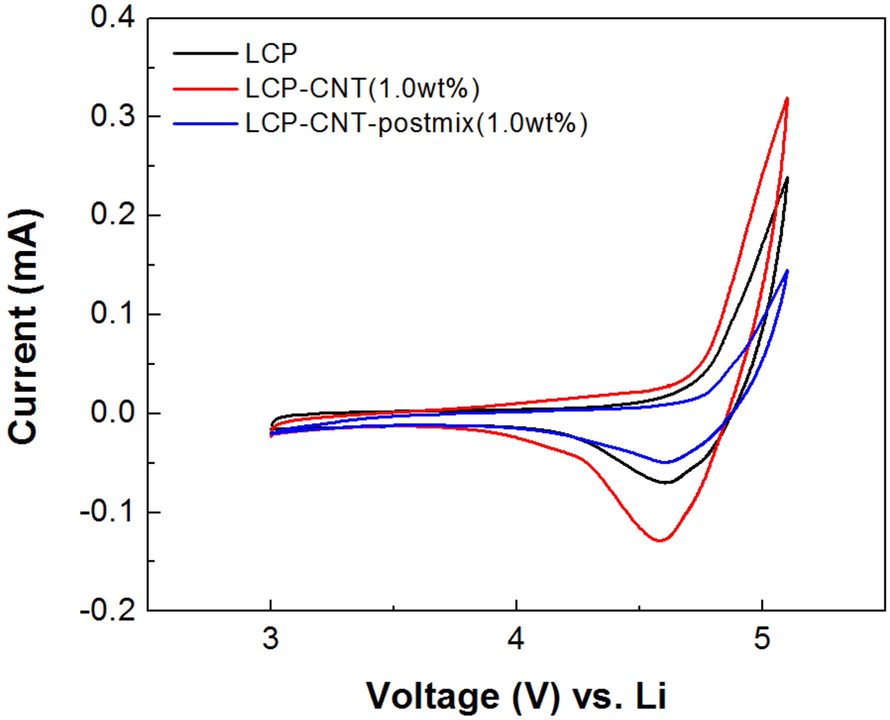

Figure 3-10. Cyclic voltammogram of coin cells fabricated with Li anode and cathodes of bare LCP, LCP-CNT composite, and post-mixed LCP-CNT mixture.

3.3.5 CNT-embedding effect on impedance

To measure the resistance of Li-ion's intercalation/deintercalation reaction which is called as charge transfer resistance, electrochemical impedance spectroscopy (EIS) is utilized for coin cells with a bare LCP cathode, LCP-CNT composite cathodes, and a post-mixed LCP-CNT mixture cathode. Fig. 3-11 shows the impedance measurement results where there are semi-circles made by scanning from high frequency (1 MHz) to low frequency (50-100 Hz). The semi-circle is composed of one small semi-circle in higher frequency range and another large semi-circle in lower frequency range which can be distinguished with much care and is more apparent especially in black-colored graph of Fig. 3-11.

The first intercept in Z'-axis is for ohmic resistance mainly determined by electrolyte impedance. A small semi-circle at high frequency is regarded as the impedance formed by solid-electrolyte interface (SEI) layer, and a large semi-circle at low frequency can be assigned to the impedance generated by charge transfer resistance (Rct, the resistance for intercalation/de-intercalation) and electrical double-layer capacitance. The linear increase of impedance after semi-circles is caused by Li-ion's diffusion inside particles, which is called as Warburg impedance [16]. Based on this interpretation, the equivalent circuit model can be made as shown in Fig. 3-12 which is similar to a typically reported model in published research results [16].

In Table 3-4 and Fig. 3-12, charge transfer (Rct) resistance decreases gradually from ~ 150 Ω to ~ 65 Ω when MWCNTs amount increases from 0.0 wt% to 2.0 wt% in LCP-CNT composite cathodes. On the other hand, a coin cell with the post-mixed LCP-CNT mixture cathode has high charge transfer resistance of ~ 170 Ω, even though MWCNTs of 1.0 wt% are mixed with LCP particles, which can result from the non-contribution on electron mobility inside LCP particles of MWCNTs located on the surface of LCP particles.

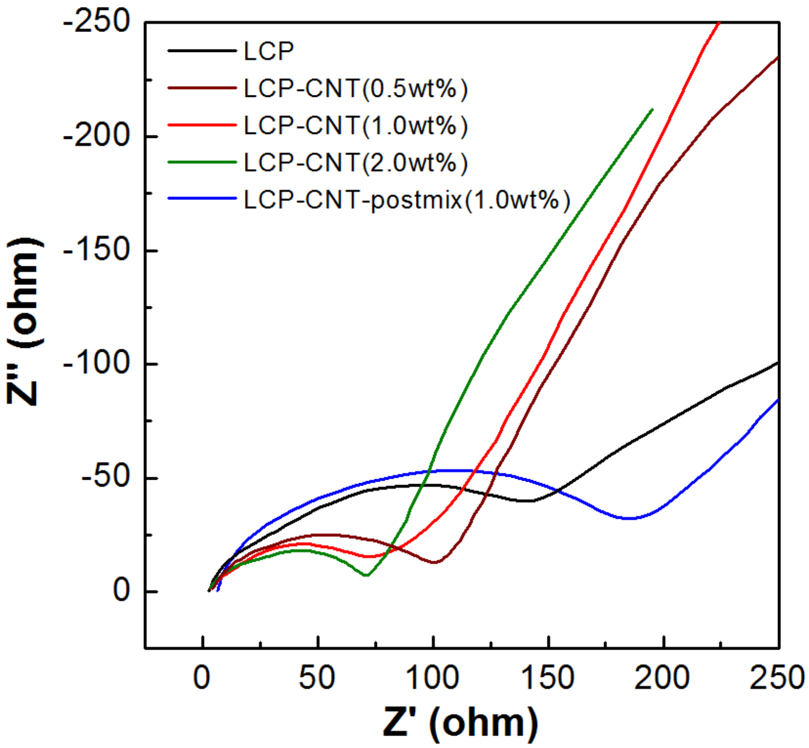

Figure 3-11. Electrochemical impedance spectroscopy measurements for coin cells with a bare LCP cathode, LCP-CNT composite cathodes, and a post-mixed LCP-CNT mixture cathode.

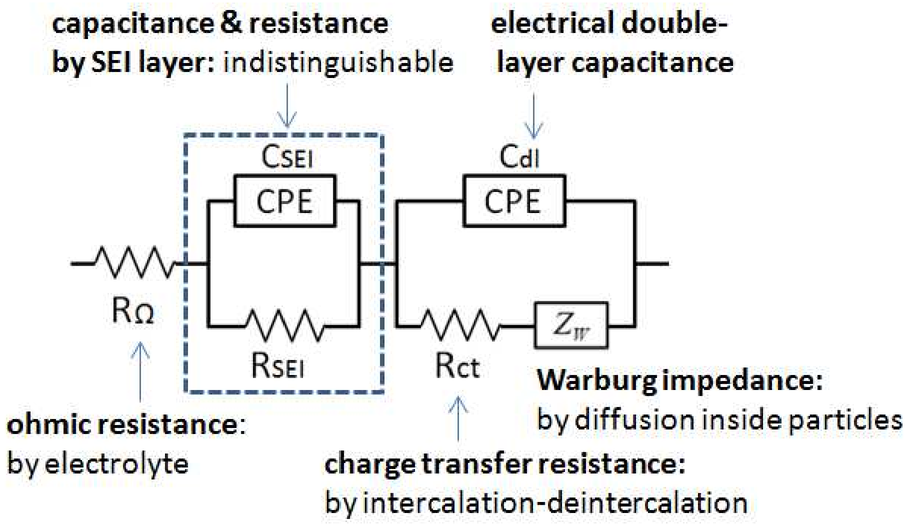

Figure 3-12. An equivalent circuit model to be applied to the coin cell with a LCP cathode and a Li anode.

Table 3-4. Charge transfer resistance and discharge capacity of coin cells with different type of cathodes.

	LCP	LCP-CNT (0.5wt%)	LCP-CNT (1.0wt%)	LCP-CNT (2.0wt%)	LCP-CNT-post-mixing (1.0wt%)
Rct (Ω)	150	110	80	65	170
Discharge Capacity to 4.25V (mAh/g)	24.4	35.8	52.5	43.2	9.1

3.3.6 Two main factors affecting the cell capacity behavior

As shown in Fig. 3-13, the charge transfer resistance (Rct) can be transformed to conductance for intercalation/de-intercalation reaction using the following equation; Conductance [S] = Resistance^{-1} [Ω^{-1}]. The discharge capacity increases proportionally to the conductance up to 1.0 wt% of MWCNTs in LCP-CNT composite cathodes, but what is interesting is that the discharge capacity decreases inversely with conductance for LCP-CNT composite cathode with 2.0 wt% MWCNTs.

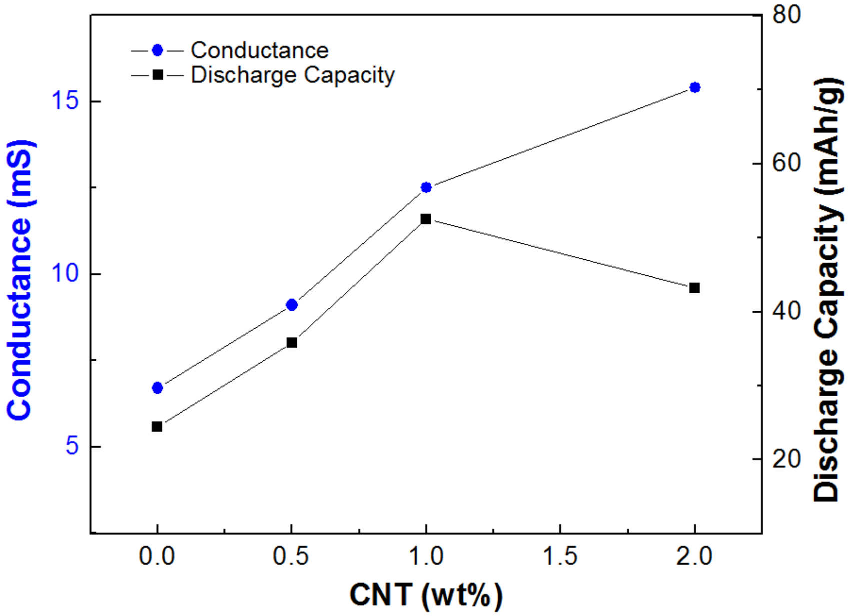

Figure 3-13. Relation of MWCNTs amount to conductance and discharge capacity of cells fabricated with bare LCP cathode and LCP-CNT composite cathodes.

One main factor to affect cell capacity with LCP-CNT composite cathodes can be higher conductance, that is, lower charge transfer resistance brought by the embedded MWCNTs, compared to the bare LCP cathode. Another factor to decide the capacity can be the uniformity of distribution state of MWCNTs in LCP-CNT composite particles. In LCP-CNT composite particles, MWCNTs of 2.0 wt% are too large amount to be dispersed uniformly during the gelation step of $LiCoPO_4$ material. This can form the agglomeration of MWCNTs, which can make some parts of $LiCoPO_4$ isolated from electrolyte and give a rise to the retardation of Li-ion's diffusion between $LiCoPO_4$ and electrolyte.

3.4 Summary

Muti-wall carbon nanotubes (MWCNTs)-embedded $LiCoPO_4$ composite particles (LCP-CNT composite) were synthesized by dispersing MWCNTs during the gelation step of $LiCoPO_4$ precursors, through which more uniform distribution of MWCNTs was achieved inside LCP particles.

The olivine crystal structure of synthesized bare LCP particles and LCP-CNT composite particles can be confirmed by XRD analysis. Raman spectroscopy analysis proves the co-existence of MWCNTs with $LiCoPO_4$ material.

LCP-CNT composite cathode shows a much improved performance than bare LCP cathode and post-mixed LCP-CNT mixture cathode. The optimized amount of MWCNTs is about 1.0 wt% based on the first cycle discharge capacity. It is concluded that the main contribution factors to the capacity improvement are the reduced charge transfer resistance observed by EIS and the uniform dispersion of multi-wall carbon nanotubes.

3.5 Acknowledgments

This chapter, in full, is currently being prepared for submission to a SCI journal. “Carbon nanotube-embedded lithium cobalt phosphate nanocomposites for high voltage cathode of lithium ion batteries”, Tae Kyoung Kim, Cyrus S. Rustomji, Hyung-Man Cho, Duyoung Choi, Dongwon Chun, Elizabeth Caldwell, Jun Hyun Han, Renkun Chen, and Sungho Jin. The dissertation author was the primary investigator and author of this paper.

3.6 References

[1] F. Kubel, Z. Kristallogr. **209**, 755 (1994). (JCPDS PDF85-0002).

[2] P.S. Herle, B. Ellis, N. Coombs, L.F. Nazar, Nat. Mater. **3**, 147 (2004).

[3] J. Wolfenstine, J. Power Sources **158**, 1431 (2006).

[4] B.J. Landi, M.J. Ganter, C.D. Cress, R.A. DiLeo, R.P. Raffaelle, Energy Environ. Sci. **2**, 638 (2009).

[5] B. Marinho, M. Ghislandi, E. Tkalya, C.E. Koning, G. de With, Powder Technology **221**, 351 (2012).

[6] Q.D. Truong, M.K. Devaraju, Y. Ganbe, T. Tomai, I. Honma, Scientific Reports, DOI: 10.1038/srep03975.

[7] J. Ni, H. Wang, L. Gao, L. Lu, Electrohimica Acta **70**, 349 (2012).

[8] L. Dimesso, C. Spanheimer, W. Jaegermann, Y. Zhangb, A.L. Yarin, Electrochimica Acta **95**, 38 (2013).

[9] T.M. Keller, S.B. Qadri, C.A. Little, J. Mater. Chem. **14**, 3063 (2004). (JCPDS PDF00-058-1638).

[10] F. Wang, J. Yang, Y. NuLi, J. Wang, J. Power Sources **196**, 4806 (2011).

[11] F. Tuinstra, J.L. Koenig, J. Chem. Phys. **53**, 1126 (1970).

[12] M.S. Dresselhaus, G. Dresselhaus, R. Saito, A. Jorio, Physics Reoprts **409**, 47 (2005).

[13] N. Yan, X. Zhou, Y. Li, F. Wang, H. Zhong, H. Wang, Q. Chen, Scientific Reports, DOI: 10.1038/srep03392.

[14] E. Markevich, R. Sharabi, O. Haik, V. Borgel, G. Salitra, D. Aurbach, G. Semrau, M.A. Schmidt, N. Schall, C. Stinner, J. Power Sources **196**, 6433 (2011).

[15] S.M.G. Yang, V. Aravindan, W.I. Cho, D.R. Chang, H.S. Kim, Y.S. Lee, J. Electrochem. Soc. **159(7)**, A1013 (2012).

[16] H.-M. Cho, W.-S. Choi, J.-Y. Go, S.-E. Bae, H.-C. Shin, J. Power Sources **198**, 273 (2012).

CHAPTER 4: Conclusions and Future Directions

To achieve a lower cost of electricity generation in concentrating solar power (CSP) plants, Si boride-coated Si nanoparticles were developed, and new spectrally selective coating (SSC) layers were devised including tandem structures made of CuO nanowires and Co_3O_4 nanoparticles and 2-layered tandem structure composed of a porous $CuFeMnO_4$ top layer and a dense $CuCr_2O_4$ bottom layer. Finally 2-layered SSC sample can satisfy the desired requirements for the next generation CSP; conversion efficiency of solar to thermal energy (FOM) $\geq$ 90% (operation temperature = 750 ^oC, sunlight concentration factor = 1000), FOM endurance $\geq$ 98% after thermal tests (isothermal annealing: 750^oC / 500h / air, thermal cycling: RT – 750^oC / 100 cycles / air), and coating layer's adhesion reliability $\geq$ 95% by tape test. For future research, the synthesis of smaller nanoparticles of $CuFeMnO_4$ and $CuCr_2O_4$ is necessary to obtain lower sunlight reflectance, and the possible causes for degraded FOM value after thermal annealing will have to be analyzed in more detail.

Electricity generated by renewable power plants such as CSP plant and wind power plant can be stored before distribution using battery energy storage system (BESS). To increase the energy density of lithium-ion batteries, multi-wall carbon nanotubes-embedded $LiCoPO_4$ composite (LCP-CNT composite) cathode was developed. Battery cells with this type of high voltage cathodes achieve a much larger discharging capacity (52.5 mAh/g) compared to the battery cell with bare $LiCoPO_4$ cathode (24.4 mAh/g), because the LCP-CNT composite electrode exhibits a lower charge transfer resistance as well as a more uniform dispersion of multi-wall carbon nanotubes inside LCP particles.

In future research, smaller LCP-CNT composite particles need to be developed to further increase the capacity. Three-dimensional image analysis is recommended to understand the embedded MWCNTs structure inside the cathode particles. Such an approach of embedding elongated conductors like MWCNTs can be applied to other electrode materials having low electrical conductivity such as $LiCoPO_4$ and $LiNiPO_4$.